

SYNTHESIS, SPECTROSCOPIC AND COMPUTATIONAL ANALYSIS OF
NICKEL INTEGRATED GERMANIUM CLUSTERS

A THESIS SUBMITTED TO
THE GRADUATE SCHOOL OF NATURAL AND APPLIED SCIENCES
OF
MIDDLE EAST TECHNICAL UNIVERSITY

BY

SİNEM ESRA ÖĞÜN

IN PARTIAL FULFILLMENT OF THE REQUIREMENTS
FOR
THE DEGREE OF MASTER OF SCIENCE
IN
CHEMISTRY

SEPTEMBER 2014

Approval of the thesis:

**SYNTHESIS, SPECTROSCOPIC AND COMPUTATIONAL ANALYSIS OF
NICKEL INTEGRATED GERMANIUM CLUSTERS**

Submitted by **SİNEM ESRA ÖĞÜN** in partial fulfillment of the requirements for
the degree of **Master of Science in Chemistry Department, Middle East
Technical University** by,

Prof. Dr. Canan Özgen

Dean, Graduate School of **Natural and Applied Sciences**

Prof. Dr. İlker Özkan

Head of Department, **Chemistry**

Assoc. Prof. Dr. Emren Nalbant Esentürk

Supervisor, **Chemistry Department, METU**

Examining Committee Members:

Prof. Dr. Ceyhan Kayran

Chemistry Department, METU

Assoc. Prof. Dr. Emren Nalbant Esentürk

Chemistry Department, METU

Assoc. Prof. Dr. Mehmet Fatih Danışman

Chemistry Department, METU

Assoc. Prof. Dr. Gülay Ertuş

Chemistry Department, METU

Assist. Prof. Dr. Ferdi Karadaş

Chemistry Department, Bilkent University

Date: 19.09.2014

I hereby declare that all information in this document has been obtained and presented in accordance with academic rules and ethical conduct. I also declare that, as required by these rules and conduct, I have fully cited and referenced all material and results that are not original to this work.

Name, Last Name: Sinem Esra ÖĞÜN

Signature:

ABSTRACT

SYNTHESIS, SPECTROSCOPIC AND COMPUTATIONAL ANALYSIS OF NICKEL INTEGRATED GERMANIUM CLUSTERS

Öğün, Sinem Esra

M. S., Department of Chemistry

Supervisor: Assoc. Prof. Dr. Emren Nalbant Esentürk

September 2014, 132 pages

Nanomaterials are attracting great deal of attention due to their wide range of applications such as in medicine, catalysis and electronics. The use of clusters either as seeds to synthesize larger molecular clusters or in assembled cluster materials is a promising way to prepare new nanomaterials. In particular, the possibility of clusters serving molecular control to design and tuning their properties to fit a particular application makes them more attractive in the search of new advanced materials. Therefore, besides synthesis of new cluster materials, the characterization and understanding of their unique properties is one of the major goals of cluster science.

Polyatomic main group clusters (Zintl ions) are great candidates to be used as “building-blocks” to prepare new cluster materials and they embody the potential to be used in applications such as bimetallic catalysis, photovoltaic devices, and light - emitting diodes. In this study, nickel (Ni) integrated germanium (Ge) Zintl ion clusters (i.e. $[\text{Ni}_2\text{Ge}_9(\text{PPh}_3)]^{2-}$, $[\text{Ni}_6\text{Ge}_{13}(\text{CO})_5]^{4-}$) have been synthesized. The experimental characterization of spectroscopic properties, which have never been

investigated before, has been performed. Vibrational, optical and electronic properties of Ni-Ge clusters have been investigated via UV-Vis, FTIR and Fluorescence spectroscopy. Moreover, frequency and time-dependent (TD) electronic transition calculations have been performed to complement the experimental results. The spectroscopic and computational findings are believed to contribute to the understanding and evaluation of cluster properties for their potential future applications.

Keywords: Nanomaterials, Clusters, Transition Metal Integrated Main Group Clusters, Nickel, Germanium, Gaussian 09, Time-Dependent, Frequency, Spectroscopy.

ÖZ

NİKEL AŞILANMIŞ GERMANYUM KÜMELERİNİN SENTEZİ, SPEKTROSKOPİK VE HESAPSAL ANALİZİ

Öğün, Sinem Esra

Yüksek Lisans, Kimya Bölümü

Tez Yöneticisi: Doç. Dr. Emren Nalbant Esentürk

Eylül 2014, 132 sayfa

Nanomalzemeler, tıp, katalizör ve elektronik gibi alanlardaki geniş kapsamlı uygulamalarından dolayı büyük ölçüde ilgi çekmektedir. Kümelerin daha büyük moleküler küme çekirdeği ya da toplanmış küme malzemeleri sentezinde kullanılması, yeni nanomalzemeler hazırlayabilmek için umut vadeden bir yol olabilir. Kümelerin moleküler kontrol sayesinde özelliklerinin tasarlanarak ya da ayarlanarak belirli bir uygulama alanında kullanılma olasılığı, kümeleri, gelişmiş yeni nanomalzemeler arayışında daha da çekici bir hale getirmektedir. Bu nedenle, yeni küme malzemelerinin sentezi dışında, kümelerin karakterizasyonunun ve özgün özelliklerinin anlaşılabilmesi küme biliminin başlıca hedeflerinden biridir.

Çok atomlu ana grup kümeleri (Zintl iyonları), yeni küme malzemelerinin “yapıtaşları” olarak kullanımı için çok iyi adaylardır ve kümelerin bimetalik katalizör, fotovoltajik aletler, ve ışık-yayan diyotlar gibi uygulamalarda kullanılma potansiyelini somutlaştırırlar. Bu çalışmada, nikel (Ni) aşılantmış germanyum (Ge) Zintl iyon kümeleri ($[\text{Ni}_2\text{Ge}_9(\text{PPh}_3)]^{2-}$, $[\text{Ni}_6\text{Ge}_{13}(\text{CO})_5]^{4-}$) sentezlenmiştir. Ayrıca

daha önce hiç yapılmamış olan spektroskopik özelliklerinin deneysel karakterizasyonu yapılmıştır. Ni-Ge kümelerinin titreşimsel, optik ve elektronik özellikleri UV-Vis, FTIR ve Floresans spektroskopik teknikler ile analiz edilmiştir. Bunlara ek olarak, deneysel sonuçları tamamlamak için frekans ve zamana-bağlı (TD) elektronik geçiş hesapları yapılmıştır. Spektroskopik ve hesapsal bulguların, kümelerin gelecekteki potansiyel uygulamaları için özelliklerinin belirlenebilmesi ve anlaşılmasına katkıda bulunacağı bulunacaktır.

Anahtar kelimeler: Nanomalzemeler, Kümeler, Geçiş Metali Aşılınmış Ana Grup Kümeleri, Nikel, Germanyum, Gaussian 09, Time-Dependent, Frekans, Spektroskopi.

to my precious family..

ACKNOWLEDGEMENTS

First of all, I would like to thank my advisor, Emren Nalbant Esentürk, for not only her endless support and guidance, but her friendship throughout my undergraduate and graduate years, and for being an excellent listener/advisor whenever I have trouble in something. I owe my knowledge on spectroscopy and Gaussian calculations to Okan Esentürk, who patiently gave me advices and always had an answer for any type of question. I cannot thank enough for his support.

I would like to send my appreciation to all former and current NanoClusMate members; Asude, Çağla, İlkem, Cansu and Doruk, for all their support and all the crazy times that we spent in the lab. Those memories will not vanish easily...

I would like to thank TÜBİTAK for the project funding (211T083) and scholarship. Moreover, TÜBİTAK ULAKBİM, High Performance and Grid Computing Center is also acknowledged for providing access to national high performance computer network.

I want to thank Prof. Dr. Ahmet M. Önal for the access to Fluorescence spectrophotometer, Prof. Dr. Şakir Erkoç and Mustafa Kurban from Physics Department for helping me solving the problems related to Gaussian calculations.

I may not find words to describe my precious friends; Nehir, Melis, Büke and Esra 'Öz', who made my life at METU more than just fun. Whatever happens in my life or wherever I go, they will always be my best friends and sisters. Unfortunately, it will not be so easy to replace or fill those memories with anything in my new life.

I also want to thank Seza, Merve, Ebru, Ozan, Hande and Emre for always supporting me and their true friendships. I wish I could have spent more time with them in my undergraduate years.

It is not possible to neglect thanking all members of METU Sub-Aqua Sports (SAS) for being amazing friends and letting me have unforgettable experiences beginning from the first week of my university life until now. I did not only have the chance to visit many places, but also succeeded as a team in many events which opened some important doors in my life. I would not be who I am without their contribution.

I had many precious memories with my crazy teammates of METU Futsal Team in my last 2 years at METU. I will truly miss our joyful trainings which gave me the chance to go back to my childhood one more time and have 19 more great friends.

Finally, I would like to thank my dear family; my mother and my father, my two big brothers abroad and their 3 little monsters (Kaan, Lara and Alhan), and my aunt for never leaving me alone in my life. I appreciate their existence.

TABLE OF CONTENTS

ABSTRACT	v
ÖZ.....	vii
ACKNOWLEDGEMENTS	x
LIST OF FIGURES.....	xv
LIST OF TABLES	xx
LIST OF EQUATIONS	xxi
LIST OF ABBREVIATIONS	xxii
CHAPTERS	
1. INTRODUCTION.....	1
1.1. The Motivation of This Dissertation	1
1.2. Clusters	3
1.2.1. Zintl Ion Clusters	5
1.3. Computational Studies.....	16
1.3.1. Density Functional Theory	16
1.3.2. Types of Calculations Carried Out	168
2. EXPERIMENTAL & COMPUTATIONAL.....	23
2.1. Experimental Part	23
2.2. Materials	23
2.3. Synthesis of K_4Ge_9	24
2.4. Synthesis of $[Ni_2Ge_9(PPh_3)]^{2-}$	24
2.5. Synthesis of $[Ni_6Ge_{13}(CO)_5]^{4-}$	25

2.6.	Sample Preparation for Spectroscopic Measurements	26
2.6.1.	Fourier Transform Infrared Spectroscopy	27
2.6.2.	Fluorescence Spectroscopy	28
2.6.3.	UV-Vis Spectroscopy	28
2.7.	Computational Part.....	29
2.7.1.	Geometry Optimization	31
2.7.2.	Frequency.....	32
2.7.3.	UV-Vis and Electronic Transitions.....	32
2.7.4.	Solvation Effect	33
3.	RESULTS & DISCUSSION.....	35
3.1.	Synthesis and Structures of $[\text{Ni}_2\text{Ge}_9(\text{PPh}_3)]^{2-}$ and $[\text{Ni}_6\text{Ge}_{13}(\text{CO})_5]^{4-}$ Zintl Ion Clusters.....	35
3.2.	Geometry Optimization of $[\text{Ni}_2\text{Ge}_9(\text{PPh}_3)]^{2-}$ and $[\text{Ni}_6\text{Ge}_{13}(\text{CO})_5]^{4-}$ Zintl Ion Clusters with Lanl2dz and CEP-121g Basis Sets.....	38
3.3.	Molecular Orbital (MO) Diagrams of $[\text{Ni}_2\text{Ge}_9(\text{PPh}_3)]^{2-}$ and $[\text{Ni}_6\text{Ge}_{13}(\text{CO})_5]^{4-}$ Zintl Ion Clusters.....	44
3.4.	UV-Vis, FTIR and Fluorescence Spectrometry Analyses of $[\text{Ni}_2\text{Ge}_9(\text{PPh}_3)]^{2-}$ and $[\text{Ni}_6\text{Ge}_{13}(\text{CO})_5]^{4-}$ Zintl Ion Clusters	46
3.4.1.	UV-Vis Spectrometry Analyses.....	47
3.4.1.1.	Results of Time-Dependent (TD) Electronic Transition Calculations for $[\text{Ni}_2\text{Ge}_9(\text{PPh}_3)]^{2-}$, $[\text{Ni}_2\text{Ge}_9(\text{CO})]^{2-}$ and $[\text{Ni}_6\text{Ge}_{13}(\text{CO})_5]^{4-}$	48
3.4.1.1.1.	Basis Set: Lanl2dz	49
3.4.1.1.2.	Basis Set: CEP-121g	53
3.4.2.	FTIR Spectrometry Analyses.....	55
3.4.2.1.	FTIR Spectra in DMF with TPX Windows	56

3.4.2.2.	FTIR Spectra in Paraffin Oil with TPX and KBr Windows	61
3.4.3.	Results of Frequency Calculations for $[\text{Ni}_2\text{Ge}_9(\text{PPh}_3)]^{2-}$, $[\text{Ni}_2\text{Ge}_9(\text{CO})]^{2-}$ and $[\text{Ni}_6\text{Ge}_{13}(\text{CO})_5]^{4-}$	67
3.4.3.1.	Basis Set: Lanl2dz	68
3.4.3.1.1.	Comparison of Lanl2dz Calculations with Experimental Results....	72
3.4.3.2.	Basis Set: CEP-121g	83
3.4.3.2.1.	Comparison of CEP-121g Calculations with Experimental Results	86
3.4.4.	Fluorescence Spectrometry Analyses	96
4.	CONCLUSIONS	101
	REFERENCES	105
	APPENDICES	113
A.	DATA RELATIVE TO CHAPTER 1	113
B.	DATA RELATIVE TO CHAPTER 3	117

LIST OF FIGURES

FIGURES

Figure 1.1. Potential application areas of assembled cluster materials.....	2
Figure 1.2. Examples of a) high-valence b) low-valence clusters	4
Figure 1.3. Structures of a) Buckminsterfullerene (C ₆₀) b) Zintl anion [Ge ₁₀] ²⁻	5
Figure 1.4. Structures of a) 2,2,2-crypt b) 18-crown-6.....	7
Figure 1.5. Common structures of Zintl anions	9
Figure 1.6. Structure of [E ₉ M(CO) ₃] ⁴⁻ (E = Pb, Sn; M = Cr, Mo, W).....	11
Figure 1.7. Ortep drawing of [Pt@Pb ₁₂] ²⁻ ion.....	12
Figure 1.8. Ortep drawing of [Ni ₂ @Sn ₁₇] ⁴⁻ ion.....	13
Figure 1.9. Examples to ligand-free transition metal integrated Germanium clusters.	14
Figure 1.10. [Sn@Cu ₁₂ @Sn ₂₀] ¹²⁻	15
Figure 1.11. Suggested sequence of calculations for any molecule.....	19
Figure 2.1. Schematic representation of synthetic pathway of Ni-Ge clusters (en: ethylenediamine).....	26
Figure 2.2. FTIR sample holders.....	27
Figure 2.3. Calculation flow for both basis sets.....	31
Figure 3.1. Ortep drawings of a) [Ni ₂ Ge ₉ (PPh ₃)] ²⁻ b) [Ni ₆ Ge ₁₃ (CO) ₅] ⁴⁻	36
Figure 3.2. Visualized structure of [Ni ₂ Ge ₉ (CO)] ²⁻	38
Figure 3.3. Visualized structure of [Ni ₂ Ge ₉ (PPh ₃)] ²⁻	39
Figure 3.4. Visualized structure of [Ni ₆ Ge ₁₃ (CO) ₅] ⁴⁻	42
Figure 3.5. MO diagrams of [Ni ₂ Ge ₉ (PPh ₃)] ²⁻ in DMF with a) Lanl2dz b) CEP-121g	45
Figure 3.6. MO diagrams of [Ni ₆ Ge ₁₃ (CO) ₅] ⁴⁻ in DMF with a) Lanl2dz b) CEP-121g	46

Figure 3.7. UV-Vis spectra of $[\text{Ni}_2\text{Ge}_9(\text{PPh}_3)]^{2-}$ and $[\text{Ni}_6\text{Ge}_{13}(\text{CO})_5]^{4-}$ cluster crystals in DMF	48
Figure 3.8. Lanl2dz TD spectrum of $[\text{Ni}_2\text{Ge}_9(\text{PPh}_3)]^{2-}$ in DMF with 750 transitions (broadened data in blue solid line, vibrations in red bars)	50
Figure 3.9. Lanl2dz TD spectra of a) $[\text{Ni}_2\text{Ge}_9(\text{PPh}_3)]^{2-}$ with 750 transitions b) $[\text{Ni}_2\text{Ge}_9(\text{CO})]^{2-}$ with 750 transitions c) $[\text{Ni}_6\text{Ge}_{13}(\text{CO})_5]^{4-}$ with 500 transitions in gas phase (blue) and in DMF (red).....	51
Figure 3.10. Experimental UV spectra of $[\text{Ni}_2\text{Ge}_9(\text{PPh}_3)]^{2-}$ (blue) and $[\text{Ni}_6\text{Ge}_{13}(\text{CO})_5]^{4-}$ (red) as solid lines; and computational TD spectra of $[\text{Ni}_2\text{Ge}_9(\text{PPh}_3)]^{2-}$ (blue), $[\text{Ni}_6\text{Ge}_{13}(\text{CO})_5]^{4-}$ (red) and $[\text{Ni}_2\text{Ge}_9(\text{CO})]^{2-}$ (cyan) in DMF as dash lines with Lanl2dz in 200-800 nm region.	53
Figure 3.11. CEP-121g TD spectra of a) $[\text{Ni}_2\text{Ge}_9(\text{PPh}_3)]^{2-}$ with 500 transitions b) $[\text{Ni}_2\text{Ge}_9(\text{CO})]^{2-}$ with 750 transitions c) $[\text{Ni}_6\text{Ge}_{13}(\text{CO})_5]^{4-}$ with 500 transitions in gas phase (blue) and in DMF (red).....	54
Figure 3.12. Experimental UV spectra of $[\text{Ni}_2\text{Ge}_9(\text{PPh}_3)]^{2-}$ (blue) and $[\text{Ni}_6\text{Ge}_{13}(\text{CO})_5]^{4-}$ (red) as solid lines; and computational TD spectra of $[\text{Ni}_2\text{Ge}_9(\text{PPh}_3)]^{2-}$ (blue), $[\text{Ni}_6\text{Ge}_{13}(\text{CO})_5]^{4-}$ (red) and $[\text{Ni}_2\text{Ge}_9(\text{CO})]^{2-}$ (cyan) in DMF as dash lines with CEP-121g in 200-800 nm region.	55
Figure 3.13. DMF absorption spectrum in a) Linear scale b) Log scale	57
Figure 3.14. Transmission spectra of precursors (K_4Ge_9 , $\text{Pt}(\text{PPh}_3)_4$, $\text{Ni}(\text{CO})_2(\text{PPh}_3)_2$ as thin solid lines) and clusters ($[\text{Ni}_2\text{Ge}_9(\text{PPh}_3)]^{2-}$, $[\text{Ni}_6\text{Ge}_{13}(\text{CO})_5]^{4-}$ as solid lines) in DMF with TPX windows, $310\text{-}70\text{ cm}^{-1}$	58
Figure 3.15. Transmission spectra of precursors (K_4Ge_9 , $\text{Pt}(\text{PPh}_3)_4$, $\text{Ni}(\text{CO})_2(\text{PPh}_3)_2$ shown as thin solid lines) and clusters ($[\text{Ni}_2\text{Ge}_9(\text{PPh}_3)]^{2-}$, $[\text{Ni}_6\text{Ge}_{13}(\text{CO})_5]^{4-}$ shown as solid lines) in DMF with TPX windows, $710\text{-}370\text{ cm}^{-1}$	59
Figure 3.16. Transmission spectra of precursors (K_4Ge_9 , $\text{Pt}(\text{PPh}_3)_4$, $\text{Ni}(\text{CO})_2(\text{PPh}_3)_2$ as thin solid lines) and clusters ($[\text{Ni}_2\text{Ge}_9(\text{PPh}_3)]^{2-}$, $[\text{Ni}_6\text{Ge}_{13}(\text{CO})_5]^{4-}$ as solid lines) in DMF with TPX windows, $2100\text{-}1800\text{ cm}^{-1}$	61
Figure 3.17. Absorption spectra of paraffin oil with KBr and TPX windows	62

Figure 3.18. Transmission spectra of precursors (K_4Ge_9 , $Pt(PPh_3)_4$, $Ni(CO)_2(PPh_3)_2$ as thin solid lines) and clusters ($[Ni_2Ge_9(PPh_3)]^{2-}$, $[Ni_6Ge_{13}(CO)_5]^{4-}$ as solid lines) in paraffin oil with TPX windows, 600-50 cm^{-1}	64
Figure 3.19. Transmission spectra of precursors (K_4Ge_9 , $Pt(PPh_3)_4$, $Ni(CO)_2(PPh_3)_2$ as thin solid lines) and clusters ($[Ni_2Ge_9(PPh_3)]^{2-}$, $[Ni_6Ge_{13}(CO)_5]^{4-}$ as solid lines) in paraffin oil with KBr windows, 800-300 cm^{-1}	65
Figure 3.20. Transmission spectra of precursors (K_4Ge_9 , $Pt(PPh_3)_4$, $Ni(CO)_2(PPh_3)_2$ as thin solid lines) and clusters ($[Ni_2Ge_9(PPh_3)]^{2-}$, $[Ni_6Ge_{13}(CO)_5]^{4-}$ as solid lines) in paraffin oil with KBr windows, 1350-800 cm^{-1}	66
Figure 3.21. Transmission spectra of precursors (K_4Ge_9 , $Pt(PPh_3)_4$, $Ni(CO)_2(PPh_3)_2$ as thin solid lines) and clusters ($[Ni_2Ge_9(PPh_3)]^{2-}$, $[Ni_6Ge_{13}(CO)_5]^{4-}$ as solid lines) in paraffin oil with a) KBr windows b) TPX windows, 2100-1800 cm^{-1}	67
Figure 3.22. Computational IR spectra of $[Ni_2Ge_9(PPh_3)]^{2-}$ in DMF and gas phase with Lanl2dz in 1750-20 cm^{-1} region.	69
Figure 3.23. Computational IR spectra of $[Ni_2Ge_9(CO)]^{2-}$ in DMF and gas phase with Lanl2dz in 1850-1600 cm^{-1} and 1625-20 cm^{-1} regions.	70
Figure 3.24. Computational IR spectra of $[Ni_6Ge_{13}(CO)_5]^{4-}$ in DMF and gas phase with Lanl2dz in 1850-1600 cm^{-1} and 600-20 cm^{-1} regions.	72
Figure 3.25. Experimental FTIR spectra of $[Ni_2Ge_9(PPh_3)]^{2-}$ (blue) and $[Ni_6Ge_{13}(CO)_5]^{4-}$ (red) as solid lines with TPX windows; and computational IR spectra of $[Ni_2Ge_9(PPh_3)]^{2-}$ (blue), $[Ni_6Ge_{13}(CO)_5]^{4-}$ (red) and $[Ni_2Ge_9(CO)]^{2-}$ (cyan) as dash lines with Lanl2dz in 350-20 cm^{-1} region.	74
Figure 3.26. Experimental FTIR spectra of K_4Ge_9 (grey), $Pt(PPh_3)_4$ (wine), $Ni(CO)_2(PPh_3)_2$ (dark cyan) as thin solid lines, $[Ni_2Ge_9(PPh_3)]^{2-}$ (blue) and $[Ni_6Ge_{13}(CO)_5]^{4-}$ (red) as solid lines with TPX windows; and computational IR spectra of $[Ni_2Ge_9(PPh_3)]^{2-}$ (blue), $[Ni_6Ge_{13}(CO)_5]^{4-}$ (red) and $[Ni_2Ge_9(CO)]^{2-}$ (cyan) as dash lines with Lanl2dz in 700-350 cm^{-1} region.	77
Figure 3.27. Experimental FTIR spectra of $[Ni_2Ge_9(PPh_3)]^{2-}$ (blue) and $[Ni_6Ge_{13}(CO)_5]^{4-}$ (red) as solid lines with KBr windows; and computational IR	

spectra of $[\text{Ni}_2\text{Ge}_9(\text{PPh}_3)]^{2-}$ (blue), $[\text{Ni}_6\text{Ge}_{13}(\text{CO})_5]^{4-}$ (red) and $[\text{Ni}_2\text{Ge}_9(\text{CO})]^{2-}$ (cyan) as dash lines with Lanl2dz in 800-300 cm^{-1} region.....	79
Figure 3.28. Experimental FTIR spectra of K_4Ge_9 (grey), $\text{Pt}(\text{PPh}_3)_4$ (wine), $\text{Ni}(\text{CO})_2(\text{PPh}_3)_2$ (dark cyan) as thin solid lines, $[\text{Ni}_2\text{Ge}_9(\text{PPh}_3)]^{2-}$ (blue) and $[\text{Ni}_6\text{Ge}_{13}(\text{CO})_5]^{4-}$ (red) as solid lines with KBr windows; and computational IR spectra of $[\text{Ni}_2\text{Ge}_9(\text{PPh}_3)]^{2-}$ (blue), $[\text{Ni}_6\text{Ge}_{13}(\text{CO})_5]^{4-}$ (red) and $[\text{Ni}_2\text{Ge}_9(\text{CO})]^{2-}$ (cyan) as dash lines with Lanl2dz in 1350-800 cm^{-1} region.....	81
Figure 3.29. Experimental FTIR spectra of $[\text{Ni}_2\text{Ge}_9(\text{PPh}_3)]^{2-}$ (blue) and $[\text{Ni}_6\text{Ge}_{13}(\text{CO})_5]^{4-}$ (red) as solid lines with a) KBr windows b) TPX windows; and computational IR spectra of $[\text{Ni}_2\text{Ge}_9(\text{PPh}_3)]^{2-}$ (blue), $[\text{Ni}_6\text{Ge}_{13}(\text{CO})_5]^{4-}$ (red) and $[\text{Ni}_2\text{Ge}_9(\text{CO})]^{2-}$ (cyan) as dash lines with Lanl2dz in 2100-1500 cm^{-1} region.	82
Figure 3.30. Computational IR spectra of $[\text{Ni}_2\text{Ge}_9(\text{PPh}_3)]^{2-}$ in DMF and gas phase with CEP-121g in 1750-20 cm^{-1} region.	84
Figure 3.31. Computational IR spectra of $[\text{Ni}_2\text{Ge}_9(\text{CO})]^{2-}$ in DMF and gas phase with CEP-121g in 1850-1600 cm^{-1} and 1625-20 cm^{-1} regions.....	85
Figure 3.32. Computational IR spectra of $[\text{Ni}_6\text{Ge}_{13}(\text{CO})_5]^{4-}$ in DMF and gas phase with CEP-121g in 1800-1550 cm^{-1} and 600-20 cm^{-1} regions.....	86
Figure 3.33. Experimental FTIR spectra of $[\text{Ni}_2\text{Ge}_9(\text{PPh}_3)]^{2-}$ (blue) and $[\text{Ni}_6\text{Ge}_{13}(\text{CO})_5]^{4-}$ (red) as solid lines with TPX windows; and computational IR spectra of $[\text{Ni}_2\text{Ge}_9(\text{PPh}_3)]^{2-}$ (blue), $[\text{Ni}_6\text{Ge}_{13}(\text{CO})_5]^{4-}$ (red) and $[\text{Ni}_2\text{Ge}_9(\text{CO})]^{2-}$ (cyan) as dash lines with CEP-121g in 350-20 cm^{-1} region.	88
Figure 3.34. Experimental FTIR spectra of K_4Ge_9 (grey), $\text{Pt}(\text{PPh}_3)_4$ (wine), $\text{Ni}(\text{CO})_2(\text{PPh}_3)_2$ (dark cyan) as thin solid lines, $[\text{Ni}_2\text{Ge}_9(\text{PPh}_3)]^{2-}$ (blue) and $[\text{Ni}_6\text{Ge}_{13}(\text{CO})_5]^{4-}$ (red) as solid lines with TPX windows; and computational IR spectra of $[\text{Ni}_2\text{Ge}_9(\text{PPh}_3)]^{2-}$ (blue), $[\text{Ni}_6\text{Ge}_{13}(\text{CO})_5]^{4-}$ (red) and $[\text{Ni}_2\text{Ge}_9(\text{CO})]^{2-}$ (cyan) as dash lines with CEP-121g in 700-350 cm^{-1} region.	91
Figure 3.35. Experimental FTIR spectra of $[\text{Ni}_2\text{Ge}_9(\text{PPh}_3)]^{2-}$ (blue) and $[\text{Ni}_6\text{Ge}_{13}(\text{CO})_5]^{4-}$ (red) as solid lines with KBr windows; and computational IR spectra of $[\text{Ni}_2\text{Ge}_9(\text{PPh}_3)]^{2-}$ (blue), $[\text{Ni}_6\text{Ge}_{13}(\text{CO})_5]^{4-}$ (red) and $[\text{Ni}_2\text{Ge}_9(\text{CO})]^{2-}$ (cyan) as dash lines with CEP-121g in 800-300 cm^{-1} region.	93

Figure 3.36. Experimental FTIR spectra of K_4Ge_9 (grey), $Pt(PPh_3)_4$ (wine), $Ni(CO)_2(PPh_3)_2$ (dark cyan) as thin solid lines, $[Ni_2Ge_9(PPh_3)]^{2-}$ (blue) and $[Ni_6Ge_{13}(CO)_5]^{4-}$ (red) as solid lines with KBr windows; and computational IR spectra of $[Ni_2Ge_9(PPh_3)]^{2-}$ (blue), $[Ni_6Ge_{13}(CO)_5]^{4-}$ (red) and $[Ni_2Ge_9(CO)]^{2-}$ (cyan) as dash lines with CEP-121g in $1350-800\text{ cm}^{-1}$ region..... 95

Figure 3.37. Experimental FTIR spectra of $[Ni_2Ge_9(PPh_3)]^{2-}$ (blue) and $[Ni_6Ge_{13}(CO)_5]^{4-}$ (red) as solid lines with a) KBr windows b) TPX windows; and computational IR spectra of $[Ni_2Ge_9(PPh_3)]^{2-}$ (blue), $[Ni_6Ge_{13}(CO)_5]^{4-}$ (red) and $[Ni_2Ge_9(CO)]^{2-}$ (cyan) as dash lines with CEP-121g in $2100-1500\text{ cm}^{-1}$ region. 96

Figure 3.38. Fluorescence spectra of $[Ni_2Ge_9(PPh_3)]^{2-}$ in DMF and only DMF..... 98

Figure 3.39. Fluorescence spectra of $[Ni_6Ge_{13}(CO)_5]^{4-}$ in DMF and only DMF 99

LIST OF TABLES

TABLES

Table 1.1. The terminology used in Wade-Mingos rules (n = number of vertex).....	8
Table 2.1. Examples to successful and unsuccessful job submissions	30
Table 3.1. Comparison of bond lengths calculated with both basis sets: [Ni ₂ Ge ₉ (PPh ₃)] ²⁻	40
Table 3.2. Comparison of bond angles calculated with both basis sets: [Ni ₂ Ge ₉ (PPh ₃)] ²⁻	41
Table 3.3. Comparison of bond lengths calculated with both basis sets: [Ni ₆ Ge ₁₃ (CO) ₅] ⁴⁻	43
Table 3.4. Comparison of bond angles calculated with both basis sets: [Ni ₆ Ge ₁₃ (CO) ₅] ⁴⁻	44
Table 3.5. Calculated maximum transition states of [Ni ₂ Ge ₉ (PPh ₃)] ²⁻ , [Ni ₂ Ge ₉ (CO)] ²⁻ and [Ni ₆ Ge ₁₃ (CO) ₅] ⁴⁻ with Lan12dz and CEP-121g	49
Table 3.6. Regions with KBr and TPX windows	62
Table 3.7. Differences in selected peak positions in Figure 3.25.	75
Table 3.8. Differences in selected peak positions in Figure 3.26.	78
Table 3.9. Differences in selected peak positions in Figure 3.27.	80
Table 3.10. Differences in selected peak positions in Figure 3.33.	89
Table 3.11. Differences in selected peak positions in Figure 3.34.	92
Table 3.12. Differences in selected peak positions in Figure 3.35.	94

LIST OF EQUATIONS

EQUATIONS

Equation 1.1. Titration of Polylead anions.....	6
Equation 2.1. Balanced equation for the synthesis of K_4Ge_9	24
Equation 2.2. Balanced equation for the synthesis of $[Ni_2Ge_9(PPh_3)]^{2-}$	25
Equation 2.3. Balanced equation for the synthesis of $[Ni_6Ge_{13}(CO)_5]^{4-}$	25

LIST OF ABBREVIATIONS

°C	degrees Celsius
18-crown-6	1,4,7,10,13,16-hexaoxacyclooctadecane
2,2,2-crypt	4,7,13,16,21,24-hexaoxa-1,10-diazabicyclo[8,8,8]-hexacosane
Å	Angstrom
A	bond angle
B	bond length
ca.	circa
CIS	Configuration Interaction Singles
Cp	cyclopentadienyl
D	dihedral angle
DFT	Density Functional Theory
DMF	dimethylformamide
ECP	Effective Core Potential
EDX	Energy Dispersive X-ray Spectroscopy
en	ethylenediamine
ESI	Electrospray Ionization
Et	ethyl
Freq	frequency
FTIR	Fourier Transform Infrared Spectroscopy
GB	gigabyte
HF	Hartree-Fock
HOMO	Highest Occupied Molecular Orbital
K	Kelvin
LUMO	Lowest Unoccupied Molecular Orbital
M	metal
<i>m/z</i>	mass to charge ratio

MB	megabyte
mg	milligram
mL	milliliter
mmol	millimole
MO	molecular orbital
Mw	million words
NMR	Nuclear Magnetic Resonance
Opt	optimization
PE	Photoelectron Spectroscopy
PE	polyethylene
PPh₃	triphenylphosphine
RMS	root mean square
s	strong
SCRF	Self-Consistent Reaction Field
sh	sharp
SSH	secure shell
TD	Time-Dependent
TM	transition metal
TPX	polymethylpentene (Trademark of Mitsui Chemicals)
UV-Vis	Ultraviolet-Visible
w	weak
ZINDO	Zerner's Intermediate Neglect of Differential Overlap

CHAPTER 1

INTRODUCTION

1.1. The Motivation of This Dissertation

The growing interest toward miniaturization of devices directs researchers to develop new materials with enhanced performances. This quest makes nanomaterials focus of intense research and have them active roles in wide variety of areas such as electronics, medicine and catalysis to name a few. The control over properties such as structural, electronic, optical can lead to discovery of new high-performance materials to be used in nanotechnology. Making rationally designed materials with well-understood properties is the major challenge in this area of research.

Clusters, aggregates of atoms, possess the potential for designing and modifying properties (cluster size, chemical identity and surface structures) toward a particular application. They can be used as “artificial atoms” in the “bottom-up” approach to prepare new nanomaterials.¹ Therefore, cluster science aim to discover new clusters with special electronic and structural stabilities as well as with thoroughly investigated properties so that they can be used as seeds for preparing well-tailored nanomaterials. The discovery of C₆₀-fullerene motivated researchers to synthesize new clusters with exciting properties and make novel materials from these clusters.² Preparation of cluster assembled materials and further advances in cluster science evident their potential for advanced materials applications which include chemical sensors, solar cells, bimetallic catalysts, and electronic device applications.²(Figure 1.1.)

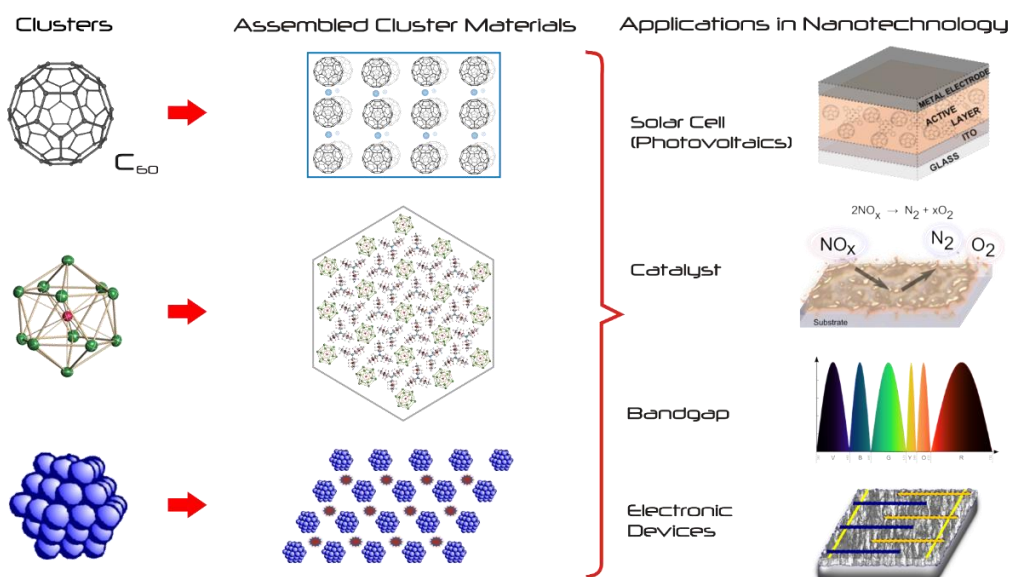


Figure 1.1. Potential application areas of assembled cluster materials.³

Among all cluster types, polyatomic main group clusters (Zintl ion clusters) are enjoying the well-deserved attention due to their non-traditional structures, special spectroscopic properties and electronic stabilities. They have considerable potential to be used as “building blocks” in the cluster assembled materials or nucleation sites for nanoparticle growth.⁴ Various types of Zintl ion clusters have been successfully isolated and their unique bonding natures have been revealed up-to-date.^{5–18} Spectroscopic studies such as with mass and NMR spectroscopy have been performed to complement the structural analysis and demonstrate unique dynamic properties of these clusters.^{13,19–32} However, knowledge of some other important properties (i.e. vibrational and optical) crucial for potential applications such as photovoltaic devices, light - emitting diodes and lasers, are lacking. Any information obtained from the investigation of these properties is believed to have significant

impact on understanding, controlling and prediction of the materials that formed by the use of these clusters.

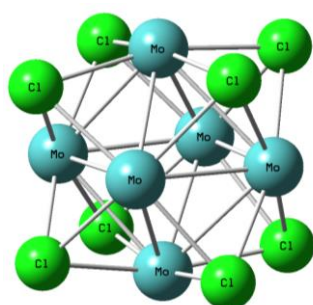
This thesis study focuses on both synthesis of nickel integrated germanium clusters; $[\text{Ni}_2\text{Ge}_9(\text{PPh}_3)]^{2-}$ and $[\text{Ni}_6\text{Ge}_{13}(\text{CO})_5]^{4-}$, and their spectroscopic characterization that has never investigated. FTIR, UV-Vis and Fluorescence spectroscopic studies have been performed to reveal these clusters' vibrational and optical properties. Computational studies have also been done in conjunction with the experimental ones to interpret the data obtained from spectroscopic studies as well as characterizing electronic properties. These studies are believed to provide deeper understanding of properties and make contributions to the development of existent knowledge about the clusters in Zintl ion library.

1.2. Clusters

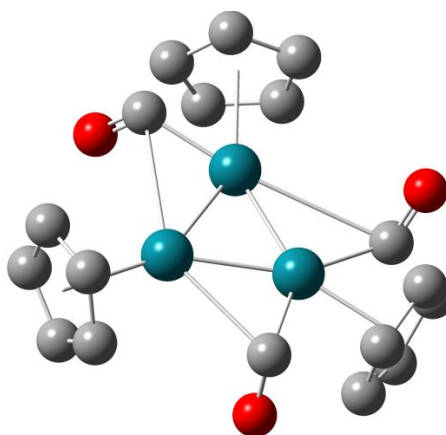
Clusters are groups of atoms connected to each other by direct and substantial element-to-element bonds forming molecular complexes having triangular, cyclic or cage-like structures.³³ The direct linkage between these atoms results in a polyatomic nucleus which generally shows different properties than its constituents.¹ These properties change with the size, surface structures and of course the elemental character of the cluster. The possibility of control of these properties makes them very desirable for potential applications such as chemical sensors³⁴, flat-panel displays³⁵, catalysis³⁶, and quantum computers³⁷ to name a few.

The main disadvantage of clusters is their tendency to agglomerate. Therefore, they need to be stabilized to prevent the formation of larger particles or even a bulk material. One way of achieving this is to coat clusters with ligands, surfactants or polymers. Another way is to synthesize individually stable (ligand-free or naked) clusters to minimize the inter-cluster interaction and resist coalescence.^{38,39}

Clusters which are prepared from d-metal elements are generally ligand stabilized and can be categorized as high valence and low valence.⁴⁰ Clusters formed by the early d-block elements are called high valence clusters as the metal atoms forming the network tend to have positive oxidation states. σ -donor or π -donor type of ligands can provide electrons to the low lying orbitals of these electron deficient metals. $[\text{Mo}_6\text{Cl}_8]^{4+}$, $[(\text{Cl})_3\text{W}(\mu\text{-Cl})_3\text{W}(\text{Cl})_3]^{3-}$ can be given as examples for these types of clusters.³³(Figure 1.2. a) On the other hand, low-valence clusters are formed by electron rich late d-block metals having zero or negative oxidation states and ligands of π -acceptor type. Some examples of these types of clusters are $\text{Rh}_3(\text{CO})_3(\pi\text{-Cp})_3$, $\text{Ru}_6\text{C}(\text{CO})_{14}(\text{C}_6\text{H}_3\text{Me}_3)$.³³(Figure 1.2. b)



a) $[\text{Mo}_6\text{Cl}_8]^{4+}$



b) $\text{Rh}_3(\text{CO})_3(\pi\text{-Cp})_3$

Figure 1.2. Examples of **a)** high-valence **b)** low-valence clusters

Clusters which are stabilized without the coordination of ligands are called as ligand free or naked clusters. These types of clusters are generally dominated by p-block elements. The C_{60} -fullerenes^{41,42} and metcars (metallocarbohedrene)⁴³ family of

TM₈C₁₂ cages (TM = a transition metal atom) are some of the most celebrated examples of these types of clusters. (Figure 1.3. a) Another family of clusters which is very rich in ligand-free members are Zintl ions such as [Ge₁₀]²⁻, [P₇]³⁻, [Pb]₅⁻, [Sn₅]⁻ and will be discussed further in the following section.⁴⁴ (Figure 1.3. b)

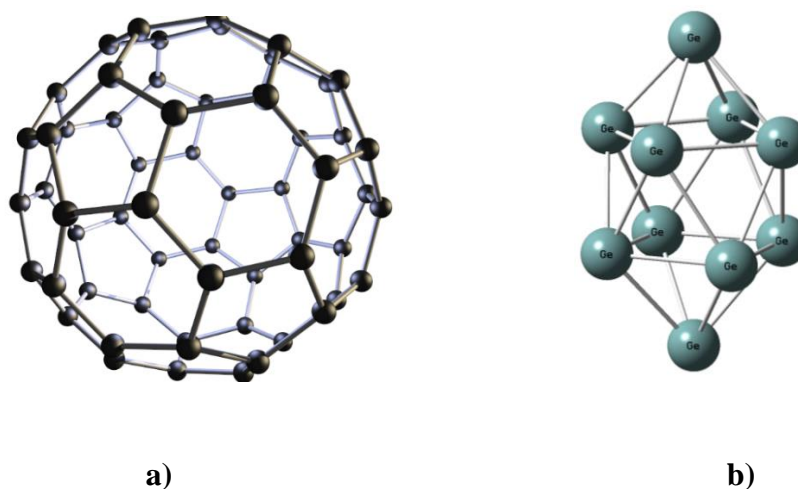


Figure 1.3. Structures of a) Buckminsterfullerene (C₆₀)⁴⁵ b) Zintl anion [Ge₁₀]²⁻⁴⁴

1.2.1. Zintl Ion Clusters

The solvated polyatomic anions of main group elements (from Group 13 to 16) are known to be Zintl ions. They are first discovered by Johannes in 1891 when he observed the color of sodium in liquid ammonia solution change from blue to green with the addition of elemental lead.⁴⁶ Further studies conducted by Zintl, Smyth, Kraus and co-workers revealed that the color change was due to reduction of metals to highly charged homoatomic polyatoms.⁴⁷⁻⁵⁰ Eduard Zintl discovered the composition of these anionic species in 1930s by using potentiometric titrations of

sodium in liquid ammonia with a salt of the metal (PbI_2). Polylead anions are formed from the titration as shown in equation 1.1.⁵¹



Extensive studies on the synthesis and characterization of main group polyanions have been performed and varieties of them have been prepared by Zintl and co-workers. Therefore, these highly charged polyanions have been named after Zintl as “Zintl ions”. Some examples of these ions are $[\text{Sn}_9]^{4-}$, $[\text{Pb}_9]^{4-}$, $[\text{As}_7]^{3-}$ and $[\text{Sb}_7]^{3-}$, $[\text{Bi}_3]^{3-}$.⁴⁷⁻⁵¹ The first structural characterization of a Zintl ion was reported by Kummer and Diehl. The single crystal X-ray structure revealed the chemical formula of the crystals as $\text{Na}_4(\text{en})_7\text{Sn}_9$ where the Zintl ion identity was verified with the presence of Sn_9^{4-} anion.⁵²

Zintl and co-workers also discovered that binary intermetallic phases such as Na_4Pb_9 gave the same solutions when dissolved in liquid ammonia, which made the synthesis of cluster relatively easy when used as a precursor.⁵³ These polar intermetallic compounds are called “Zintl phases” and are generally composed of an electropositive s-block element and an electronegative p-block element. They are in the form of A_xE_y (examples include K_4Sn_9 , K_3P_7) and are generally obtained by heating a stoichiometric mixture of the elements for several hours under an inert atmosphere at very high temperatures. Contrary to most metals they were found out to be brittle and display semiconducting properties.⁵⁴

Although Zintl ion clusters were discovered in 1930s, they were not widely explored until 1970s due to the challenges in synthesis and high air-sensitivity of these compounds. Corbett and co-workers made an important discovery towards isolation of these compounds with the crystallization of $[\text{K}(2,2,2\text{-crypt})]_3[\text{Sb}_7]$ in 1975.⁵⁵ The crystal growth is promoted by adding alkali metal isolating agents such as [2,2,2]-crypt or 18-crown-6. Stable complexes with alkali metal cations and macro-cyclic

polyethers are formed preventing the transfer of electrons from the Zintl anions back to the alkali metal. The [2,2,2]-crypt acts as a sequestering agent by separating the ion pairs of alkali metal and Zintl ions. This provides an enhancement in the solubility and crystallization of Zintl ions.⁵⁶

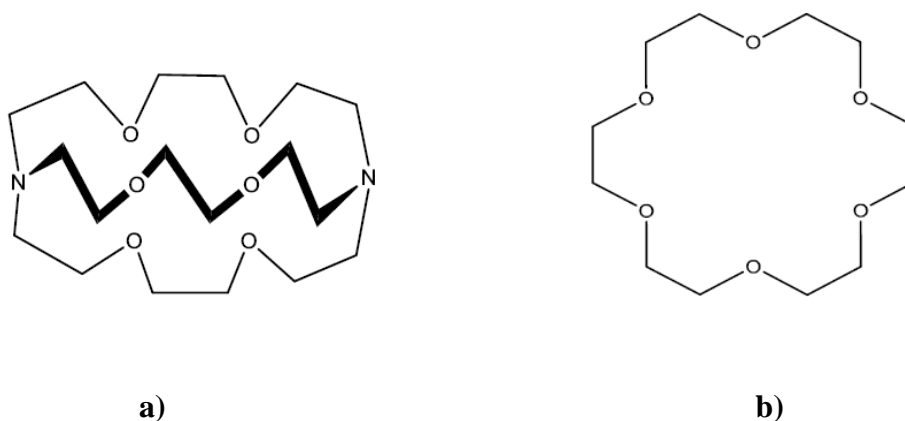


Figure 1.4. Structures of **a)** 2,2,2-crypt **b)** 18-crown-6

Numerous Group 14 and Group 15 Zintl salts and naked clusters were isolated after the discovery of Corbett and co-workers. E_9^{4-} ($E = \text{Sn, Ge, Pb}$)^{55,57-61}, Ge_9^{2-} ⁵⁵ and E_7^{3-} ($E = \text{P, As, Sb}$)^{62-65,56} are some of the first examples of isolated Zintl ion clusters.

The elements of Group 15 (Pnictogens) are more likely to form polycyclic structures resembling to hydrocarbons due to isoelectronic behavior of E to CH and E^- to CH_2 where E is P or As. Nortricyclanes E_7^{3-} ($E = \text{P, As, Sb}$) can be given as examples for polyanionic clusters of Group 15. Group 15 Zintl ions are electron precise and have E-E bonds with $2c-2e^-$ covalent bonds while Group 14 Zintl ions are electron

deficient and are analogous to borane clusters. Therefore, Wade-Mingos rules apply for the explanation of the bonding and each Group 14 element donates two electrons to the cluster.^{66,67}

In deltahedral clusters, bonding is achieved via delocalized electrons. Thus, instead of using the octet rule, electrons are counted by using Wade-Mingos rules. Based on the vertex number and total charge of the cluster, structures of the clusters are described as *closo*, *hypo-closo*, *nido* and *arachno* type deltahedra.⁶⁶(Table 1.1.)

Table 1.1. The terminology used in Wade-Mingos rules (n = number of vertex)

Type	Total Number of Skeletal Electrons
<i>closo</i>	$2n+2$
<i>hypo-closo</i>	$2n$ or $2n-2$
<i>nido</i>	$2n+4$
<i>arachno</i>	$2n+6$

For instance, E_9^{2-} consists of 9 vertices (occupied by Group 14 element and each contribute 2 electron to the skeleton) and -2 charge. Total number of skeletal electrons becomes 2×9 (number of vertex or atoms on the skeleton) + 2 (charge) = 20 and the cluster obeys $2n+2$ type representing *closo* deltahedra.

The Group 14 Zintl ions most commonly form deltahedral-like, nine atom clusters such as $[E_9]^{4-}$ where E is Si, Ge, Sn or Pb. (Figure 1.4.) The crystals of these cluster ions are obtained in solvents such as liquid ammonia, ethylenediamine (en) or dimethylformamide (DMF). The structures of these nine atom clusters are commonly either monocapped square antiprism with C_{4v} symmetry ($[Pb_9]^{4-}$) or tricapped

trigonal prism with the symmetry of D_{3h} ($[Sn_9]^{4-}$).⁴⁴ The structures are quite fluxional in solution and have an exchange process between symmetries with the bond formation and breaking.^{58,68,69} Therefore, these nine atom clusters are extensively used as precursors for making new Zintl ion clusters with various bonding natures. The most common homoatomic Zintl ion clusters that are structurally characterized in solutions are shown in Figure 1.5.^{44,70} Among them, $closo-[Pb_{10}]^{2-}$ with bicapped quadratic-antiprism shape is the largest homoatomic Group 14 cluster isolated up to date.⁷¹ To our knowledge, no homoatomic cluster of the form $[E_{12}]^{2-}$ has been isolated in solid state or solution, yet it is observed in gas phase with mass spectroscopy analysis.^{18,72}

- I. $[E_4]^{4-}$ where E = Sn, Pb⁴⁴
- II. $[E_5']^{2-}$, $[E_9']^{2-}$, $[E_9']^{3-}$, $[E_9']^{4-}$ where E' = Si, Ge, Sn, Pb⁷⁰
- III. $[E_{10}']$ where E = Ge, Pb⁴⁴

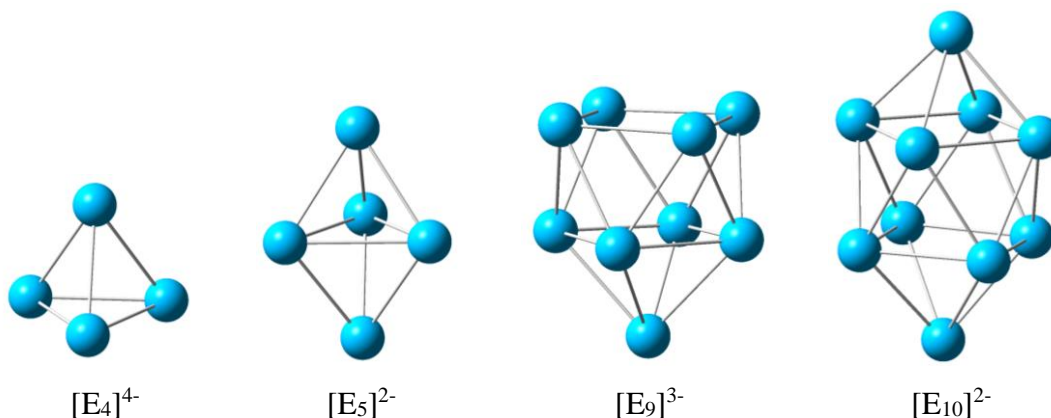


Figure 1.5. Common structures of Zintl anions^{44,70}

Besides individual homoatomic Zintl ion clusters, the ones exo-bonded to each other to form dimeric, trimeric and polymeric structures such as $[(\text{Ge}_9)_2]^{6-}$, $[(\text{Ge}_9)_3]^{6-}$, $[\infty(\text{Ge}_9)^{2-}]$, respectively, have been isolated.⁷³⁻⁷⁶ The isolation of these structures demonstrates the possibility of controlled preparation of new materials in nano or micro scale.

The simplicity and high reactivity of homoatomic, naked Group 14 clusters have yielded isolation of wide variety of new Zintl ion clusters. Their reactions with transition metals opened up the new research avenue and lead to isolation of clusters with exciting properties. Haushalter et al. have isolated the first example of this type of clusters.⁷⁷ The chromium-plumbide cluster, $[\text{Pb}_9\text{Cr}(\text{CO})_3]^{4-}$ has square antiprism unit of Pb_9 capped by $\text{Cr}(\text{CO})_3$ unit resulting *closo* geometry. Subsequently, derivatives of this cluster anion (i.e. $[\text{Sn}_9\text{Cr}(\text{CO})_3]^{4-}$, $[\text{Sn}_9\text{M}(\text{CO})_3]^{4-}$ where $\text{M} = \text{Cr}, \text{Mo}, \text{W}$) have been isolated.⁷⁸ (Figure 1.6.)

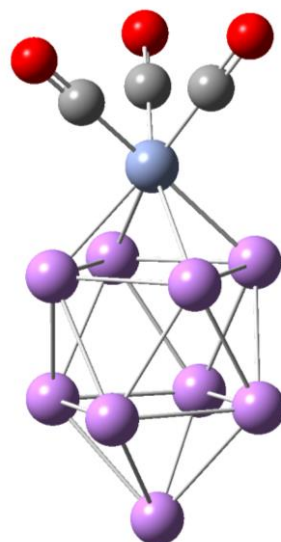


Figure 1.6. Structure of $[E_9M(CO)_3]^{4-}$ ($E = Pb, Sn$; $M = Cr, Mo, W$)^{77,78}

Integrating transition metal to Zintl ion clusters have become very attractive research area due to the potential of these new types of clusters to be used to make bimetallic catalysts and nanomaterials.^{69,79} More recently, another type of transition metal integrated Zintl ions has been isolated. In these types of clusters, instead of having transition metal as part of cluster skeleton, they are encapsulated in the cluster center. The transition metal in the center is believed to have stabilizing effect since the strength of the surface bonds may not enough to support clusters with large number of atoms. These types of clusters are called as “endohedrally functionalized or filled” clusters.⁵⁴ In literature, their chemical formulas are generally represented by first writing the interstitial atom then placing “@” sign and finally writing the cluster formula. For instance, lead cluster with interstitial Pt is represented with $[Pt@Pb_{12}]^{2-}$

.¹⁷

The first freestanding ligand-free icosahedral cluster, $[\text{Pt}@\text{Pb}_{12}]^{2-}$, is a good example to this stabilization as $[\text{Pb}_{12}]^{2-}$ could not be isolated yet.¹⁷(Figure 1.7.) Subsequent isolation of Pd and Ni centered $[\text{Pb}_{12}]^{2-}$ and the structural deformations due to differences in the size of the central atom demonstrated the effect of transition metal size on the stability of the cluster.¹⁸

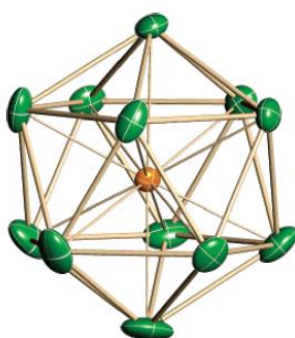


Figure 1.7. Ortep drawing of $[\text{Pt}@\text{Pb}_{12}]^{2-}$ ion.¹⁷

Encapsulation of transition metals in Zintl ion clusters with various geometries has also been demonstrated. For instance, $[\text{Cu}@\text{Pb}_9]^{3-}$ and $[\text{Ni}@\text{Pb}_{10}]^{2-}$ clusters exhibit monocapped square-antiprism and bicapped square-antiprism, respectively.^{19,80} On the other hand, $[\text{Ni}_2@\text{Sn}_{17}]^{4-}$ and $[\text{Pt}_2@\text{Sn}_{17}]^{4-}$ demonstrates interesting dumbbell structures.^{16,81}(Figure 1.8.) Characterization of some of these clusters with spectroscopic techniques such as NMR reveals their very unique properties. For instance, NMR studies on $[\text{Ni}@\text{Pb}_{10}]^{2-}$ and $[\text{Ni}_2@\text{Sn}_{17}]^{4-}$ anions shows interesting intermolecular exchange process.^{16,80} Such studies might provide valuable information about possible exchange between surface and bulk atom on

nanoparticles. They also help to understand properties of these particles such as their lower melting points relative to the bulk materials.⁸²

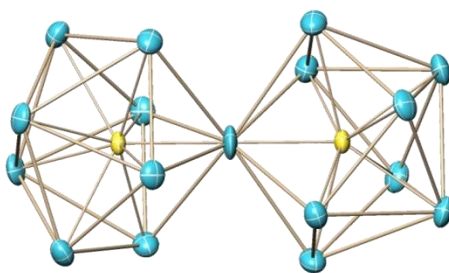


Figure 1.8. Ortep drawing of $[\text{Ni}_2@\text{Sn}_{17}]^{4+}$ ion.¹⁶

$[\text{Co}@\text{Ge}_{10}]^{3-}$ exhibits D_{5h} geometry of pentagonal prism which is not present in the traditional deltahedral geometries of transition metal containing Group 14 Zintl clusters.²⁰ Another example to these type of clusters is $[\text{Ru}@\text{Ge}_{12}]^{3-}$ having D_{2d} polyhedral geometry which is significantly different from other deltahedral 12-vertex clusters such as $[\text{M}@\text{Pb}_{12}]^{2-}$ ($\text{M} = \text{Ni}, \text{Pd}, \text{Pt}$).⁸³(Figure 1.9.)

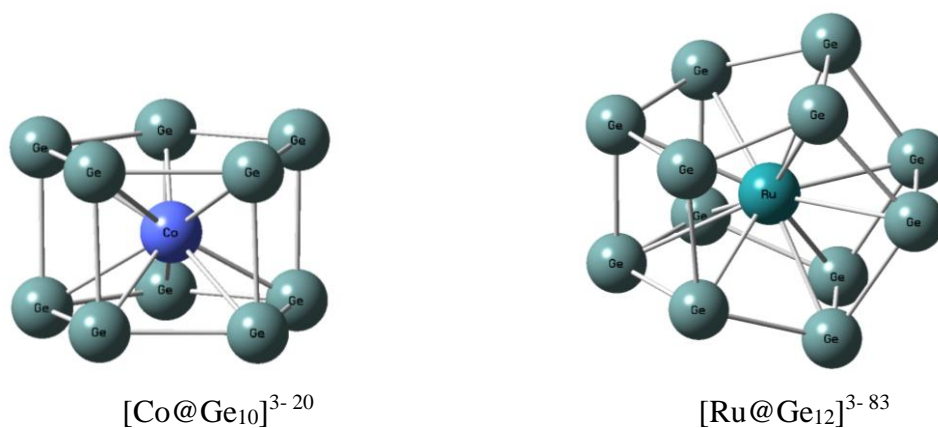


Figure 1.9. Examples to ligand-free transition metal integrated Germanium clusters.

Varieties of “endohedrally functionalized” Zintl ion clusters have been isolated up to date with different transition metal and main group element choices and also with more complicated structures. Some unique examples such as $[\text{Sn}@Cu_{12}@Sn_{20}]^{12-}$ and $[\text{As}@Ni_{12}@As_{20}]^{2-}$ show “onion skin” type arrangement of clusters with again individual atom placed in the center.^{44,84}(Figure 1.10) The existence of these examples supports the possibility of synthesizing increasingly large clusters which might have sizes in nanoscale.

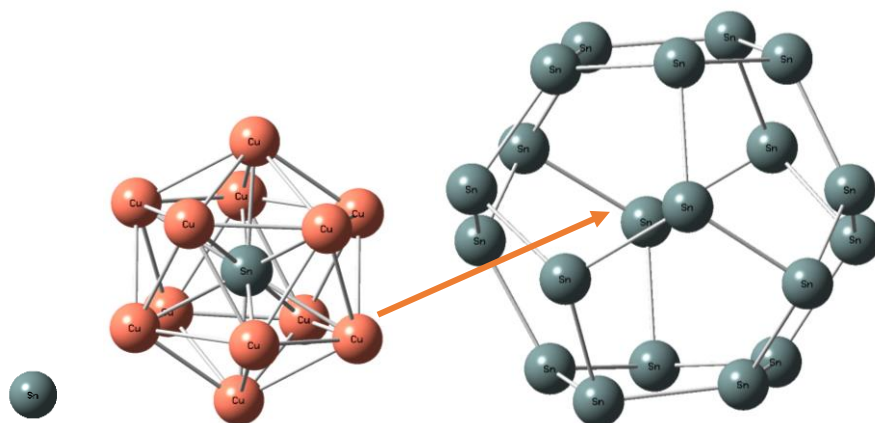


Figure 1.10. $[\text{Sn}@\text{Cu}_{12}@\text{Sn}_{20}]^{12-44}$

The extensive number of Zintl ion clusters each with unique structure and properties possesses the great potential to be used as “building blocks” in the formation of new, advanced materials. This potential has started the new research area where the Zintl ions can be used as “artificial atoms” or “super atoms” in the fabrication of “cluster assembled materials”.² These materials allow the control over properties by modifying the properties of building blocks. Zintl ions with their unique architectures and interesting properties take over this role in the hierarchical assembly of clusters. Therefore, it is very important to investigate these properties such as optical, electronic and magnetic to have the control on the formation of new materials.

The characterization of Zintl ion clusters have been generally performed with single crystal X-ray studies to identify their structures, mass spectroscopy to verify the structural data or to identify clusters formed in the gas phase, NMR spectroscopy to complement the structural analysis or to investigate dynamic properties in solution. A few of the isolated Zintl ion clusters have been studied with photoelectron spectroscopy to investigate their electronic properties.^{85,86} Also, only one FTIR study on Zintl ion cluster ($[\text{Ni}_2\text{Ge}_9(\text{CO})]^{2-}$) have been reported to verify the existence of

CO ligand.²¹ However, to our knowledge there is no extensive study on investigating these types of clusters' vibrational and optical properties which are very important in their potential future applications.

1.3. Computational Studies

Some properties of molecules can be calculated using specific computer programs with certain types of theoretical models. In each theoretical model, different sets of approximations together with an algorithm of calculation are used on atomic orbitals to calculate molecular orbitals and energy. Depending on the size of the system and approximation level, there are four main methods of theoretical models; semi-empirical, ab initio, density functional and molecular mechanics.⁸⁷ In our calculations, Density Functional Theory (DFT) has been used due to its good compatibility with transition metal complexes.⁸⁸

1.3.1. Density Functional Theory

DFT is one of the methods of theoretical chemistry calculating the ground state properties of metals, semi-conductors, insulators and also metal complexes. Different from ab initio methods (i.e. Hartree-Fock (HF) model) in which wave function is used to compute energy, DFT uses electron density instead. The electron density has always maxima at the positions of the nuclei; in other words, it is a function of nuclear positions. Therefore, molecular structures can be obtained from the electron density. Since the electron correlation is already included, there is no need for the correction of electron repulsion as in the case of HF-based calculations. This makes DFT calculations less time consuming than HF.^{87,89} Carbonyl containing transition metal complexes tend to give better results with hybrid models of DFT than HF. For instance, in the calculation of the distance between metal and carbon in a complex

revealed significant errors with HF method.^{90,91} B3LYP, Becke's 3-Parameter hybrid functional using nonlocal correlations due to Lee-Yang-Parr, called to be a hybrid model and known as the most popular DFT model.⁸⁹

Some of the reported examples of DFT calculations performed with clusters are summarized. For instance, in order to define the minimum energy structure of bismuth-doped tin clusters, density functional theory with generic algorithm method was used by Heiles et al. to compute dielectric properties of their low energy structures. Dielectric and structural properties are included in the simulations of beam profile to be compared with the experimental data which provides the type of pattern these bimetallic clusters follow while growing.⁹² In a study conducted by Eichhorn et al., the electronic and geometric structure of gas phase endohedral clusters of Pt/Pb anions are determined by DFT calculations along with the photoelectron spectroscopy. DFT calculations revealed that Pt@Pb₁₀¹⁻ and Pt@Pb₁₂^{2-/1-} clusters does not change their geometry of D_{4d} significantly in the gas phase.⁸⁶ Moreover, the most stable structures and different atom positions of [Sn_{9-m}-_nGe_mBi_n]⁽⁴⁻ⁿ⁾⁻ (n = 1-4 and m = 0-(9-n)) series are investigated by DFT calculations, since their structural data for ESI spectrometry is not sufficient enough. According to the results, the cluster geometry is strongly dependent to the stoichiometry with different charges.⁹³ Another DFT study conducted by King et al. showed that iron-centered germanium clusters (Fe@Ge₁₀^z, z = -5 to 3) tend to exhibit pentagonal prism instead of a deltahedral structure at the lowest energy conformation which is consistent with the experimental observation.⁹⁴ Schoss et al. investigated the possible structures of tin cluster anions, Sn_n⁻ (n = 16-29), by using DFT along with trapped ion electron diffraction and collision induced dissociation.⁹⁵

The shapes of atomic orbitals are described by certain sets of functions, called as basis sets. Atomic orbitals are linearly combined with the molecular orbitals calculated by a specific theoretical model. In each basis set, the level of approximation differs. A larger basis set may exhibit more accurate results but it is

also more time consuming and the calculation may not be completed due to complexity. Therefore, it is important to choose a basis set based on the properties and size of the system.

If the system has negative charge, excited states or lone pairs, it is better to prefer a basis set having diffuse functions, in which electrons can travel away from the nucleus and orbitals can diffuse. Some basis sets already have self-diffuse functions, but for some, an additional sign might be required such as 6-31g basis set become diffuse as '6-31g+'. In order to describe the system with a better approximation, polarized functions are needed. The atomic orbitals are distorted depending on the conditions of surroundings. Similar to diffuse ones, the polarization function can be either inside the basis set or added with a sign like '*', such as 3-21g*.^{96,97}

Based on the publications conducted on transition metal complexes containing germanium in recent years, for the calculations, medium-sized Lanl2dz and CEP-121g basis sets are chosen.^{91,98-100} Lanl2dz (Lanl = Los Alamos National Laboratory) is a double-zeta type basis set using effective core potentials (ECP) of Hay and Wadt. It can be applied to H, Li-La, Hf-Bi. CEP-121g (CEP = Consistent Effective Potential), on the other hand, is a triple split valence type basis set using ECPs of Stevens, Basch and coworkers. It can be used from H to Rn.^{91,97} Both basis sets use only valence electrons for calculation which is convenient for systems having large amount of electrons.

1.3.2. Types of Calculations Carried Out

Depending on the needs of the research, there are many types of calculations available in Gaussian 09. Some examples include geometry optimization, single point energy, frequency, population analysis, UV-Vis and electronic transitions, potential energy surface, solvation effect, etc. All calculations have common criteria

of converging at the minimum energy. Route for a reliable calculation is shown in Figure 1.11.⁹⁶

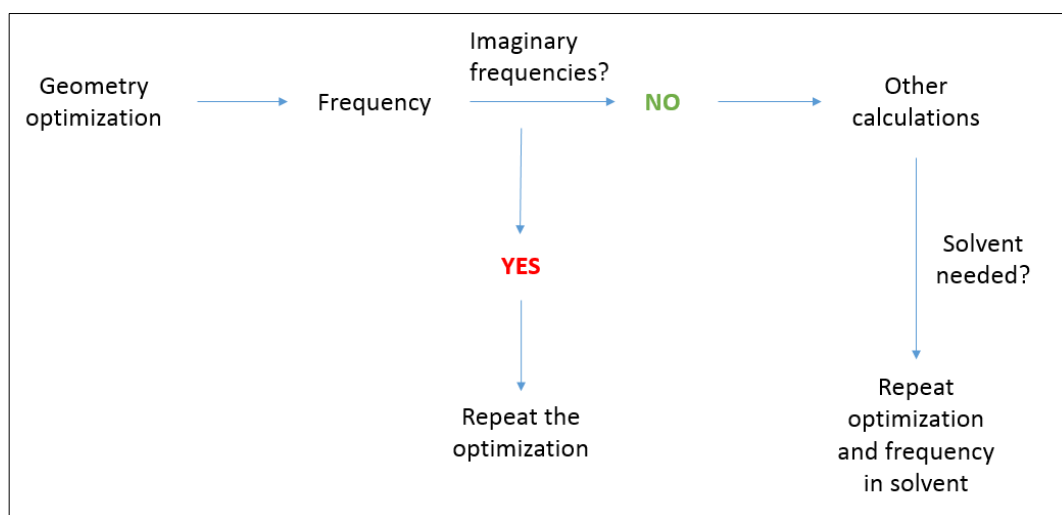


Figure 1.11. Suggested sequence of calculations for any molecule.

1.3.2.1. Geometry Optimization

The aim is to find the minimum energy configuration of the molecule by computing the wave function and the energy at the given geometry and processing until lower energy is found.⁹⁶ There are certain threshold values for convergence of RMS and Maximum Force/Displacement depending on the type of basis set which can be seen in the output file. Once all four criteria meet the threshold values, then the optimization finishes. The keyword to be included in the input file is 'Opt'.

From the output of the calculation these information can be obtained:

- Optimized coordinates of the molecule
- Atomic distances and angles
- HOMO/LUMO eigenvalues in Hartrees
- Mulliken atomic charges
- Dipole moments ¹⁰¹

1.3.2.2. Frequency

The vibrations of the molecule are calculated with this type of calculation. The resultant optimization coordinates is used in the input file with a keyword of 'Freq'. It is suggested to use the same theoretical model and basis set for both optimization and frequency calculations.

In the case of imaginary frequencies, which are negative values, are found in the output file, the molecule is instable and tends to be in transition state. Therefore, the optimization process should be repeated.

Raman intensities can also be calculated by adding the keyword 'Raman' to route line of input file.

From the output, this information can be obtained in addition to the ones in optimization calculation:

- Single point energy
- Harmonic frequencies
- Reduced masses
- Force constants
- IR intensities
- Raman intensities (if needed) ^{96,102}

1.3.2.3. UV-Vis and Electronic Transitions

As the difference between the excited and the ground state of a molecule matches the energy of a photon interacting with the molecule, the electron excitation takes place from an occupied level to an unoccupied level. According to Franck-Condon principle, electrons can move faster than the nuclei, so this absorption of energy does not influence the configuration of the nuclei much. That is why vertical excitation energies build the spectrum for absorption of the molecules.

There are three different methods; ZINDO, CIS and TD which are semi-empirical, HF and DFT based calculations, respectively. Time-Dependent (TD) calculation operates under the principles of DFT in which the wave functions of molecular orbitals oscillating between the ground state and upper levels are obtained.^{103,104} Number of transition states interested can be determined and added to the input line after the keyword of 'TD', i.e. TD=(NStates=100).

Following information can be obtained from this calculation:

- Transitions from ground state to excited state
- Energies of excitation and strengths of oscillation
- Eigenvalues of orbitals selected
- Population of orbitals⁹⁶

1.3.2.4. Solvation Effect

Since Gaussian computes in isolated environment, it might be logical to use the solvation effect to resemble to the experimental conditions. By adding 'SCRF' keyword along with the name of the solvent as 'SCRF=(solvent=n,n-dimethylformamide)', a solvent cavity is formed surrounding the molecule.^{96,105}

After completing the solvent-free optimization, the resulting coordinates should be used in the solvent-added calculation to optimize the structure. Then, by using the solvent-added optimization coordinates, other types of calculations in a solvent can be made.

CHAPTER 2

EXPERIMENTAL & COMPUTATIONAL

2.1. Experimental Part

All reactions and sample preparations for analysis were carried out under an inert atmosphere, in a glove box due to extreme air sensitivity of most of the compounds used or synthesized in this study. Solvent distillation was done using a dual-manifold Schlenk line equipped with argon as an inert gas. Air sensitive reagents were stored and used inside the M-Braun UNI-Lab glove box in which both oxygen and moisture levels are kept below the concentration of 0.1 ppm.

2.2. Materials

2,2,2-crypt (4,7,13,16,21,24-hexaoxa-1,10-diazabicyclo[8,8,8]-hexacosane; Sigma-Aldrich, 99%) and $\text{Ni}(\text{CO})_2(\text{PPh}_3)_2$ (bis(triphenylphosphine)dicarbonylnickel; Sigma-Aldrich, 99%) were taken inside the glove box as received and used in the synthesis of both clusters. Purification of solvents was done after passing each through molecular sieves (3Å). Ethylenediamine (Sigma-Aldrich, >99.5% GC) and DMF (dimethylformamide, Sigma-Aldrich, 99.0% GC), were both distilled over CaH_2 (Sigma-Aldrich, 99.99%) and Toluene (Sigma-Aldrich, >99.5% GC) were distilled over sodium/benzophenone mixture for several hours. After the completion of distillation procedures, all solvents were carefully frozen under argon gas and vacuum to prevent any source of moisture and oxygen, and then they were taken inside the glove box to be used in the experiments.

K₄Ge₉ precursor was synthesized from a stoichiometric mixture of the elements (K: 98.0%, Sigma-Aldrich; Ge: 99.999%, Sigma-Aldrich) according to previously reported synthetic procedures.

Paraffin oil (Sigma-Aldrich) was taken inside the glove box after several treatments of vacuum and nitrogen gas in one of the ports of the glove box and used in the FTIR measurements.

2.3. Synthesis of K₄Ge₉

Synthesis of K₄Ge₉ was performed with a method described in literature.¹⁵ Briefly, potassium chunks (0.21g, 5.37 mmol) and germanium granules (0.88g, 12 mmol) were weighed into a quartz tube inside the glove box and sealed under static vacuum. Resulting tube was placed in homemade stainless-steel jacket and heated to 650°C for 18 hours in a furnace under vacuum. The balanced equation for this reaction is shown in equation 2.1.



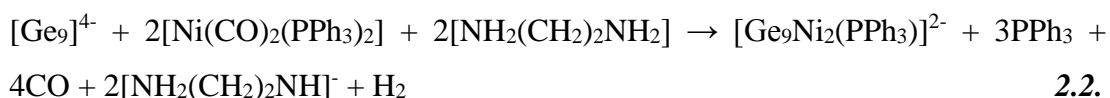
After taking this apparatus into the glove box, the quartz tube was broken and the product was taken inside a mortar. It was then crushed into fine powder via pestle.

2.4. Synthesis of [Ni₂Ge₉(PPh₃)²⁻

[Ni₂Ge₉(PPh₃)²⁻ cluster anions were synthesized with a method previously reported by Esenturk et al.¹⁵ Briefly, K₄Ge₉ (54 mg, 0.007 mmol) and Ni(CO)₂(PPh₃)₂ (84 mg, 0.14 mmol) and 2,2,2-crypt (0.1 g, 0.27 mmol) were dissolved in 4 mL of en in a vial. The mixture was nearly boiled for 15 minutes at 120°C and then hot filtered to an empty vial. It was set aside to cool down by itself and crystal formation was

observed in the bottom of the vial after 2-3 days. EDX analysis on the crystals showed the presence of Ni and Ge atoms. Ge: Ni: K = 9.09: 2.08: 1.85.

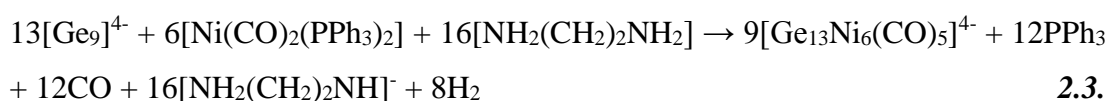
The proposed balanced equation for the synthesis of $[\text{Ni}_2\text{Ge}_9(\text{PPh}_3)]^{2-}$ in the presence of [2,2,2]-crypt is shown in equation 2.2.¹⁵



2.5. Synthesis of $[\text{Ni}_6\text{Ge}_{13}(\text{CO})_5]^{4-}$

Synthesis of $[\text{Ni}_6\text{Ge}_{13}(\text{CO})_5]^{4-}$ cluster anions was achieved by following same route used in the synthesis of $[\text{Ni}_2\text{Ge}_9(\text{PPh}_3)]^{2-}$ cluster crystals but at different reaction temperature.¹⁵ Similarly, K_4Ge_9 (54 mg, 0.007 mmol) and $\text{Ni}(\text{CO})_2(\text{PPh}_3)_2$ (84 mg, 0.14 mmol) and 2,2,2-crypt (0.1 g, 0.27 mmol) were dissolved in en in a vial. The mixture was stirred for 15 minutes at 45°C and then hot filtered to an empty vial. After self-cooling, crystals appeared after about a week. EDX analysis on the crystals showed the presence of Ni and Ge atoms. Ge: Ni: K= 13.78: 1.65: 1.47.

The proposed balanced equation for the synthesis of $[\text{Ni}_6\text{Ge}_{13}(\text{CO})_5]^{4-}$ in the presence of [2,2,2]-crypt is shown in equation 2.3.¹⁵



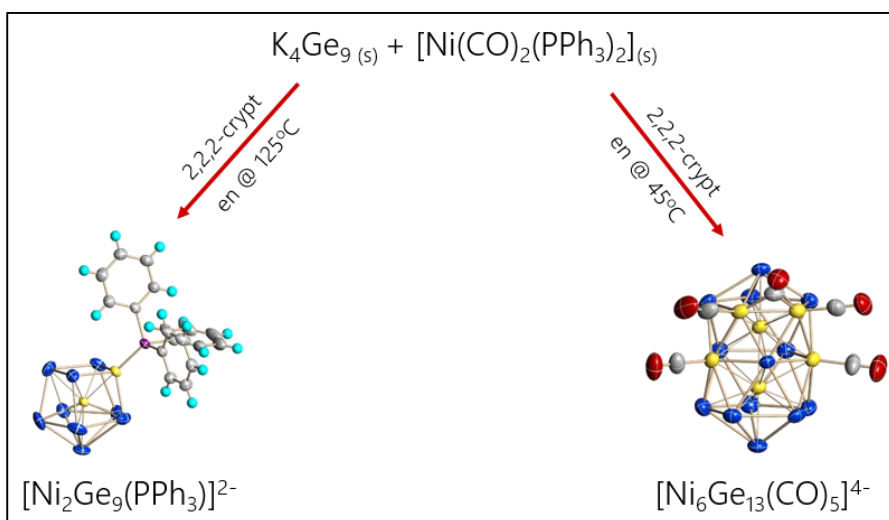


Figure 2.1. Schematic representation of synthetic pathway of Ni-Ge clusters (en: ethylenediamine)¹⁵

2.6. Sample Preparation for Spectroscopic Measurements

The crystal isolation procedure is as follows for all measurements:

1. Collecting crystals from the solution
2. Washing them with toluene
3. Drying them under vacuum
4. Storing them in a closed-cap vial inside the glove box

It should be noted that all procedures were done inside the glove box until the measurement of the sample in the related instruments outside. Moreover, due to presence of the high static field inside the glove box, the crystals cannot be weighed. Thus, it is not possible to determine the exact concentration of the solutions or mixtures.

2.6.1. Fourier Transform Infrared Spectroscopy

A liquid sample holder with rectangle TPX (polymethylpentene) and PS (polystyrene) windows, and a solid sample holder with a KBr window along with a 120 micron-tick spacer were used in FTIR measurements.(Figure 2.2.)

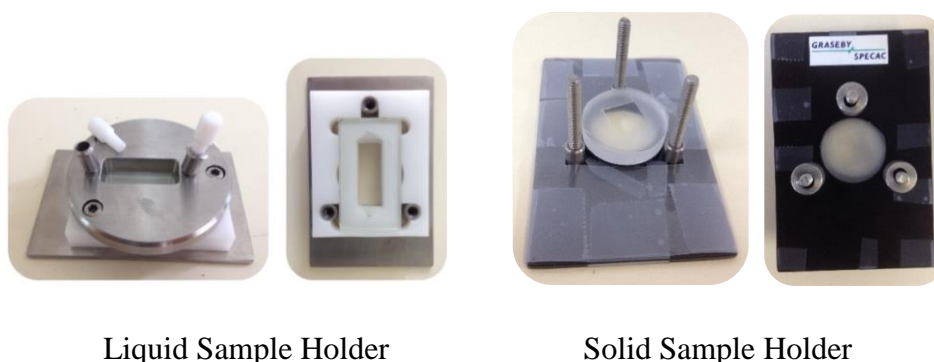


Figure 2.2. FTIR sample holders

Two types of measurements were applied on both clusters and precursors (i.e. $\text{Ni}(\text{CO})_2(\text{PPh}_3)_2$, $\text{Pt}(\text{PPh}_3)_4$ and K_4Ge_9); liquid-phase measurement in DMF and solid-phase measurement in paraffin oil. In the liquid-phase measurements, the crystals collected from the solutions were dissolved in certain amount of DMF and injected through the holes of the liquid sample holder having a 100 micron-tick spacer in between two TPX windows by not leaving any air bubbles. After sealing the Teflon lids of the holes carefully, the sample was taken outside the glove box and measurement was performed. DMF was used as blank measurements for each sample.

In the solid-phase measurements, paraffin oil and crystals (i.e. one or two pieces) were put inside an agate mortar and crushed all together with the pestle until a smooth mixture was obtained. Then, the mixture was buttered onto the surface of one window having already the spacer on. The second window was carefully placed on top of sample without leaving any air bubbles in between. After securing windows on holder, the sample was taken to the instrument for measurements. Paraffin oil was used as a blank, and blank measurement was done before every sample measurement.

After several trials to find the optimum settings for measurements in paraffin oil, the device was set to some parameters including gain as 2.0, optical velocity as 0.4747, and aperture as 100.

2.6.2. Fluorescence Spectroscopy

Sample solution was prepared by dissolving cluster crystals. As it is noted before, the exact concentration of the solution could not be determined due to challenges during weighing process of crystals, resulting from the high static field inside the glove box. The sample solution then placed inside the quartz cuvette which was then sealed carefully with parafilm to prevent any contact with air. As blank, only DMF was measured to eliminate any emission bands which might be formed due to the solvent.

2.6.3. UV-Vis Spectroscopy

The samples were prepared in the same way as in the Fluorescence spectroscopy studies. However, more dilute solution was prepared to keep absorbance under the value of 1.0. Similarly, DMF was measured as blank to eliminate the absorbance due to the solvent itself.

2.7. Computational Part

All calculations were submitted to Gaussian 09 via TR-Grid servers of ULAKBIM by using the SSH client software MobaXterm.

After creating appropriate input and slurm files, the calculation can start by using the command of 'sbatch'. It is very important to have both input and slurm files in the same directory. Also, the location where the calculations are done should be the same as those files. Otherwise, the job submission cannot be achieved. It should be noted that Linux is case sensitive, so it might be practical choosing the file names in lower case letters. The output and error files are created in the locations given in the slurm file.

An example to job submission is shown in Table 2.1.

Table 2.1. Examples to successful and unsuccessful job submissions

	Successful Job Submission	Unsuccessful Job Submission
Input File	ni2ge9_b31yp_lan12dz_opt.com	ni2ge9_b31yp_lan12dz_opt.com
Slurm File	ni2ge9-lan12dz-opt.slurm	ni2ge9-lan12dz-opt.slurm
Location of Both Files	truba_scratch/enalbantesenturk/ ni2ge9/lan12dz/opt/	truba_scratch/enalbantesenturk/ ni2ge9/lan12dz/opt/
Current Location	truba_scratch/enalbantesenturk/ ni2ge9/lan12dz/opt/	truba_scratch/enalbantesenturk/ ni2ge9/
Command Line	sbatch ni2ge9-lan12dz-opt.slurm	sbatch ni2ge9-lan12dz-opt.slurm

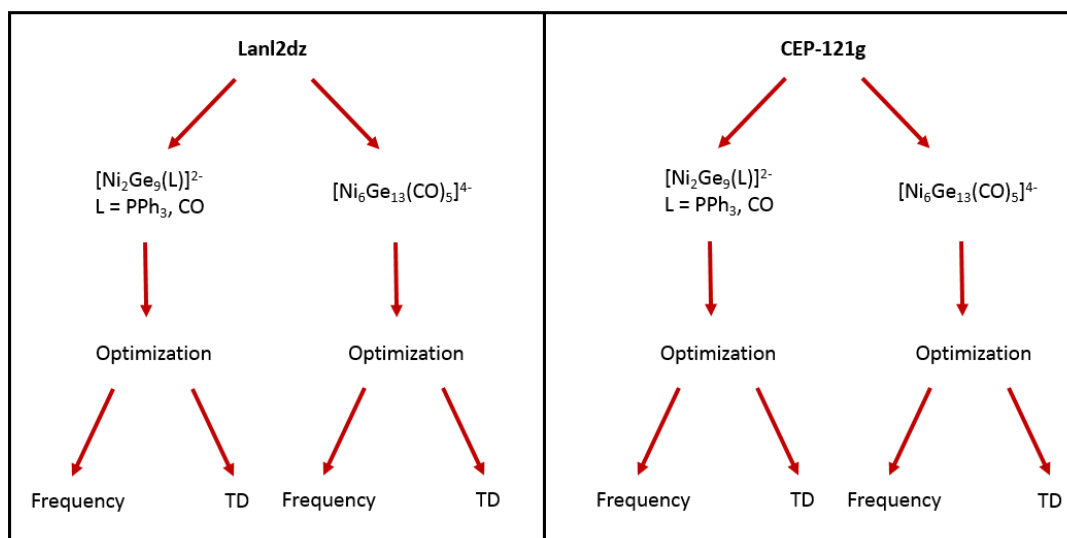


Figure 2.3. Calculation flow for both basis sets

The pathway shown in Figure 2.3 was performed for the calculations with or without the use of solvation effect.

2.7.1. Geometry Optimization

The coordinates of both Ni-Ge clusters were accessed from the Single-Crystal XRD data of their publication.¹⁵ For calculations, coordinates of a single cluster should be present in the input file. However, the crystal data not only included multiple clusters of the same kind but also the crypt molecules surrounding them in a unit cell. Therefore, the crypt molecules and additional cluster molecules were deleted in GaussView 5.0. Then, the coordinates of a single cluster molecule were extracted to an input file.

The route line in the input file is as follows:

```
#p opt b3lyp/lanl2dz
```

2.7.2. Frequency

The outputs of the successful optimization calculation were opened in GaussView 5.0 to extract the optimized coordinates for other calculations. These optimized coordinates of the corresponding basis set were inserted to the input file of the frequency calculation. It is crucial to continue with the same basis set when using its optimized coordinates, because each basis set has different levels of approximation.

The route line in the input file is as follows (for Lanl2dz optimized coordinates):

```
#p freq b3lyp/lanl2dz
```

The output of the frequency calculation was opened in GaussView 5.0 and ChemCraft 1.7 for visualization of the vibrational spectrum and can be redrawn in programs such as Origin or Excel.

2.7.3. UV-Vis and Electronic Transitions

Similar to frequency calculations, the coordinates of the successful optimization were inserted to the input file. Normally, the default settings for number of transitions in TD calculation are set as 3. Since both clusters have huge amount of electrons, the number of transitions were chosen from 100 to 500 to see the trend in the graphs.

The input file is as follows for a 200 transition state calculation:

```
#p td=(nstates=200) b3lyp/lanl2dz
```

As frequency outputs, the TD output was opened in the same programs to visualize the absorption spectrum.

2.7.4. Solvation Effect

The effect of the solvent can be added to the input line of the desired molecule having optimized coordinates. Since DMF was used as a solvent in UV-Vis measurements, its effect has been calculated. Before calculating TD electronic transitions in a solvent, the optimization should be redone by adding the following line to the input route.

```
#p opt b3lyp/lanl2dz scrf=(solvent=n,n-dimethylformamide)
```

Then, from the output of these solvent added optimizations, the new coordinates were extracted by GaussView 5.0 and inserted into the corresponding frequency or TD inputs. However, the solvent line should be kept in the route.

```
#p td=(nstates=200) b3lyp/lanl2dz scrf=(solvent=n,n-dimethylformamide)
```


CHAPTER 3

RESULTS & DISCUSSION

3.1. Synthesis and Structures of $[\text{Ni}_2\text{Ge}_9(\text{PPh}_3)]^{2-}$ and $[\text{Ni}_6\text{Ge}_{13}(\text{CO})_5]^{4-}$ Zintl Ion Clusters

$[\text{Ni}_2\text{Ge}_9(\text{PPh}_3)]^{2-}$ and $[\text{Ni}_6\text{Ge}_{13}(\text{CO})_5]^{4-}$ Zintl ion clusters are synthesized from the reaction of K_4Ge_9 , $[\text{Ni}(\text{CO})_2(\text{PPh}_3)_2]$ and 2,2,2-crypt in ethylenediamine (en) at different reaction temperatures.¹⁵ $[\text{K}(2,2,2\text{-crypt})]^+$ salt of $[\text{Ni}_6\text{Ge}_{13}(\text{CO})_5]^{4-}$ is obtained when the reaction is performed at temperature about 45°C. On the other hand, the one of $[\text{Ni}_2\text{Ge}_9(\text{PPh}_3)]^{2-}$ is formed at elevated temperatures, 120°C. Both salts are air and moisture sensitive in solution and in solid state. Their solubility is high in DMF and CH_3CN , forming dark brown solutions.

Structural analyses of the clusters that reveal their interesting bonding natures have been previously reported in literature.¹⁵ Briefly, $[\text{Ni}_2\text{Ge}_9(\text{PPh}_3)]^{2-}$ anion is formed by nine surface Ge atoms, one Ni encapsulated in the center of the cluster and one $[\text{Ni}(\text{PPh}_3)]$ fragment capping the cluster.(Figure 3.1.a) The anion has virtual C_{3v} point symmetry and exhibiting 10-vertex 20 electron deltahedron. Therefore, it can be defined as *hypo-closo* system with open *nido*-like structure according to Wades' rules. The total number of electron of the anion is 484.

The structure of the $[\text{Ni}_6\text{Ge}_{13}(\text{CO})_5]^{4-}$ anion can be defined as 17-vertex deltahedral cluster formed by 13 Ge atoms and 4 Ni atoms.(Figure 3.1.b) The cluster also has two interstitial Ni atoms located in the center. Each Ni atoms on the surface has one CO ligand and two of them have additional bridging CO ligand. The structure of the anion reveals C_s point symmetry with a symmetry plane passing through five Ge

atoms, two interstitial Ni atoms and a bridging CO ligand. This 17-vertex deltahedron has 658 total electron (126 valence electrons) and 32 skeletal electrons. Therefore, the cluster can be defined as *hypo-closo* according to Wades Rules.

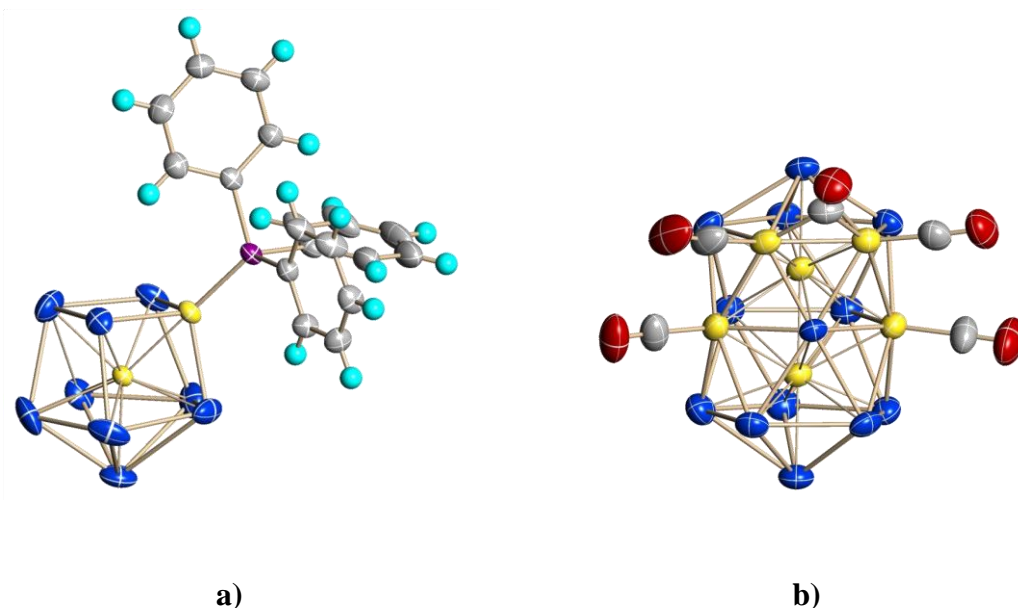


Figure 3.1. Ortep drawings of **a)** $[\text{Ni}_2\text{Ge}_9(\text{PPh}_3)]^{2-}$ **b)** $[\text{Ni}_6\text{Ge}_{13}(\text{CO})_5]^{4-}$ ¹⁵

Electrospray (ESI) mass spectrometry analyses for both cluster anions were reported previously to verify the structure obtained from single crystal analysis. These studies were done in negative ion mode from the DMF solutions of cluster crystals.¹⁵ They revealed the mass envelopes arising from the multiple isotopes of Ni and Ge. For example, the spectrum of DMF solutions of $[\text{K}(2,2,2\text{-crypt})]_4[\text{Ni}_6\text{Ge}_{13}(\text{CO})_5]$ crystals shows signals for $[\text{K}(2,2,2\text{-crypt})\text{Ni}_6\text{Ge}_{13}(\text{CO})_5]^{1-}$ ($m/z = 1850$) as a parent ion and decomposition products observed in gas phase (i.e. $[\text{Ni}_6\text{Ge}_{13}]^{1-}$ ($m/z = 1296$), $\text{K}[\text{Ge}_9\text{Ni}_2(\text{CO})]^{1-}$ ($m/z = 838$)). The spectrum of $[\text{Ni}_2\text{Ge}_9(\text{PPh}_3)]^{2-}$ cluster demonstrate

the parent ion ($[\text{K}(2,2,2\text{-crypt})\text{Ni}_2\text{Ge}_9(\text{PPh}_3)]^{1-}$ ($m/z = 1447$) as well as its fragments and/or gas phase products such as $\text{K}[\text{Ni}_2\text{Ge}_9(\text{CO})]^{1-}$ ($m/z = 838$), $\text{K}[\text{Ni}_2\text{Ge}_9]^{1-}$ ($m/z = 810$).

Here, in this study, too, ESI mass spectrometry studies in similar conditions are performed with the exception of solvent type. In this study, instead of using DMF, CH_3CN and DMF mixture (with 1% of DMF) is used because of the instrumental restrictions. Even though the crystals have very good solubility in CH_3CN , the solution starts to decompose in very short amount of time. This might be due to high coordinating ability of the CH_3CN resulting a change and/or decomposition of the cluster investigated. Therefore, ESI mass spectrometry studies are hampered by these restrictions. The example of ESI mass spectrum is given in appendix section, in Figure A.1. It is important to note that the analysis of $[\text{Ni}_2\text{Ge}_9(\text{PPh}_3)]^{2-}$ anion revealed the signals of K-coordinated molecular ion of $[\text{Ni}_2\text{Ge}_9(\text{CO})]^{1-}$ ($m/z = 838.1$) as it is observed in previously reported study.¹⁵ It is first considered as a gas phase product produced in fragmentation of main cluster. However, isolation of the $[\text{Ni}_2\text{Ge}_9(\text{CO})]^{2-}$ cluster anion (Figure 3.2) by Sevov and co-workers²¹ strengthen the possibility of obtaining this cluster ions' crystals along with the ones of $[\text{Ni}_2\text{Ge}_9(\text{PPh}_3)]^{2-}$. Also, as it is being discussed in following sections, observation of CO signals in the FTIR measurements of $[\text{Ni}_2\text{Ge}_9(\text{PPh}_3)]^{2-}$ cluster make this assumption more valid. Therefore, $[\text{Ni}_2\text{Ge}_9(\text{CO})]^{2-}$ anion is included in the computational studies as well.

Computational studies have been carried out in order to help us better understand the observed spectroscopic properties of the synthesized clusters. Unfortunately, these types of clusters are fairly new and not much information is available in the literature. Here, previously reported crystal structures were used to obtain the initial geometries of the isolated $[\text{Ni}_6\text{Ge}_{13}(\text{CO})_5]^{4-}$ and $[\text{Ni}_2\text{Ge}_9(\text{PPh}_3)]^{2-}$ molecules. $[\text{Ni}_2\text{Ge}_9(\text{CO})]^{2-}$ anion is obtained by the replacement of PPh_3 with a CO group.

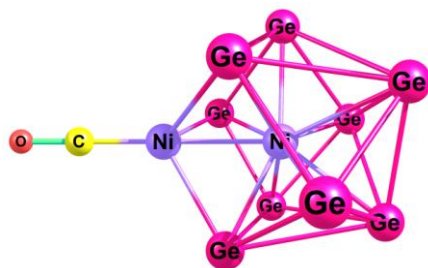


Figure 3.2. Visualized structure of $[\text{Ni}_2\text{Ge}_9(\text{CO})]^{2-}$ ²¹

Since these clusters have complex geometries with huge numbers of electrons, it very difficult to optimize with large basis sets having diffuse and polarized functions (i.e. 6-311+G(d)). Therefore, basis sets that treat core electrons as potentials and consider valance electrons only such as CEP-121g are more applicable to these molecules. After an extensive literature search we have observed that mainly Lanl2dz and CEP-121g is used for similar structures. We have also tried augmented versions of these basis sets to include diffuse functions since the clusters are charged species. However, the computational power of TR-Grid was not sufficient and we were unable to have a successful run. Therefore, all the presented results are obtained by these two basis sets. Results of spectroscopic studies are given and discussed by comparing them with the computational ones.

3.2. Geometry Optimization of $[\text{Ni}_2\text{Ge}_9(\text{PPh}_3)]^{2-}$ and $[\text{Ni}_6\text{Ge}_{13}(\text{CO})_5]^{4-}$ Zintl Ion Clusters with Lanl2dz and CEP-121g Basis Sets

Figure 3.3 shows the visualized structure of $[\text{Ni}_2\text{Ge}_9(\text{PPh}_3)]^{2-}$ where germaniums (pink) are from 10 to 18, nickels (purple) are 19 and 20, phosphorous (green) is 21, and carbons (yellow) bonded to phosphorous are 22, 24 and 35.

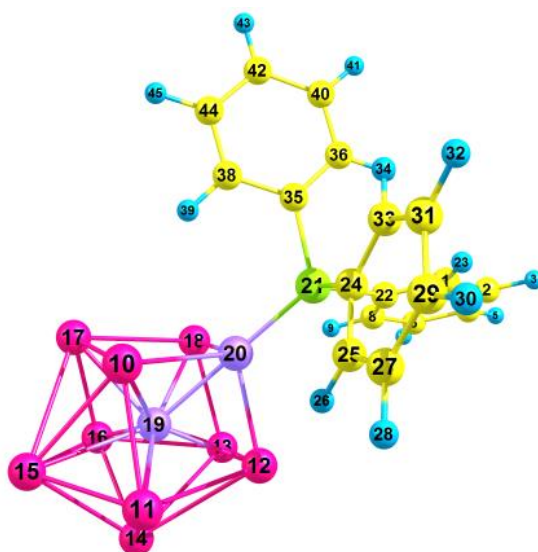


Figure 3.3. Visualized structure of $[\text{Ni}_2\text{Ge}_9(\text{PPh}_3)]^{2-}$

The cartesian coordinates extracted from single crystal data of this cluster before optimization are shown in Table A.1. The carbon and hydrogen atoms are not included in the table. The cartesian coordinates of the cluster after the optimization with Lan12dz and CEP-121g basis sets are shown in Table A.2. There are slight differences between the coordinates of the two basis sets, because they use different approximations and functions to optimize the structure. Thus, the minimum energy structure of the cluster is not exactly the same.

In order to decide which calculation is more similar to the original structure, the bond lengths and angles of the optimized structures are compared with the ones obtained from crystal data. The differences between the bond lengths of selected atoms, Ge-Ge and Ni-Ge bond averages are shown in Table 3.1.

Table 3.1. Comparison of bond lengths calculated with both basis sets: $[\text{Ni}_2\text{Ge}_9(\text{PPh}_3)]^{2-}$

	Bond Lengths (Å)				
	Crystal Structure	Lanl2dz Optimized	Difference	CEP-121g Optimized	Difference
<i>Average</i>	2.482	2.591	0.109	2.578	0.096
<i>Minimum</i>	1.840	1.903	0.029	1.920	0.031
<i>Maximum</i>	2.997	3.230	0.233	3.196	0.199
<i>Average R (Ni-Ge)</i>	2.395	2.486	0.091	2.478	0.083
<i>Average R (Ge-Ge)</i>	2.696	2.830	0.135	2.806	0.111

Overall, there are no unexpected deviations in the results of both calculations. The average bond lengths and differences are very close to each other. The average bond lengths are 2.482 Å, 2.591 Å and 2.578 Å, average Ni-Ge bond lengths are 2.395 Å, 2.486 Å and 2.478 Å, and Ge-Ge bond lengths are 2.696 Å, 2.830 Å and 2.806 Å for crystal structure, Lanl2dz and CEP-121g, respectively. The results suggest that the optimized structures are slightly expanded in space. This is expected since the crystal structure is formed by a salt of the cluster, thus have electrostatic interactions. However, the calculations are done for a single molecule. Comparison of the two basis sets show that the CEP-121g optimization is slightly closer to the original structure than Lanl2dz one, thus show less deviation.

The average bond angles are 96.5°, 96.6° and 96.6° for crystal structure, Lanl2dz and CEP-121g, respectively.(Table 3.2.) The angles are very close to each other

suggesting that the overall shape of the cluster has not changed significantly. When individual angles are compared, CEP-121g optimized structure has slightly lower differences with the crystal data compared to the ones of Lanl2dz optimized structure. The bond lengths obtained by both basis sets are in acceptable range and close to the originals with a maximum deviation of ca. 7 degrees.

Table 3.2. Comparison of bond angles calculated with both basis sets: $[\text{Ni}_2\text{Ge}_9(\text{PPh}_3)]^{2-}$

	Bond Angles ($^\circ$)				
	Crystal Structure	Lanl2dz Optimized	Difference	CEP-121g Optimized	Difference
<i>Average</i>	96.5	96.6	2.5	96.6	2.3
<i>Minimum</i>	59.4	58.7	0.0	58.8	0.0
<i>Maximum</i>	177.2	179.8	7.2	179.8	7.3

Figure 3.4 represents the visualized structure of $[\text{Ni}_6\text{Ge}_{13}(\text{CO})_5]^{4-}$ where germaniums are pink, nickels are purple, carbons are yellow, and oxygens are red. The cartesian coordinates extracted from a single crystal of this cluster and after the optimization are shown in Table A.3 and Table A.4, respectively.

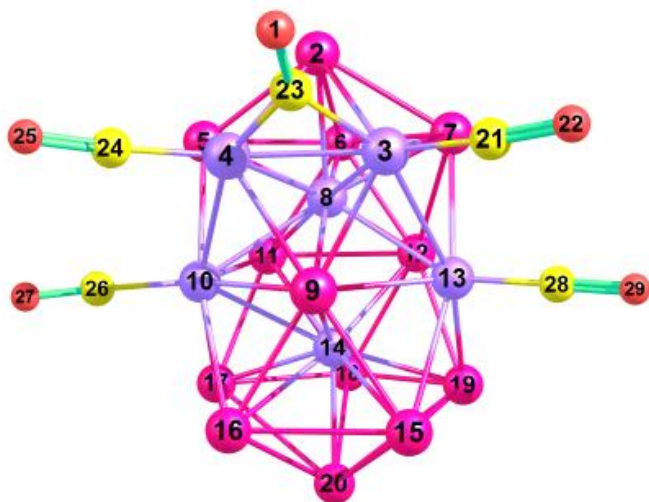


Figure 3.4. Visualized structure of $[\text{Ni}_6\text{Ge}_{13}(\text{CO})_5]^{4-}$

The differences in the bond lengths of selected atoms, Ge-Ge and Ni-Ge bond averages compared to the experimental ones are given in Table 3.3. Overall, all values are consistent with the crystal structure. The average bond lengths and differences are very close to each other. The average bond lengths are 2.322 Å, 2.381 Å and 2.381 Å, average Ni-Ni bond lengths are 2.591 Å, 2.698 Å and 2.709 Å, and Ni-Ge bond lengths are 2.537 Å, 2.594 Å and 2.590 Å, Ge-Ge bond lengths are 2.755 Å, 2.895 Å and 2.865 Å for crystal structure, Lan12dz and CEP-121g, respectively. According to the metal skeleton average bond length values, CEP-121g optimization again shows less deviation from the original structure.

Table 3.3. Comparison of bond lengths calculated with both basis sets: $[\text{Ni}_6\text{Ge}_{13}(\text{CO})_5]^+$

	Bond Lengths (Å)				
	Crystal Structure	Lanl2dz Optimized	Difference	CEP-121g Optimized	Difference
<i>Average</i>	2.322	2.381	0.061	2.381	0.062
<i>Minimum</i>	1.136	1.199	0.000	1.209	0.002
<i>Maximum</i>	2.668	2.777	0.197	2.780	0.174
<i>Average R (Ni-Ni)</i>	2.591	2.698	0.107	2.709	0.118
<i>Average R (Ni-Ge)</i>	2.537	2.594	0.060	2.590	0.056
<i>Average R (Ge-Ge)</i>	2.755	2.895	0.140	2.865	0.110

The average bond angles are 94.9°, 95.8° and 95.5° for crystal structure, Lanl2dz and CEP-121g, respectively.(Table 3.4.) Both calculations have the similar average bond angle values; however, CEP-121g calculation has a closer value to the crystal structure, having a difference of 1.8 degrees. As the bond lengths, all values are similar to the original with a maximum deviation of ca. 9 degrees.

Table 3.4. Comparison of bond angles calculated with both basis sets: $[\text{Ni}_6\text{Ge}_{13}(\text{CO})_5]^{4-}$

	Bond Angles (°)				
	Crystal Structure	Lanl2dz Optimized	Difference	CEP-121g Optimized	Difference
<i>Average</i>	94.9	95.8	2.5	95.5	1.8
<i>Minimum</i>	48.6	49.8	0.0	49.5	0.0
<i>Maximum</i>	177.5	177.0	8.7	177.8	9.2

3.3. Molecular Orbital (MO) Diagrams of $[\text{Ni}_2\text{Ge}_9(\text{PPh}_3)]^{2-}$ and $[\text{Ni}_6\text{Ge}_{13}(\text{CO})_5]^{4-}$ Zintl Ion Clusters

Molecular orbital diagrams are constructed from the DMF-based optimization results of $[\text{Ni}_2\text{Ge}_9(\text{PPh}_3)]^{2-}$ and $[\text{Ni}_6\text{Ge}_{13}(\text{CO})_5]^{4-}$ with both basis sets. (Figure 3.5 and Figure 3.6) The HOMO-LUMO band gaps of $[\text{Ni}_2\text{Ge}_9(\text{PPh}_3)]^{2-}$ are found as 0.1092 eV (11.3 μm , 880.8 cm^{-1}) and 0.1091 eV (11.4 μm , 879.9 cm^{-1}) for Lanl2dz and CEP-121g basis sets, respectively. Lanl2dz and CEP-121g use different numbers of core electrons in calculations; therefore, the occupied and unoccupied energy levels are not the same and not meaningful to compare. However, the differences in energy states such as HOMO-LUMO can be compared, and the calculated HOMO-LUMO band gaps are very close to each other. (Figure 3.5.) The range for the band gap of silicon-germanium alloys is between 0.67 eV and 0.11 eV at 300 K.¹⁰⁶ The band gap of this cluster falls within the same region, so it might be a semiconductor.

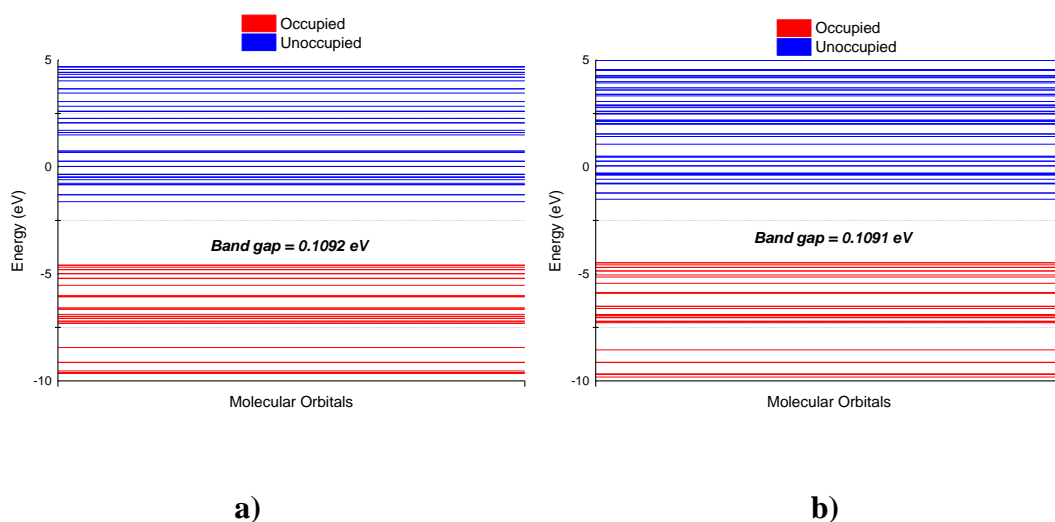


Figure 3.5. MO diagrams of $[\text{Ni}_2\text{Ge}_9(\text{PPh}_3)]^{2-}$ in DMF with a) Lanl2dz b) CEP-121g

The HOMO-LUMO band gaps of $[\text{Ni}_6\text{Ge}_{13}(\text{CO})_5]^{4-}$ are determined as 0.0574 eV (21.6 μm , 462.9 cm^{-1}) and 0.0564 eV (22.0 μm , 454.9 cm^{-1}) with Lanl2dz and CEP-121g basis sets, respectively. The much lower value compared to the other cluster might be due to higher number of electrons in $[\text{Ni}_6\text{Ge}_{13}(\text{CO})_5]^{4-}$. (Figure 3.6.)

Such low HOMO-LUMO band gaps and very broad absorption spectra of the clusters open up many application areas from optics to solar cells where they can be used as detectors, solar energy collectors, optical filters, etc.

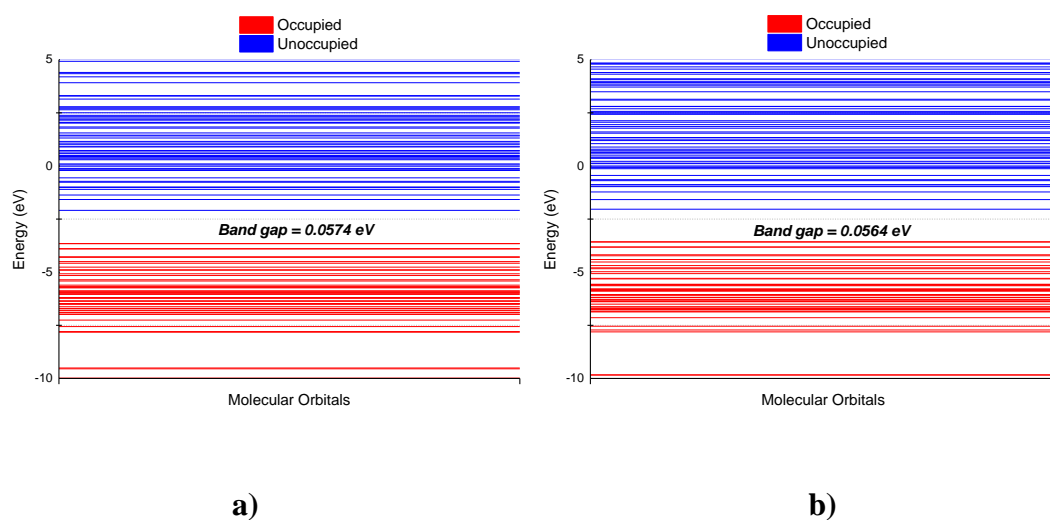


Figure 3.6. MO diagrams of $[\text{Ni}_6\text{Ge}_{13}(\text{CO})_5]^{4+}$ in DMF with a) Lan12dz b) CEP-121g

3.4. UV-Vis, FTIR and Fluorescence Spectrometry Analyses of $[\text{Ni}_2\text{Ge}_9(\text{PPh}_3)]^{2-}$ and $[\text{Ni}_6\text{Ge}_{13}(\text{CO})_5]^{4+}$ Zintl Ion Clusters

Vibrational and optical properties of $[\text{Ni}_2\text{Ge}_9(\text{PPh}_3)]^{2-}$ and $[\text{Ni}_6\text{Ge}_{13}(\text{CO})_5]^{4+}$ cluster anions are analyzed qualitatively with UV-Vis, FTIR and fluorescence spectrometry. Quantitative analysis hampered by difficulties faced during sample preparation with known concentrations. These difficulties arise mostly because of the high static field inside the glove box, where all the samples are prepared along with the small size of the crystals. These do not make it possible to weigh crystals correctly, thus to prepare sample solutions in unknown concentrations. Therefore, it is important to note that relative intensities of observed signals are not comparable since the sample concentrations in each measurement might be different, which led us to consider only peak positions in the discussion of experimental results.

The following two sections include discussion on UV-Vis and FTIR spectrometry analysis results of the cluster anions and their comparison with the computational ones. Finally, the results of fluorescence spectrometry results will be discussed.

3.4.1. UV-Vis Spectrometry Analyses

The absorption spectra obtained from DMF solutions of $[\text{Ni}_2\text{Ge}_9(\text{PPh}_3)]^{2-}$ and $[\text{Ni}_6\text{Ge}_{13}(\text{CO})_5]^{4-}$ anion crystals are shown in Figure 3.7. The spectra are fairly similar to each other with maximum intensity of the absorption band around 270 nm for both cluster with an exception of a shoulder appearing around 320 nm for $[\text{Ni}_6\text{Ge}_{13}(\text{CO})_5]^{4-}$. (Figure 3.7.) This observation is most likely explained by the more complex structure of $[\text{Ni}_6\text{Ge}_{13}(\text{CO})_5]^{4-}$ cluster ion with larger number of valance electrons compared to the those of $[\text{Ni}_2\text{Ge}_9(\text{PPh}_3)]^{2-}$. Since the absorption bands observed in UV-Vis spectrum corresponds to charge transfers in the molecule, the molecule with more electrons will more likely to produce broader bands in the spectrum.

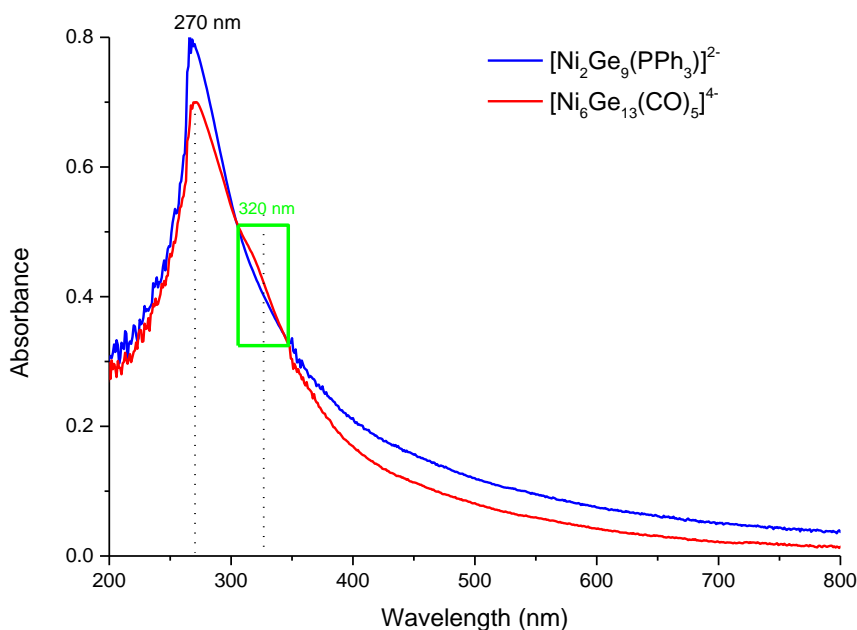


Figure 3.7. UV-Vis spectra of $[\text{Ni}_2\text{Ge}_9(\text{PPh}_3)]^{2-}$ and $[\text{Ni}_6\text{Ge}_{13}(\text{CO})_5]^{4-}$ cluster crystals in DMF

3.4.1.1. Results of Time-Dependent (TD) Electronic Transition Calculations for $[\text{Ni}_2\text{Ge}_9(\text{PPh}_3)]^{2-}$, $[\text{Ni}_2\text{Ge}_9(\text{CO})]^{2-}$ and $[\text{Ni}_6\text{Ge}_{13}(\text{CO})_5]^{4-}$

Electronic transition spectra drawn from the outputs of TD calculations with Lanl2dz and CEP-121g basis sets are shown in the following sections. Since the clusters not only have huge number of electrons (see Section 3.1) but also a lot of transitions, these calculations were very time consuming and required very large amount of memory. In order to simulate the experimental UV-Vis spectra, approximately 750 transitions is required, thus a memory of more than 1000Mw (2 GB) in cases was needed instead of 400Mw (800 MB), which was used for the optimization and frequency calculations. Unfortunately, 750 transitions were only achieved for $[\text{Ni}_2\text{Ge}_9(\text{PPh}_3)]^{2-}$ (Lanl2dz) and $[\text{Ni}_2\text{Ge}_9(\text{CO})]^{2-}$ (Lan2ldz, CEP-121g) calculations,

and TR-Grid environment was not enough for the large systems. For $[\text{Ni}_6\text{Ge}_{13}(\text{CO})_5]^{4-}$, a maximum of 500 transitions could be calculated with both basis sets since it has more electrons and more complicated structure than the other two clusters.(Table 3.5.)

Table 3.5. Calculated maximum transition states of $[\text{Ni}_2\text{Ge}_9(\text{PPh}_3)]^{2-}$, $[\text{Ni}_2\text{Ge}_9(\text{CO})]^{2-}$ and $[\text{Ni}_6\text{Ge}_{13}(\text{CO})_5]^{4-}$ with Lanl2dz and CEP-121g

Basis Set	Transitions	$[\text{Ni}_2\text{Ge}_9(\text{PPh}_3)]^{2-}$ (484 electrons)	$[\text{Ni}_2\text{Ge}_9(\text{CO})]^{2-}$ (360 electrons)	$[\text{Ni}_6\text{Ge}_{13}(\text{CO})_5]^{4-}$ (658 electrons)
<i>Lanl2dz</i>	500	Yes	Yes	Yes
	750	Yes	Yes	No
<i>CEP-121g</i>	500	Yes	Yes	Yes
	750	No	Yes	No

Since approximations and functions used in both basis sets are different, Lanl2dz and CEP-121g TD results (X-axis) were multiplied by their correction factors, which are 0.961 and 0.975, respectively.¹⁰⁷ The bands are simulated using Lorentzian broadening to obtain the spectra from the computed electronic transitions of isolated clusters (Gas phase band width: 4 cm^{-1} , DMF band width: 10 cm^{-1}).

3.4.1.1.1. Basis Set: Lanl2dz

An example to conversion of computed oscillator strengths into intensities is shown in Figure 3.8. Although 750 transitions were calculated, more transitions are required

to reach below 167 nm, which may shift the absorption maximum. Similarly, in the electronic transition spectra of the other clusters high energy transitions may not be achieved. Therefore, this study will only provide qualitative information.

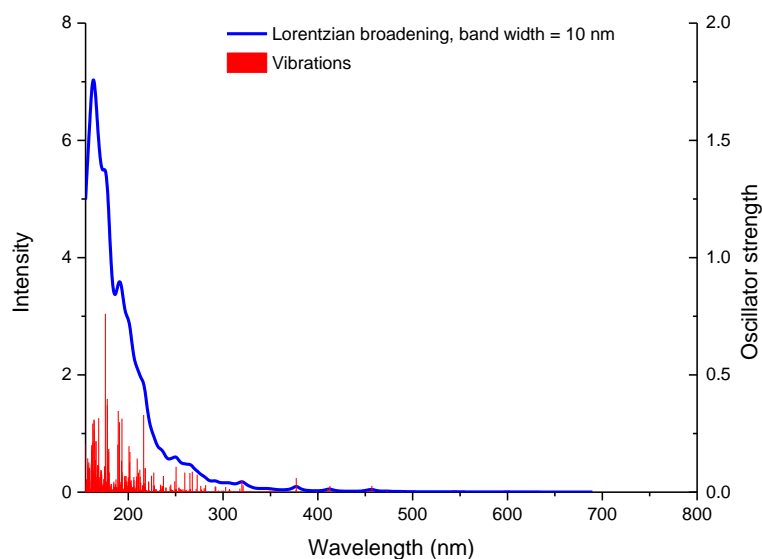


Figure 3.8. Lanl2dz TD spectrum of $[\text{Ni}_2\text{Ge}_9(\text{PPh}_3)]^{2-}$ in DMF with 750 transitions (broadened data in blue solid line, vibrations in red bars)

Simulated UV-Vis spectra of $[\text{Ni}_2\text{Ge}_9(\text{PPh}_3)]^{2-}$ (750 transitions), $[\text{Ni}_2\text{Ge}_9(\text{CO})]^{2-}$ (750 transitions) and $[\text{Ni}_6\text{Ge}_{13}(\text{CO})_5]^{4-}$ (500 transitions) in gas phase and DMF are shown in Figure 3.9. There are clear differences between the gas phase and solvent simulations since the clusters are in different environments. A comparison of $[\text{Ni}_2\text{Ge}_9(\text{PPh}_3)]^{2-}$ and $[\text{Ni}_2\text{Ge}_9(\text{CO})]^{2-}$ spectra suggest that 750 transitions might not be enough to evaluate the spectrum of $[\text{Ni}_2\text{Ge}_9(\text{PPh}_3)]^{2-}$. Considering $[\text{Ni}_6\text{Ge}_{13}(\text{CO})_5]^{4-}$ has a lot more electrons than the other two clusters, this molecule

may require 1000 transitions. To our knowledge, such high numbers of transitions were not reported before, and we are not sure if Gaussian is suitable for these type of calculations. As the transition states increase, the spectrum shifts to the higher energy. Therefore, in the following results, it is not certain whether the maximum absorption is real or a shoulder.

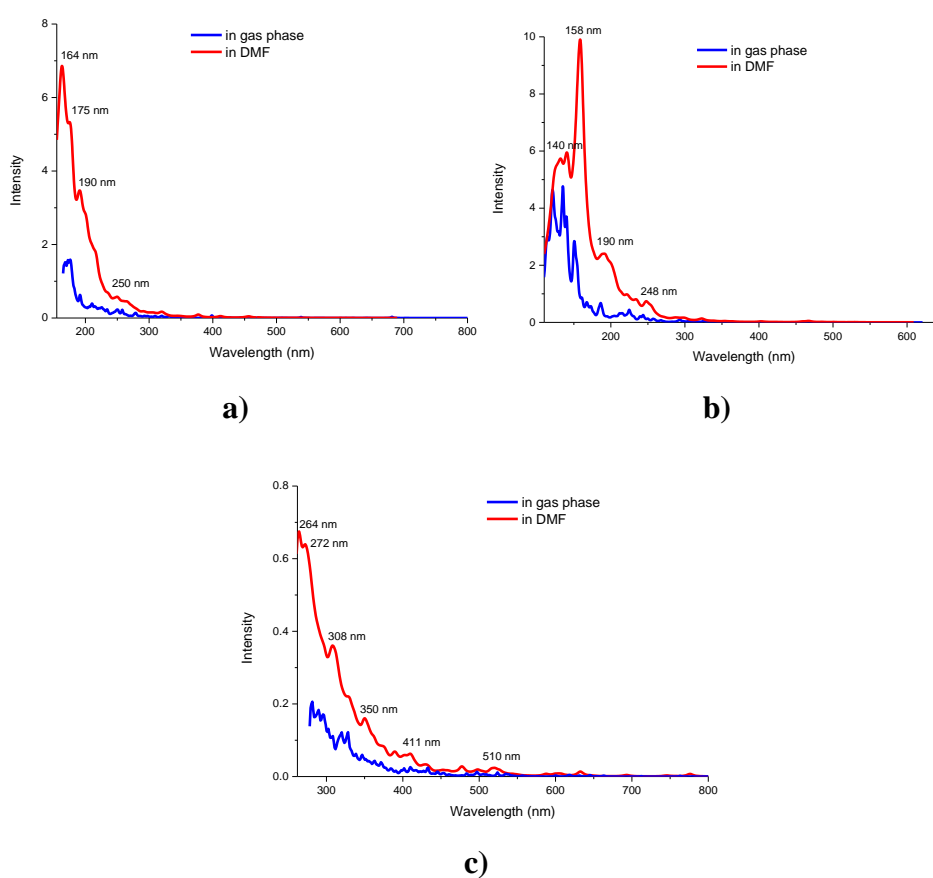


Figure 3.9. Lan12dz TD spectra of **a)** $[\text{Ni}_2\text{Ge}_9(\text{PPh}_3)]^{2-}$ with 750 transitions **b)** $[\text{Ni}_2\text{Ge}_9(\text{CO})]^{2-}$ with 750 transitions **c)** $[\text{Ni}_6\text{Ge}_{13}(\text{CO})_5]^{4-}$ with 500 transitions in gas phase (blue) and in DMF (red).

During the following discussions, the spectra are simulated with a 25 nm band-width and they are red-shifted such that absorption maxima is at 280 nm in order to compare with the experimental ones.(Figure 3.10.) Even though the complete simulations of all electronic transitions observed in experimental spectra may not be achieved, there are strong resemblances. Both the experimental and simulated spectra show very broad bands covering the entire region from UV to near-IR. In addition, the shoulder of $[\text{Ni}_6\text{Ge}_{13}(\text{CO})_5]^{4-}$ around 330 nm shown with green dashed rectangle resembles well to the experimental data.

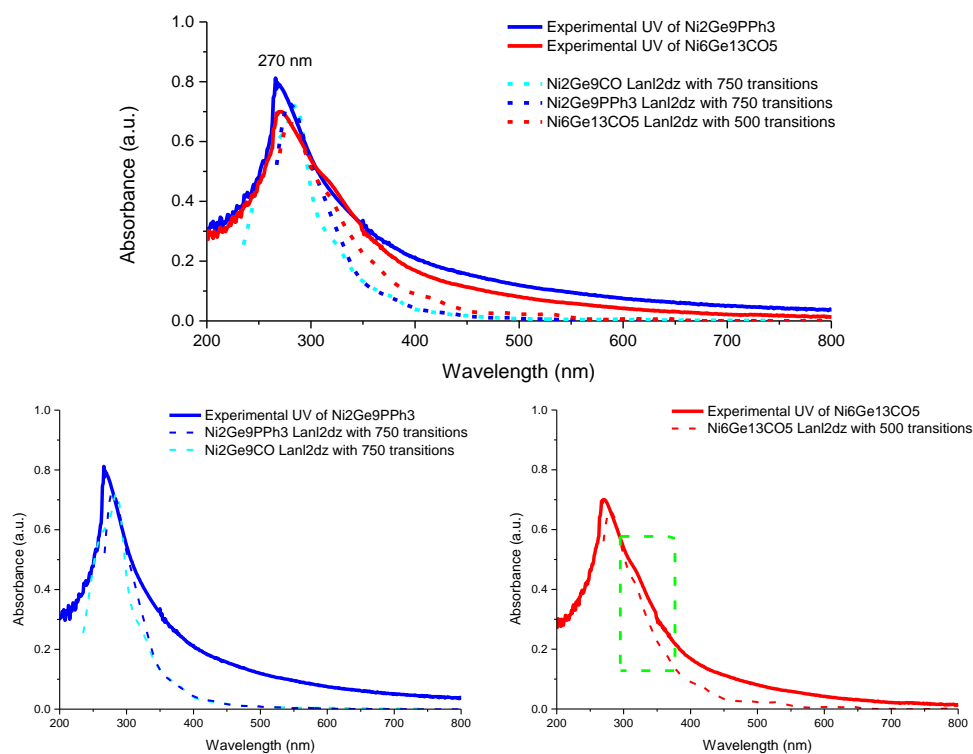


Figure 3.10. Experimental UV spectra of $[\text{Ni}_2\text{Ge}_9(\text{PPH}_3)]^{2-}$ (blue) and $[\text{Ni}_6\text{Ge}_{13}(\text{CO})_5]^{4-}$ (red) as solid lines; and computational TD spectra of $[\text{Ni}_2\text{Ge}_9(\text{PPH}_3)]^{2-}$ (blue), $[\text{Ni}_6\text{Ge}_{13}(\text{CO})_5]^{4-}$ (red) and $[\text{Ni}_2\text{Ge}_9(\text{CO})]^{2-}$ (cyan) in DMF as dash lines with Lanl2dz in 200-800 nm region.

3.4.1.1.2. Basis Set: CEP-121g

In CEP-121g calculations, 750 transitions were achieved only for $[\text{Ni}_2\text{Ge}_9(\text{CO})]^{2-}$ cluster. It might be due to more memory requirements of CEP-121g basis sets during these calculations. In all cases, CEP-121g based calculations required more time than Lanl2dz ones. The positions of transitions and their relative intensities of Lanl2dz and CEP-121g are also different, since they use different levels of approximation and functions.

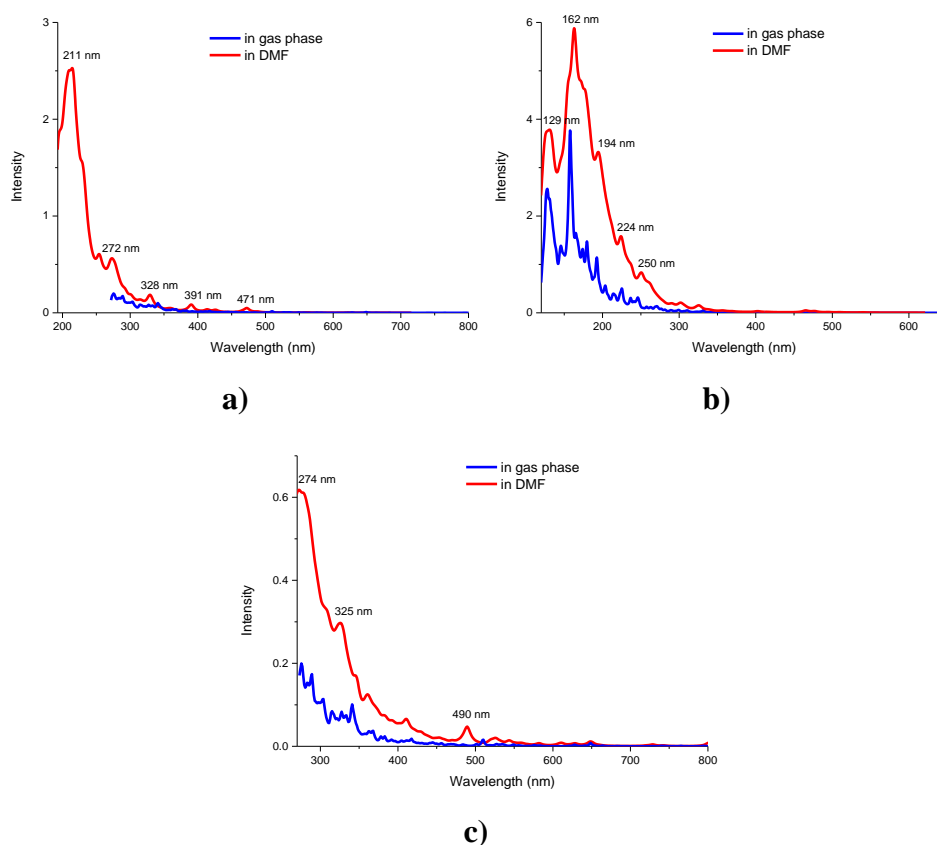


Figure 3.11. CEP-121g TD spectra of **a)** $[\text{Ni}_{12}\text{Ge}_9(\text{PPh}_3)]^{2-}$ with 500 transitions **b)** $[\text{Ni}_{12}\text{Ge}_9(\text{CO})]^{2-}$ with 750 transitions **c)** $[\text{Ni}_6\text{Ge}_{13}(\text{CO})_5]^{4-}$ with 500 transitions in gas phase (blue) and in DMF (red).

Even though the complete spectra were not simulated for the clusters, similar behaviors were observed.(Figure 3.11.) The bands are very broad possibly covering from UV to near-IR, and the shoulder around 330 nm is again present in the computational data of $[\text{Ni}_6\text{Ge}_{13}(\text{CO})_5]^{4-}$.(Figure 3.12.)

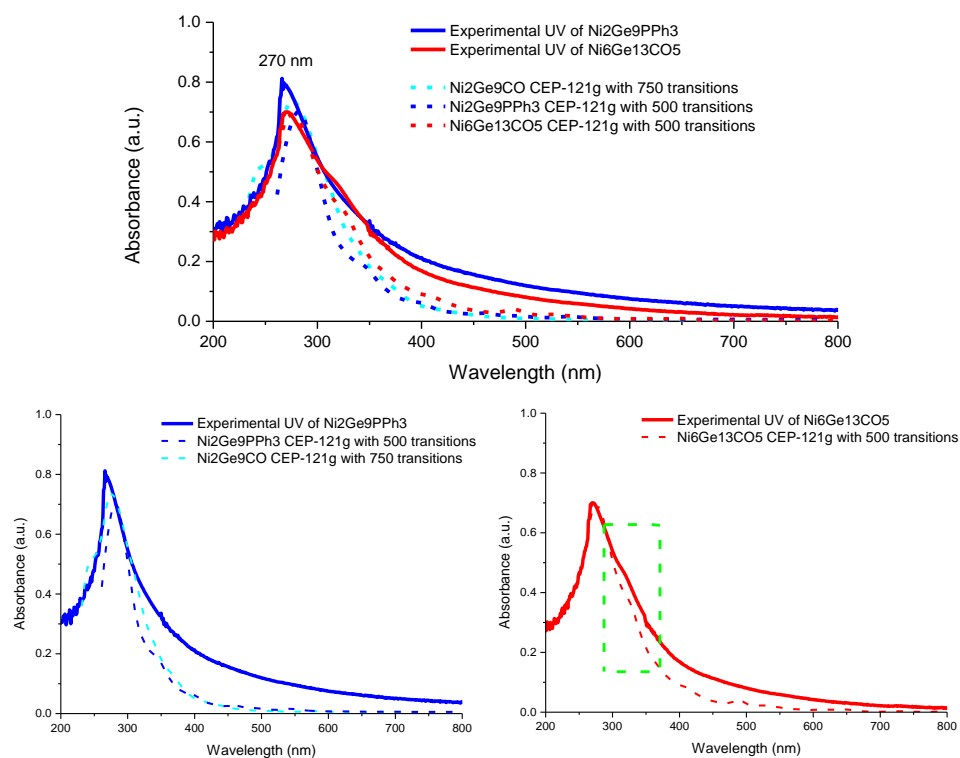


Figure 3.12. Experimental UV spectra of $[\text{Ni}_2\text{Ge}_9(\text{PPh}_3)]^{2-}$ (blue) and $[\text{Ni}_6\text{Ge}_{13}(\text{CO})_5]^{4-}$ (red) as solid lines; and computational TD spectra of $[\text{Ni}_2\text{Ge}_9(\text{PPh}_3)]^{2-}$ (blue), $[\text{Ni}_6\text{Ge}_{13}(\text{CO})_5]^{4-}$ (red) and $[\text{Ni}_2\text{Ge}_9(\text{CO})]^{2-}$ (cyan) in DMF as dash lines with CEP-121g in 200-800 nm region.

3.4.2. FTIR Spectrometry Analyses

FTIR measurements for $[\text{Ni}_2\text{Ge}_9(\text{PPh}_3)]^{2-}$ and $[\text{Ni}_6\text{Ge}_{13}(\text{CO})_5]^{4-}$ clusters are performed under different experimental conditions to obtain the best and the most reliable data possible. Two different solvent (DMF and paraffin oil) for dispersion of crystals and two different FTIR sample holder windows (TPX; polymethylpentene and KBr) are used. Regions of transmission differ depending on the solvent and window chosen, as they all have different absorptions in the IR region. These various

combinations allow us to collect data from as many regions as possible. This type of monitoring is very crucial since the extensive FTIR measurements of these types of clusters have not been reported before, thus there is no available data for comparison and/or assignment of the available features.

Due to the lack of reference FTIR data of these types of clusters, measurements on precursors used during the synthesis of clusters are considered as a very valuable guide to regions that will be focused on to determine the main features of the observed spectra. Therefore, FTIR spectra of K_4Ge_9 and $Ni(CO)_2(PPh_3)_2$ as precursors and $Pt(PPh_3)_4$ as another compound having PPh_3 ligand has become the starting point in this part of the study. As a result of these measurements the regions where M-M and M-L (M: Ni and/or Ge, L: PPh_3 or CO) bands might appear are determined and results contribute to identify the bands correspond to $[Ni_2Ge_9(PPh_3)]^{2-}$ and $[Ni_6Ge_{13}(CO)_5]^{4-}$. Thus, the transmission spectra of precursors collected between 2600 cm^{-1} and 20 cm^{-1} region is also shown in the following sections.

3.4.2.1. FTIR Spectra in DMF with TPX Windows

Background spectrum of pure DMF with TPX windows are performed firstly as reference to identify the possible regions that can be studied. These measurements show that there are three main regions of transmission as shown in Figure 3.13. Therefore, only these regions are studied and others excluded during analyses of Ni-Ge clusters.

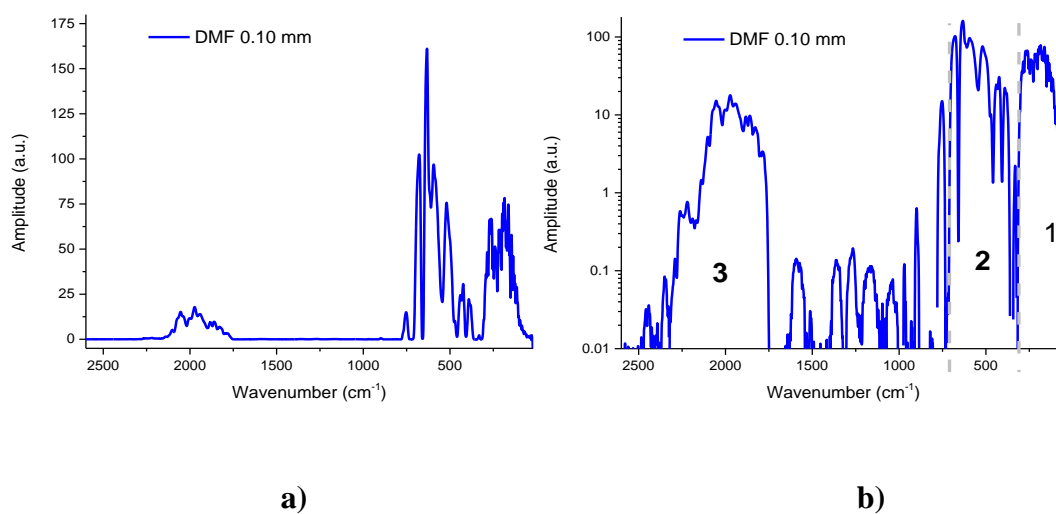


Figure 3.13. DMF absorption spectrum in **a)** Linear scale **b)** Log scale

In the following sections, color coding with rectangles are used for a better visualization of the similarities. Each color represents similar bands or group of bands. Moreover, in some parts of the analyzed regions, there are ‘no transmission’ regions they are covered with light grey rectangles.

The first region ($310\text{-}70\text{ cm}^{-1}$) is expected to correspond to the low energy metal-metal vibrational modes.¹⁰⁸(Figure 3.14.) However, due to the moisture very strong absorption bands (fairly sharp lines) are major handicaps to observe individual vibrational bands resulted from the clusters. Instead, a very broad signal with moisture as noise (all the sharp bands) is observed for both precursors and clusters as shown in Figure 3.14. Even though the bands are not very clearly observed, measurements in this region demonstrate that the combination of metal-metal bands appear as a very broad band around 200 cm^{-1} . The green curve is drawn to see this broad band more clearly in Figure 3.14.

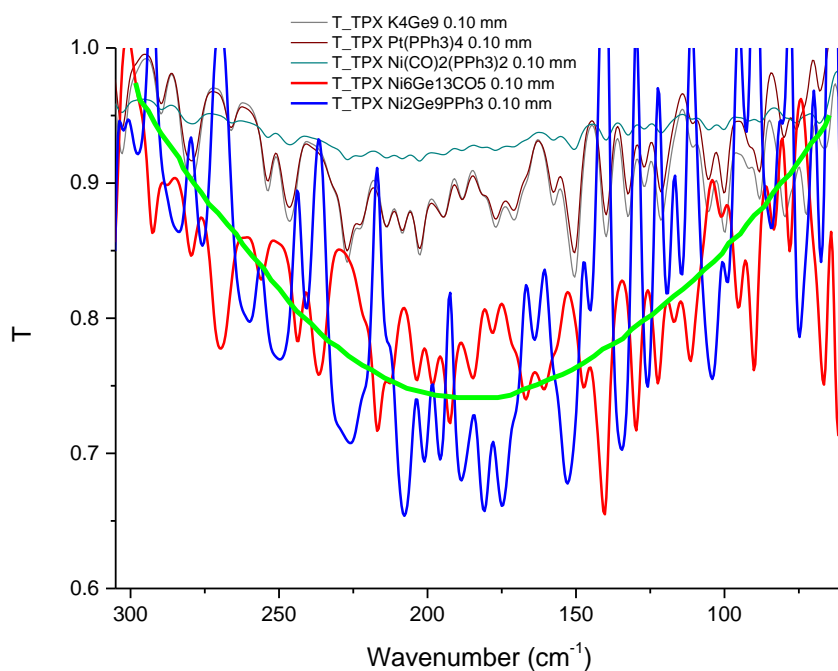


Figure 3.14. Transmission spectra of precursors (K_4Ge_9 , $\text{Pt}(\text{PPh}_3)_4$, $\text{Ni}(\text{CO})_2(\text{PPh}_3)_2$ as thin solid lines) and clusters ($[\text{Ni}_2\text{Ge}_9(\text{PPh}_3)]^{2-}$, $[\text{Ni}_6\text{Ge}_{13}(\text{CO})_5]^{4-}$ as solid lines) in DMF with TPX windows, 310-70 cm^{-1} .

In the second region (710-370 cm^{-1}), different vibrational modes of M-PPh_3 are expected to be observed.¹⁰⁹(Figure 3.15.) The measurements on PPh_3 containing compounds ($\text{Ni}(\text{CO})_2(\text{PPh}_3)_2$, $\text{Pt}(\text{PPh}_3)_4$) have shown bands at 496 cm^{-1} , 515 cm^{-1} , 545 cm^{-1} and 700 cm^{-1} that are common to all as different vibrational modes of PPh_3 attached to a metal. Not observing these bands in the spectrum of K_4Ge_9 verifies this observation. The band appeared at 496 cm^{-1} in the spectrum of $\text{Ni}(\text{CO})_2(\text{PPh}_3)_2$ precursor is considered to be Ni-P stretching band. The comparison of the spectra of Ni-Ge clusters with those precursors suggests that Ni-P stretching band might present around 470 cm^{-1} in PPh_3 -bearing Ni-Ge cluster.(Figure 3.15.) Even though the bands' closeness to the “no transmission region” (between 460 cm^{-1} and 410 cm^{-1})

make the reliability of it questionable, absence of any other band(s) makes this assignment probable. Also, observation of the band at 470 cm^{-1} in multiple measurements of different batches of sample suggests the reality of the band. The band observed at ca. 525 cm^{-1} is considered also to be one of the M-PPh₃ modes that are observed in precursors at ca. 515 cm^{-1} . The shoulder observed at ca. 530 cm^{-1} may correspond to the feature observed at 545 cm^{-1} for precursors. Unfortunately, there is no data available in literature to assign the observed features, thus the computational data will be very useful in the assignment. Similarly, a very broad feature centered at ca. 540 cm^{-1} is observed for CO-bearing cluster.

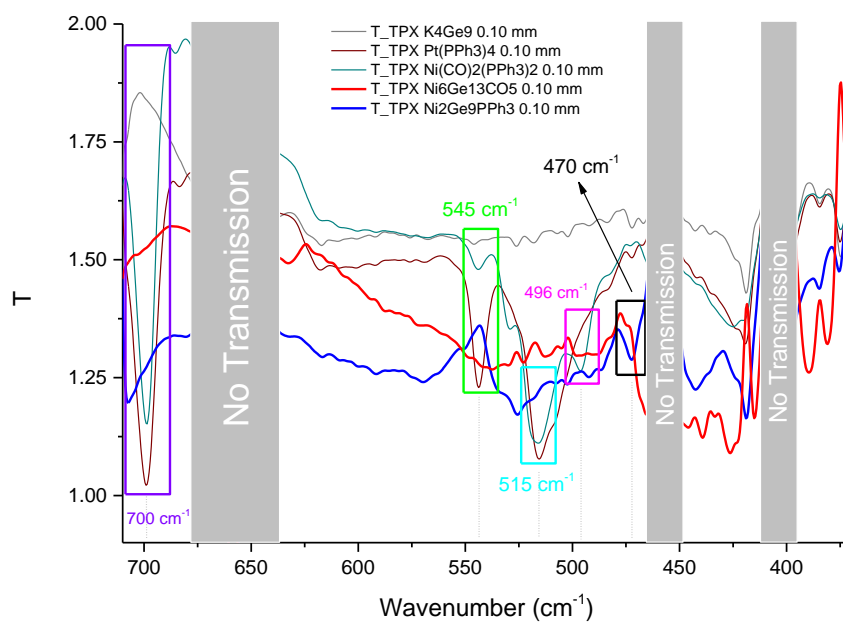


Figure 3.15. Transmission spectra of precursors (K_4Ge_9 , $\text{Pt}(\text{PPh}_3)_4$, $\text{Ni}(\text{CO})_2(\text{PPh}_3)_2$ shown as thin solid lines) and clusters ($[\text{Ni}_2\text{Ge}_9(\text{PPh}_3)]^{2-}$, $[\text{Ni}_6\text{Ge}_{13}(\text{CO})_5]^{4-}$ shown as solid lines) in DMF with TPX windows, $710\text{-}370\text{ cm}^{-1}$

In the third region (2100-1800 cm^{-1}) of the spectrum, CO stretching frequencies are present.(Figure 3.16.) Among all precursors studied only $\text{Ni}(\text{CO})_2(\text{PPh}_3)_2$ exhibits two main bands at 1996 cm^{-1} and 1936 cm^{-1} corresponding to CO stretching modes as expected. On the other hand, the spectrum of both cluster anions show a band at 1929 cm^{-1} even though only one of them, $[\text{Ni}_6\text{Ge}_{13}(\text{CO})_5]^{4-}$, possess CO groups. This observation suggests the co-crystallization of CO containing Ni-Ge clusters such as $[\text{Ni}_2\text{Ge}_9(\text{CO})]^{2-}$ along with the ones of $[\text{Ni}_2\text{Ge}_9(\text{PPh}_3)]^{2-}$. It also agrees with the mass spectrometry analysis of $[\text{Ni}_2\text{Ge}_9(\text{PPh}_3)]^{2-}$ where the signals of $\text{K}[\text{Ni}_2\text{Ge}_9\text{CO}]^-$ present as discussed in the previous section. Both ESI mass and FTIR spectra suggest that the removal of CO ligands are not completely achieved during the synthesis of $[\text{Ni}_2\text{Ge}_9(\text{PPh}_3)]^{2-}$, even though the reaction temperatures of two clusters ($[\text{Ni}_6\text{Ge}_{13}(\text{CO})_5]^{4-}$ and $[\text{Ni}_2\text{Ge}_9(\text{PPh}_3)]^{2-}$) are significantly different from each other, 45°C for $[\text{Ni}_6\text{Ge}_{13}(\text{CO})_5]^{4-}$ and 120°C for $[\text{Ni}_2\text{Ge}_9(\text{PPh}_3)]^{2-}$. The similarity of CO bands in the spectrum of two clusters may even suggest existence of trace amount of $[\text{Ni}_6\text{Ge}_{13}(\text{CO})_5]^{4-}$ anion crystals in the reaction batch of $[\text{Ni}_2\text{Ge}_9(\text{PPh}_3)]^{2-}$. The comparison of FTIR spectrum of precursor and clusters show a shift in the CO bands of clusters toward lower wavenumber region. This is most likely due to differences in coordination of CO ligands in precursor and cluster.

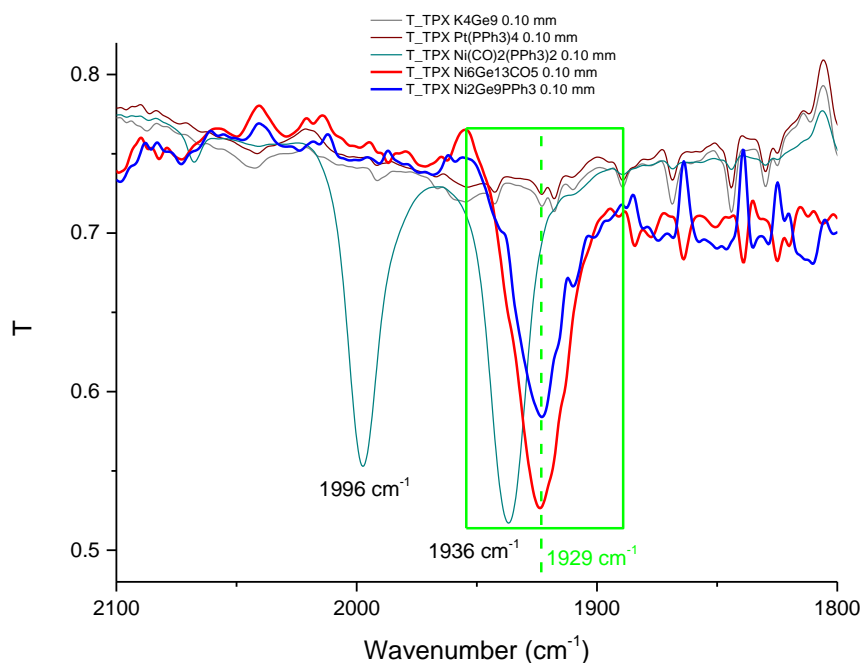


Figure 3.16. Transmission spectra of precursors (K_4Ge_9 , $Pt(PPh_3)_4$, $Ni(CO)_2(PPh_3)_2$ as thin solid lines) and clusters ($[Ni_2Ge_9(PPh_3)]^{2-}$, $[Ni_6Ge_{13}(CO)_5]^{4-}$ as solid lines) in DMF with TPX windows, 2100-1800 cm^{-1} .

3.4.2.2. FTIR Spectra in Paraffin Oil with TPX and KBr Windows

In this part of the study, FTIR spectra of the clusters are collected by dispersing crystals in paraffin oil. Here too, the measurements are done by using sample holders with two different windows (KBr and TPX). This allows almost complete monitoring of spectrum in a very wide range from 2600 cm^{-1} to 20 cm^{-1} . (Figure 3.17) Since the FTIR device has a polyethylene (PE) filter in front of the detector, background spectrum with KBr windows has absorption regions where PE absorbs the light. The regions analyzed with windows studied are shown in Table 3.6.

Table 3.6. Regions with KBr and TPX windows

	KBr	TPX
Region I	800-300 cm^{-1}	600-50 cm^{-1}
Region II	1350-800 cm^{-1}	-
Region III	2100-1800 cm^{-1}	2100-1800 cm^{-1}

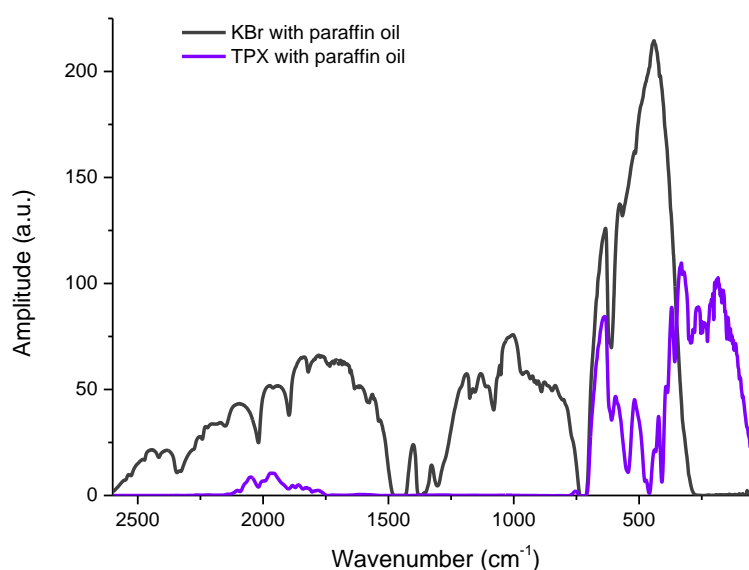


Figure 3.17. Absorption spectra of paraffin oil with KBr and TPX windows

In the first region ($600\text{-}50\text{ cm}^{-1}$) of TPX windows, K_4Ge_9 has a broad band near 104 cm^{-1} , which is probably a combination of Ge-Ge vibrational modes and/or the phonon mode of the molecule. We have not observed such a band in the spectra of clusters, thus this is more probably dominated by the phonon modes of the precursor. Both clusters exhibit a very similar behavior in this region. At 231 cm^{-1} and 155 cm^{-1}

¹, different vibrational modes of Ge-Ge, Ni-Ge and Ni-Ni is present, which is not observed in the precursors.¹⁰⁸ The shoulder band observed at ca. 125 cm⁻¹ might correspond to Ge-Ge vibrational modes as in K₄Ge₉ case. The main feature at 155 cm⁻¹ and the higher energy band at 231 cm⁻¹ is most probably an overlap of various modes of Ni-Ge clusters. A group of bands with maximum of 318 cm⁻¹ is possibly similar to the ones of Pt(PPh₃)₄ and Ni(CO)₂(PPh₃)₂ observed below the no transmission zone at 450 cm⁻¹ (shown with a green rectangle). Here, variation in intensities and shift in band positions is considered due to the change in PPh₃ environment. In addition, some parts of the precursor data is in the 'no transmission' zone; therefore, some bands may not be isolated completely.(Figure 3.18.) The features are clearer in the KBr window measurements and shown below in Figure 3.19. The features observed between 500 cm⁻¹ and 600 cm⁻¹ are also possibly due to the metal attached PPh₃ and CO modes (grey rectangle), and correlate with the ones observed in the same region of precursors. The variation in intensities and shift in band positions is due to the variation in bonding and environment changes of the PPh₃ and CO ligands. These observed bands are tentatively assigned to the fundamental M-PPh₃ and M-CO fundamental bands with the help of data obtained from computational studies. However, the co-presence of all the clusters does complicate the detailed analysis. The computational and experimental results will be compared after all regions are discussed individually.

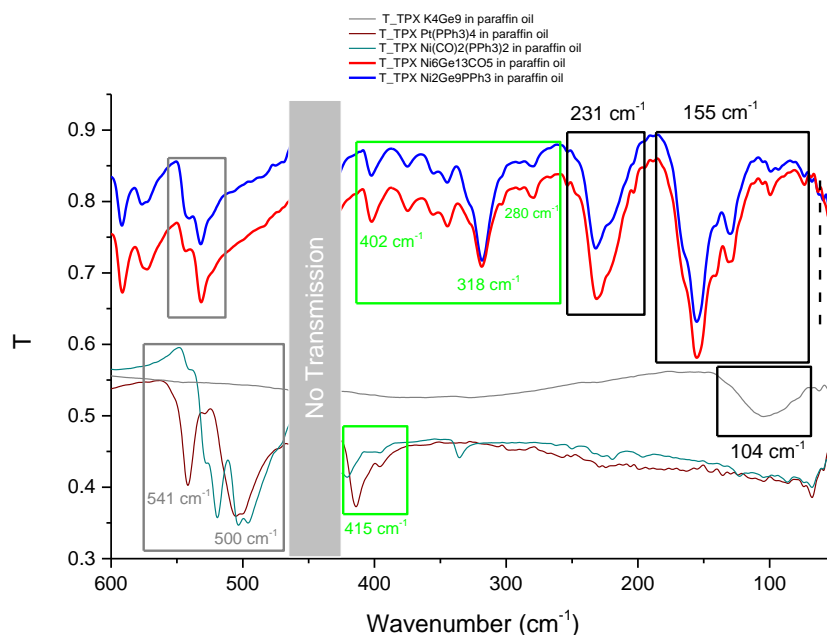


Figure 3.18. Transmission spectra of precursors (K_4Ge_9 , $\text{Pt}(\text{PPh}_3)_4$, $\text{Ni}(\text{CO})_2(\text{PPh}_3)_2$ as thin solid lines) and clusters ($[\text{Ni}_2\text{Ge}_9(\text{PPh}_3)]^{2-}$, $[\text{Ni}_6\text{Ge}_{13}(\text{CO})_5]^{4-}$ as solid lines) in paraffin oil with TPX windows, 600-50 cm^{-1} .

In the first transmission region with KBr windows (800-300 cm^{-1}), more bands are observed since KBr transmits near 410 cm^{-1} . (Figure 3.19.) The combination of bands observed for $\text{Pt}(\text{PPh}_3)_4$ and $\text{Ni}(\text{CO})_2(\text{PPh}_3)_2$ around 415 cm^{-1} (green rectangle) is very similar to the ones observed for the clusters, and confirms our observations with the TPX windows. The fairly strong and sharp band observed in Pt-precursor at 415 cm^{-1} and the band of Ni-precursor at ca. 425 cm^{-1} is most probably correspond to M-P stretching mode.¹⁰⁹ Thus the strong band observed at 319 cm^{-1} probably corresponds to Ni-P vibrational mode. The sharp feature of Ni-precursor observed at ca. 450 cm^{-1} is most probably M-CO stretching mode,¹¹⁰ since it is comparably weaker in Pt-precursor. Thus, the two bands of the clusters observed around 420 cm^{-1} is considered to be Ni-CO stretching bands. The group of bands of PPh_3 containing

precursors above 500 cm^{-1} , shown with grey rectangle, is similar to the cluster features observed in the same region. These bands are considered to be different vibrational modes of Ni-P and P-C.¹¹¹ Due to ‘No transmission’ zone around 700 cm^{-1} , it is not possible to identify the bands of cluster compared to the sharp band of PPh_3 containing precursors at 690 cm^{-1} .(Figure 3.19.)

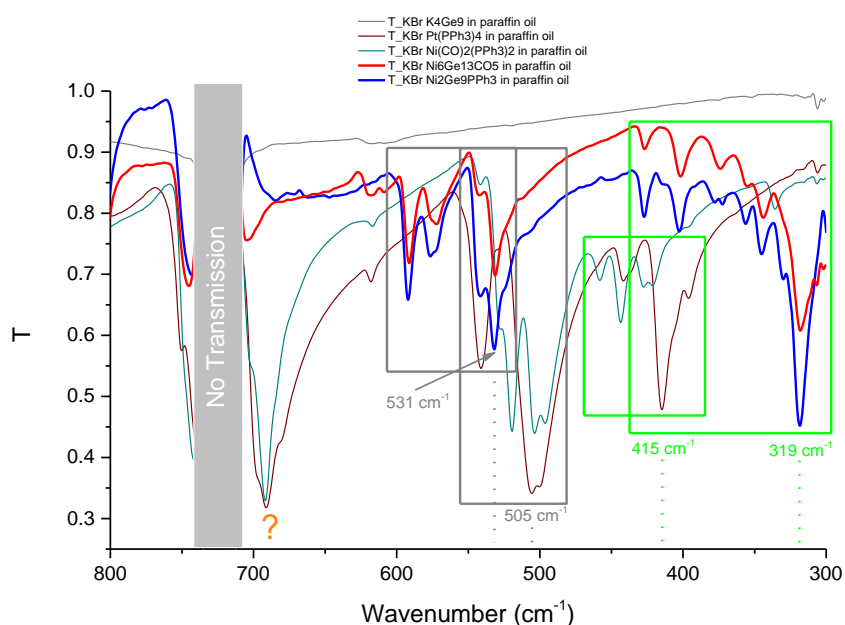


Figure 3.19. Transmission spectra of precursors (K_4Ge_9 , $\text{Pt}(\text{PPh}_3)_4$, $\text{Ni}(\text{CO})_2(\text{PPh}_3)_2$ as thin solid lines) and clusters ($[\text{Ni}_2\text{Ge}_9(\text{PPh}_3)]^{2-}$, $[\text{Ni}_6\text{Ge}_{13}(\text{CO})_5]^{4-}$ as solid lines) in paraffin oil with KBr windows, $800\text{-}300\text{ cm}^{-1}$.

In second region of KBr windows ($1350\text{-}800\text{ cm}^{-1}$), similar group of bands are shown with light blue and green rectangles.(Figure 3.20.) These bands are probably the different vibrational modes of P-C in PPh_3 .¹¹¹

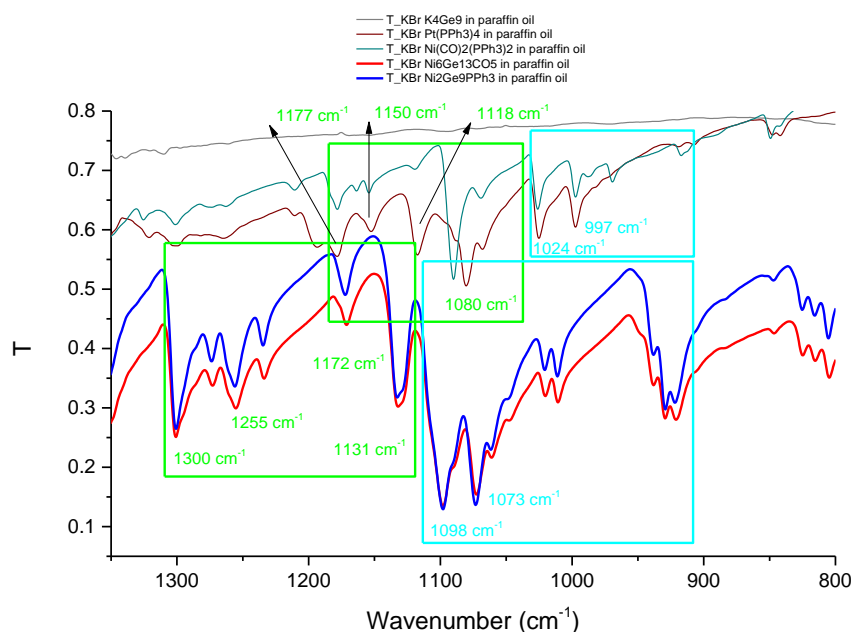
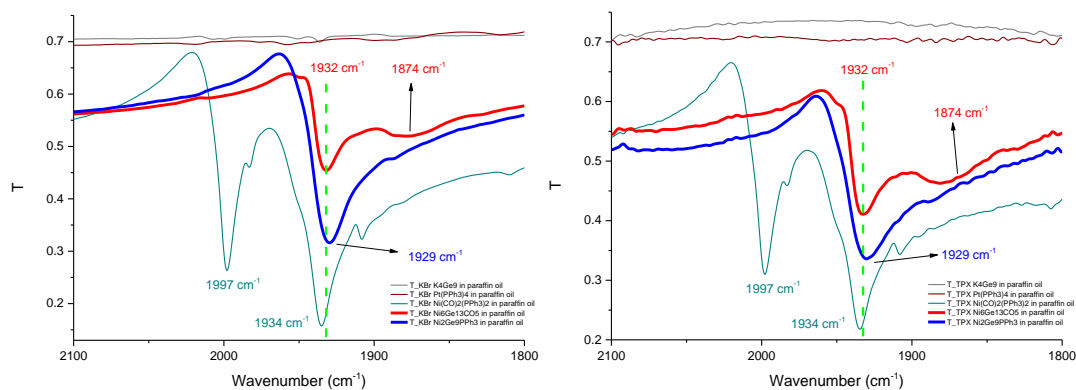


Figure 3.20. Transmission spectra of precursors (K_4Ge_9 , $\text{Pt}(\text{PPh}_3)_4$, $\text{Ni}(\text{CO})_2(\text{PPh}_3)_2$ as thin solid lines) and clusters ($[\text{Ni}_2\text{Ge}_9(\text{PPh}_3)]^{2-}$, $[\text{Ni}_6\text{Ge}_{13}(\text{CO})_5]^{4-}$ as solid lines) in paraffin oil with KBr windows, 1350-800 cm^{-1} .

In the third region of KBr and TPX windows (2100-1800 cm^{-1}), CO stretching modes are observed. $\text{Ni}(\text{CO})_2(\text{PPh}_3)_2$ has two intense CO stretching bands at 1997 cm^{-1} and 1934 cm^{-1} . Similarly, both clusters exhibit a strong CO band around 1930 cm^{-1} . Different from the DMF measurements, $[\text{Ni}_6\text{Ge}_{13}(\text{CO})_5]^{4-}$ has also a broad shoulder near 1875 cm^{-1} , possibly corresponding to the bridging CO. (Figure 3.21.) Observing CO stretching band that should not be observed for $[\text{Ni}_2\text{Ge}_9(\text{PPh}_3)]^{2-}$ cluster suggests co-crystallization of CO containing cluster crystals as well.



a)

b)

Figure 3.21. Transmission spectra of precursors (K_4Ge_9 , $Pt(PPh_3)_4$, $Ni(CO)_2(PPh_3)_2$ as thin solid lines) and clusters ($[Ni_2Ge_9(PPh_3)]^{2-}$, $[Ni_6Ge_{13}(CO)_5]^{4-}$ as solid lines) in paraffin oil with **a)** KBr windows **b)** TPX windows, 2100-1800 cm^{-1} .

3.4.3. Results of Frequency Calculations for $[Ni_2Ge_9(PPh_3)]^{2-}$, $[Ni_2Ge_9(CO)]^{2-}$ and $[Ni_6Ge_{13}(CO)_5]^{4-}$

Vibrational spectra drawn from the outputs of calculations with Lanl2dz and CEP-121g basis sets are shown in the following sections. Since approximations and functions used in both basis sets are different, Lanl2dz and CEP-121g frequency results (X-axis) were multiplied by their correction factors, which are 0.961 and 0.975, respectively.¹⁰⁷ Then, Lorentzian broadening was applied on the vibrational data by using ChemCraft in order to obtain IR spectra. For gas phase calculations, the band width is 4 cm^{-1} , whereas for DMF-based calculations it is chosen as 10 cm^{-1} for both basis sets and all clusters.

In overall, relative peak positions of the vibrations are almost the same in both gas phase and DMF-based calculations. However, some bands have been separated from each other, and intensities are higher/enhanced under the influence of DMF.

3.4.3.1. Basis Set: Lanl2dz

For $[\text{Ni}_2\text{Ge}_9(\text{PPh}_3)]^{2-}$, there are four main groups of bands in the region of 1750-20 cm^{-1} . These bands were identified as different metal-metal (Ni-Ni, Ni-Ge, Ge-Ge), nickel-phosphorous, phosphorous-carbon, carbon-carbon and carbon-hydrogen of PPh_3 modes.(Figure 3.22.) There is no observed band between 2600 cm^{-1} and 1750 cm^{-1} . Such an investigation enables us to determine/identify the vibrational features observed in experimental measurements. The computational infrared spectra of the clusters with Lanl2dz basis set show many different metal-metal vibrational modes in region between 310-20 cm^{-1} . The Ni-Ni stretching is clearly identified at 310 cm^{-1} , whereas the others are appear to be more complex cluster modes involving many atoms. In a study of $\text{Et}_3\text{Sn-GePh}_3$, Sn-Ge stretching is reported at 230 cm^{-1} .¹⁰⁸ Considering Ni is lighter than Ge and Sn (Ni: 58.69 g/mol, Ge: 72.61 g/mol, Sn: 118.71 g/mol), its stretching frequency is expected to be higher than Ge-Sn one.

The region between 510-410 cm^{-1} is identified as nickel-phosphorous region, and Ni-P stretching is observed at 510 cm^{-1} with the high intensity. In a study of $(\text{CO})_3\text{NiP}(\text{GeMe}_3)_3$, Ni-P stretching is reported to be at 454 cm^{-1} .¹⁰⁹ Such a difference in the band position suggests strong dependence on the coordination. Various modes of triphenylphosphine occur between 1570 cm^{-1} and 605 cm^{-1} . In literature, vibrational modes of carbon-carbon (aromatic), phenyl-phosphorous, and phosphorous carbon are generally present in the regions of 1600-1400 cm^{-1} , 1440-1000 cm^{-1} , and 750-650 cm^{-1} , respectively.^{111,112} In general, phosphorous modes have higher intensity than carbon-carbon or carbon-hydrogen modes. The computational results have shown clear separation of the functional modes. Therefore, they are very

helpful on identifying regions, which will be very useful in determination of vibrational modes observed in experimental measurements.

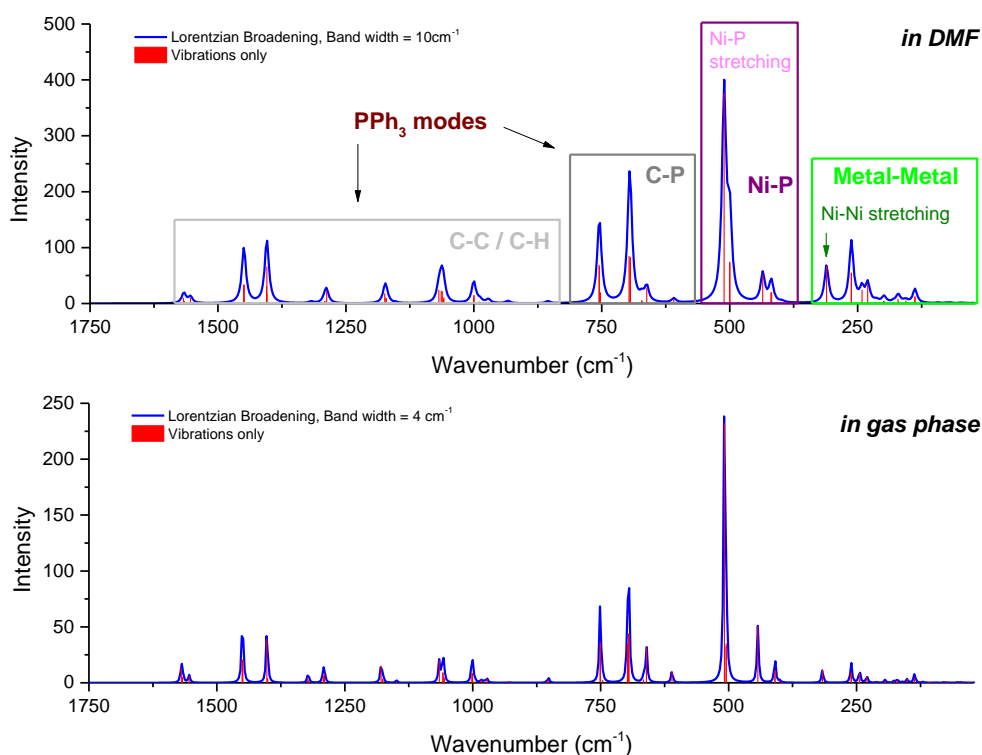


Figure 3.22. Computational IR spectra of $[\text{Ni}_2\text{Ge}_9(\text{PPh}_3)]^{2-}$ in DMF and gas phase with LanL2dz in 1750-20 cm⁻¹ region.

For $[\text{Ni}_2\text{Ge}_9(\text{CO})]^{2-}$, there are four groups of bands which are identified as metal-metal modes, nickel-carbon stretching, metal-carbonyl bending and carbon-oxygen stretching as a sharp band at 1761 cm⁻¹. (Figure 3.23.) The total number of vibrational modes for this cluster is 33 (N is 13). In the metal-metal region (272-20 cm⁻¹), Ni-Ni stretching is observed at 272 cm⁻¹, which is different from the $[\text{Ni}_2\text{Ge}_9(\text{PPh}_3)]^{2-}$ case.

Ni-C stretching and Ni-CO bending are located at 538 cm^{-1} and 410 cm^{-1} , respectively. In a study of $(\text{Et}_2\text{GaF})_3$, Ga-C stretching is reported at 538 cm^{-1} ¹¹³, while in AlPh_3 different modes of Al-C are reported at 332 cm^{-1} , 420 cm^{-1} , 446 cm^{-1} , 680 cm^{-1} ¹¹⁰ (Al: 26.98 g/mol, Ga: 69.72 g/mol). The observed Ni-C stretching mode at 538 cm^{-1} of the cluster is within the region of Ga-C and Al-C stretching modes ($680\text{--}332\text{ cm}^{-1}$). The observed relative intensity of the carbonyl stretching at 1760 cm^{-1} is significantly more than the Ni-P stretching in $[\text{Ni}_2\text{Ge}_9(\text{PPh}_3)]^{2-}$.

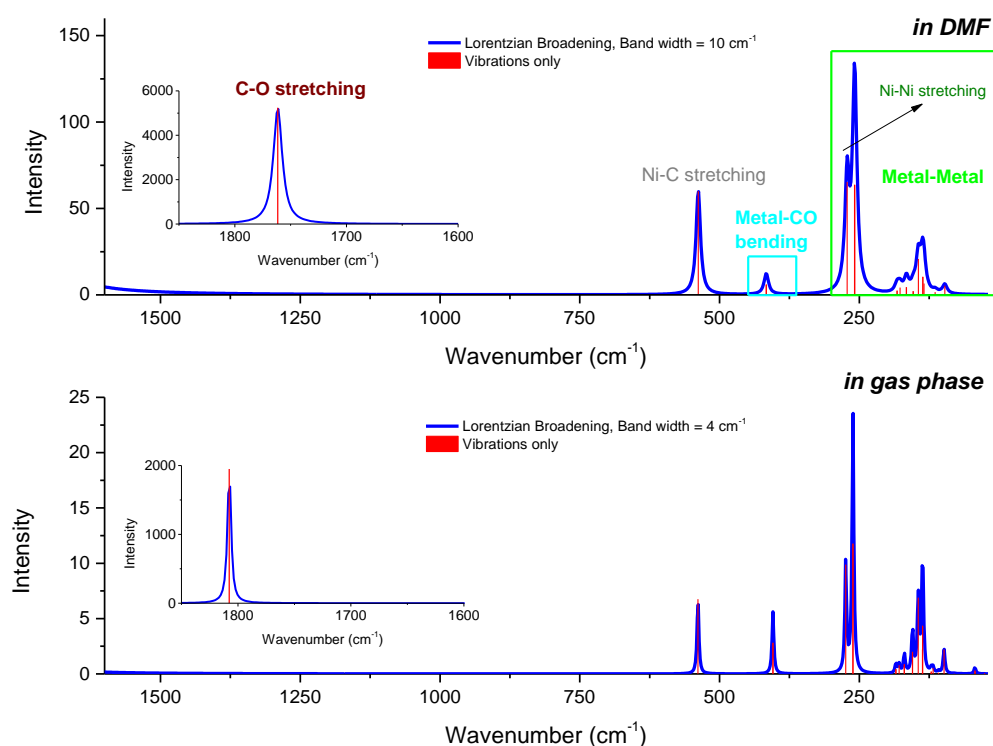


Figure 3.23. Computational IR spectra of $[\text{Ni}_2\text{Ge}_9(\text{CO})]^{2-}$ in DMF and gas phase with Lanl2dz in $1850\text{--}1600\text{ cm}^{-1}$ and $1625\text{--}20\text{ cm}^{-1}$ regions.

For $[\text{Ni}_6\text{Ge}_{13}(\text{CO})_5]^{4-}$, there are three groups of bands identified as metal-metal modes, metal-carbonyl bending and carbonyl stretching modes. (Figure 3.24.) The total number of vibrational modes for this cluster is 81 (N is 19). Since it has more metal atoms than the other two clusters, there are more vibrations in metal-metal region ($260\text{-}20\text{ cm}^{-1}$). The Ni-Ni stretching band of the two interstitial nickel atoms is at 258 cm^{-1} , which is lower in frequency than the one in $[\text{Ni}_2\text{Ge}_9(\text{PPh}_3)]^{2-}$ cluster. This is expected because nickel atoms are bonded to more germanium atoms in $[\text{Ni}_6\text{Ge}_{13}(\text{CO})_5]^{4-}$ resulting a red shift. Ni-CO bending modes are present in between 510 cm^{-1} and 347 cm^{-1} , which is also the region where nickel-phosphorous modes observed in $[\text{Ni}_2\text{Ge}_9(\text{PPh}_3)]^{2-}$. Therefore, overlaps of bands are expected in the co-crystal formation. Carbonyl stretching bands are at 1783 cm^{-1} , 1762 cm^{-1} , 1747 cm^{-1} , 1742 cm^{-1} for terminal carbonyls and 1620 cm^{-1} for the bridging one. Normally, 3 separate carbonyl bands (2 different terminal + 1 bridging carbonyls) would be expected since the structure has C_s symmetry. However, after optimization with Gaussian the structure of has C_1 symmetry, thus all the carbonyls are different from each other. Therefore, all carbonyl groups exhibit separate bands. The bridging carbonyl has lower frequency than the others since the π back-bonding from the metal to the carbon increases as two metals donate electrons. This strengthens the metal-carbon bond but weakens the carbon-oxygen bond at the same time, so the bridging carbonyl has a lower vibrational frequency.¹¹⁴

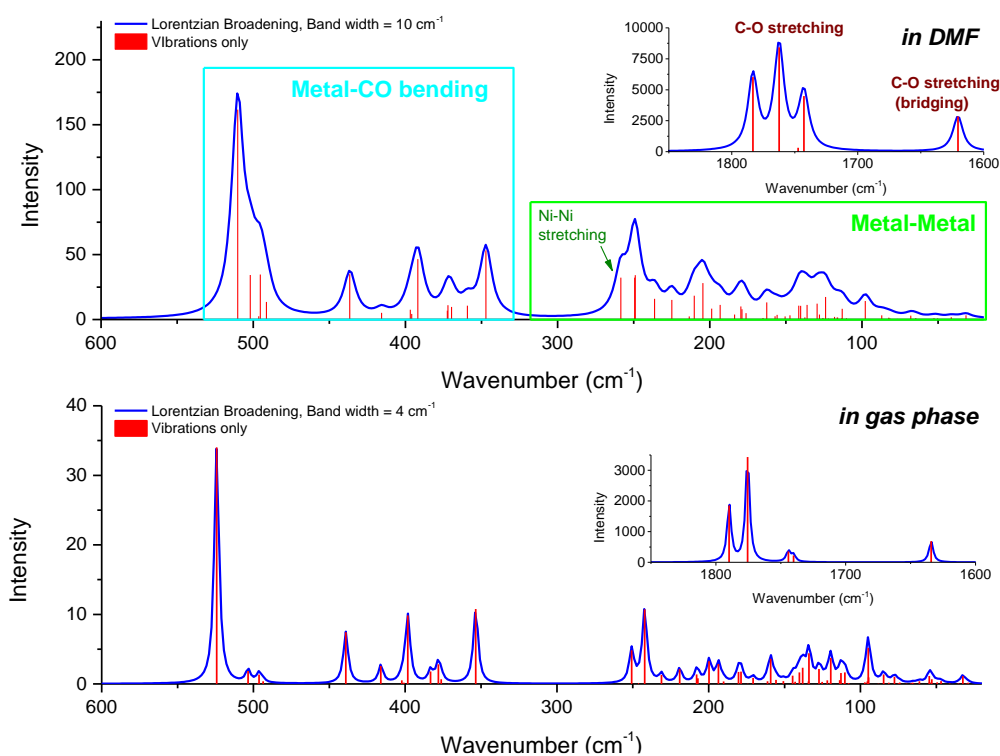


Figure 3.24. Computational IR spectra of $[\text{Ni}_6\text{Ge}_{13}(\text{CO})_5]^{4-}$ in DMF and gas phase with Lan12dz in 1850-1600 cm^{-1} and 600-20 cm^{-1} regions.

3.4.3.1.1. Comparison of Lan12dz Calculations with Experimental Results

Computational results provided a guide for identification of the possible vibrational bands in the FTIR spectra of the clusters. For ease of comparison with experimental data all the spectra are flipped and translated in y-scale. Since Gaussian does not have an option for paraffin oil as a dispersion solvent, DMF-based calculations are chosen to be compared with the FTIR data. The bands in DMF-based calculations are more separated and resembles to the experimental data.

As in the case of precursor comparison in *Section 3.4.2.2.*, the spectra are divided into regions.(Table 3.6.) Similar bands or group of bands are shown with the same colored rectangles. The first region of TPX divided into two parts to investigate metal-metal region separately to provide better visualization of the bands.(Figure 3.25)

In the metal-metal region with TPX windows, the combination of frequency calculations of three clusters ($[\text{Ni}_2\text{Ge}_9(\text{PPh}_3)]^{2-}$, $[\text{Ni}_6\text{Ge}_{13}(\text{CO})_5]^{4-}$, $[\text{Ni}_2\text{Ge}_9(\text{CO})]^{2-}$) revealed similar bands with the experimental data as three groups of bands (grey, green and black rectangles), which actually strengthens the idea of having co-crystals in the same solution.(Figure 3.25) In the computational data, the Ni-Ni stretching bands are located at 310 cm^{-1} , 258 cm^{-1} , 272 cm^{-1} for $[\text{Ni}_2\text{Ge}_9(\text{PPh}_3)]^{2-}$, $[\text{Ni}_6\text{Ge}_{13}(\text{CO})_5]^{4-}$, $[\text{Ni}_2\text{Ge}_9(\text{CO})]^{2-}$ clusters, respectively. Therefore, the band at 318 cm^{-1} , the one at 280 cm^{-1} , and the shoulder at 303 cm^{-1} of the experimental cluster data is most probably the Ni-Ni stretching band of $[\text{Ni}_2\text{Ge}_9(\text{PPh}_3)]^{2-}$, $[\text{Ni}_6\text{Ge}_{13}(\text{CO})_5]^{4-}$, $[\text{Ni}_2\text{Ge}_9(\text{CO})]^{2-}$ clusters, respectively. The rest of the observed features correspond to low frequency vibrational modes that include roughly the whole cluster (all Ge-Ni atoms). Considering the K_4Ge_9 spectra the feature at ca. 50 cm^{-1} might be Ge-Ge stretching modes or a phonon mode of the crystals.

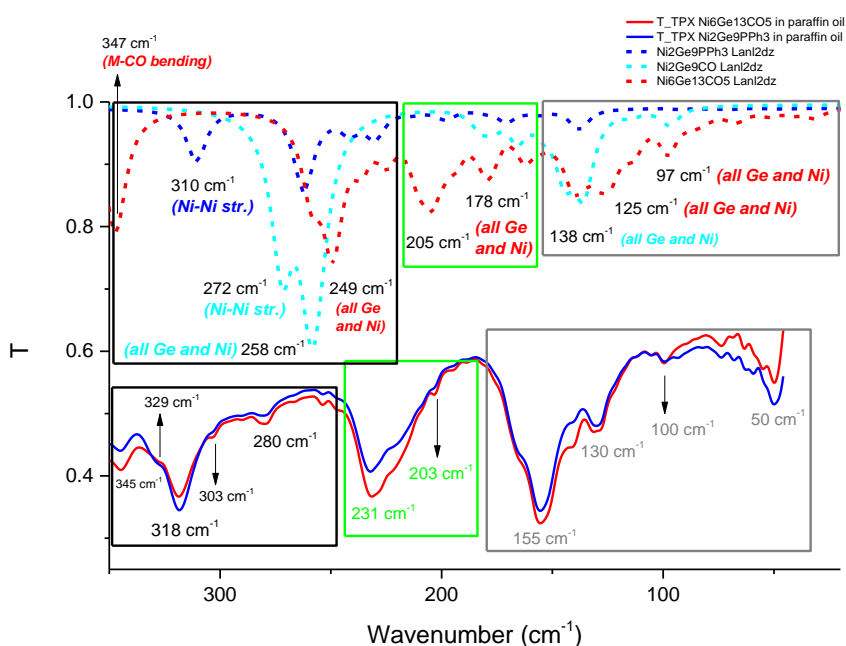


Figure 3.25. Experimental FTIR spectra of $[\text{Ni}_2\text{Ge}_9(\text{PPh}_3)]^{2-}$ (blue) and $[\text{Ni}_6\text{Ge}_{13}(\text{CO})_5]^{4-}$ (red) as solid lines with TPX windows; and computational IR spectra of $[\text{Ni}_2\text{Ge}_9(\text{PPh}_3)]^{2-}$ (blue), $[\text{Ni}_6\text{Ge}_{13}(\text{CO})_5]^{4-}$ (red) and $[\text{Ni}_2\text{Ge}_9(\text{CO})]^{2-}$ (cyan) as dash lines with Lanl2dz in 350-20 cm^{-1} region.

Table 3.7 lists relative differences of the computed and experimentally observed bands. The average of differences is 17 cm^{-1} for this region, which is very reasonable since the spectra are obtained from the optimized geometry in DMF rather than in paraffin oil.

Table 3.7. Differences in selected peak positions in Figure 3.25.

<i>Regions</i>	Computational (Lanl2dz)	Experimental	Difference
<i>Metal-Metal</i>	97 cm ⁻¹	100 cm ⁻¹	- 3 cm ⁻¹
	125 cm ⁻¹	130 cm ⁻¹	- 5 cm ⁻¹
	138 cm ⁻¹	155 cm ⁻¹	- 17 cm ⁻¹
	178 cm ⁻¹	203 cm ⁻¹	- 25 cm ⁻¹
	205 cm ⁻¹	231 cm ⁻¹	- 26 cm ⁻¹
	249 cm ⁻¹	280? cm ⁻¹	- 31 cm ⁻¹
	258 cm ⁻¹	280 cm ⁻¹	- 22 cm ⁻¹
	272 cm ⁻¹	303 cm ⁻¹	- 31 cm ⁻¹
	310 cm ⁻¹	318 cm ⁻¹	-8 cm ⁻¹
	345 cm ⁻¹	347 cm ⁻¹	- 2 cm ⁻¹
	<i>Average difference (Absolute)</i>		

In the second region of TPX windows (700-350 cm⁻¹), green rectangle represents the different vibrational modes of nickel-phosphorous and metal-carbonyl bending based on the computational results.(Figure 3.26.) The nickel-carbonyl stretching mode of [Ni₆Ge₁₃(CO)₅]⁴⁺ appears at 538 cm⁻¹. Nickel-phosphorous stretching in [Ni₂Ge₉(PPh₃)₂]²⁻ is present at 510 cm⁻¹, where one of the carbonyl bending modes of [Ni₆Ge₁₃(CO)₅]⁴⁺ also takes place. Other metal-carbonyl bending modes of CO-containing clusters occur between 510 cm⁻¹ and 350 cm⁻¹. However, metal-carbonyl bending of [Ni₆Ge₁₃(CO)₅]⁴⁺ and nickel-phosphorous stretching bands of [Ni₂Ge₉(PPh₃)₂]²⁻ overlap at 510 cm⁻¹ and ca. 495 cm⁻¹, and cannot be distinguished from each other. Therefore, it is not possible to identify the bands at 531 cm⁻¹ and 522 cm⁻¹ in the experimental data of clusters as metal-carbonyl bending or nickel-phosphorous stretching. However, there is a clear difference in the ratio of 541 cm⁻¹

to 531 cm^{-1} bands of the two clusters, thus the relatively stronger band at 541 cm^{-1} must correspond either to nickel-carbonyl stretching mode of $[\text{Ni}_6\text{Ge}_{13}(\text{CO})_5]^{4-}$ or to nickel-phosphorous stretching mode of $[\text{Ni}_2\text{Ge}_9(\text{PPh}_3)]^{2-}$. The other computational bands of $[\text{Ni}_2\text{Ge}_9(\text{PPh}_3)]^{2-}$ and $[\text{Ni}_6\text{Ge}_{13}(\text{CO})_5]^{4-}$ at 435 cm^{-1} , 392 cm^{-1} and 371 cm^{-1} are similar to the bands that are experimentally observed at 427 cm^{-1} , 401 cm^{-1} and 375 cm^{-1} for the clusters. The group of bands shown with black rectangle could not be paired with any of the bands in the computational results. The bands depicted in the orange rectangle does corresponds to the modes of nickel bonded PPh_3 group and have also been observed in the spectra of PPh_3 containing precursors $\text{Pt}(\text{PPh}_3)_4$, $\text{Ni}(\text{CO})_2(\text{PPh}_3)_2$. However, the band may be blue-shifted to higher frequencies such as the others and beyond 700 cm^{-1} thus may not be observed in the spectra of the clusters. The differences between the computational and experimentally determined bands are listed in Table 3.8.

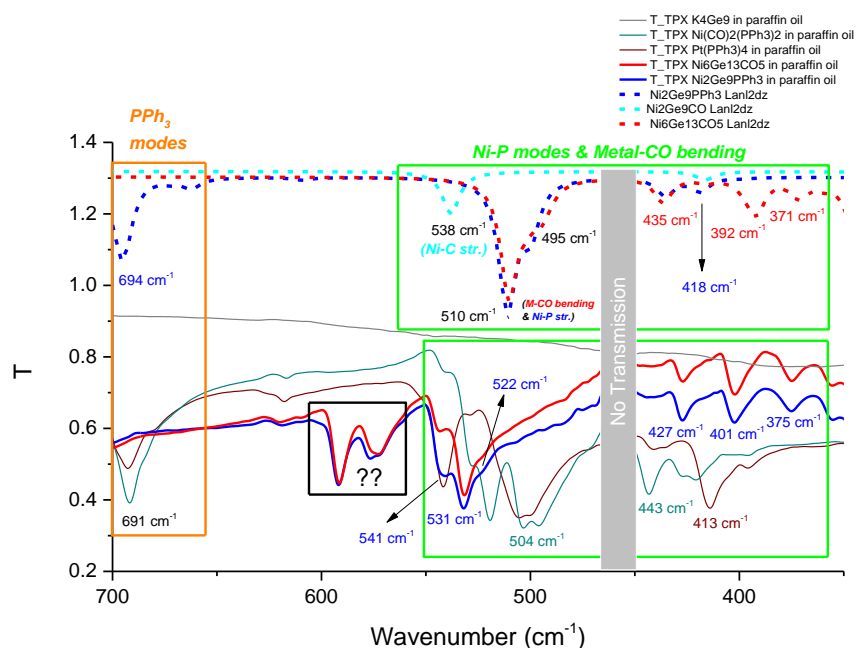


Figure 3.26. Experimental FTIR spectra of K₄Ge₉ (grey), Pt(PPh₃)₄ (wine), Ni(CO)₂(PPh₃)₂ (dark cyan) as thin solid lines, [Ni₂Ge₉(PPh₃)₂]²⁻ (blue) and [Ni₆Ge₁₃(CO)₅]⁴⁻ (red) as solid lines with TPX windows; and computational IR spectra of [Ni₂Ge₉(PPh₃)₂]²⁻ (blue), [Ni₆Ge₁₃(CO)₅]⁴⁻ (red) and [Ni₂Ge₉(CO)]²⁻ (cyan) as dash lines with Lanl2dz in 700-350 cm⁻¹ region.

Table 3.8. Differences in selected peak positions in Figure 3.26.

<i>Regions</i>	Computational (Lanl2dz)	Experimental	Difference
<i>Nickel-Phosphorous Modes & Metal-Carbonyl Bending</i>	538 cm ⁻¹	541 cm ⁻¹	+ 3 cm ⁻¹
	510 cm ⁻¹	531 cm ⁻¹	+ 21 cm ⁻¹
	495 cm ⁻¹	522 cm ⁻¹	10 cm ⁻¹
	435 cm ⁻¹	427 cm ⁻¹	+ 8 cm ⁻¹
	418 cm ⁻¹	-	-
	392 cm ⁻¹	401 cm ⁻¹	- 9 cm ⁻¹
	375 cm ⁻¹	371 cm ⁻¹	- 4 cm ⁻¹
	<i>Average difference (Absolute)</i>		9 cm ⁻¹
<i>PPh₃ Modes</i>	694 cm ⁻¹	691 cm ⁻¹	+ 3 cm ⁻¹
	<i>Average difference (Absolute)</i>		3 cm ⁻¹

In the first region of KBr windows (800-300 cm⁻¹), similar to the second region of TPX windows, different modes of nickel-phosphorous, metal-carbonyl bending and PPh₃ takes place.(Figure 3.27.) There are some differences in the spectra of KBr and TPX windows. The band at 418 cm⁻¹ of computational [Ni₂Ge₉(PPh₃)₂]²⁻ spectrum appears as a shoulder at 415 cm⁻¹ in the experimental data of the same cluster, which was not that obvious in the measurements with TPX windows. Bands at 343 cm⁻¹ and 317 cm⁻¹ of both clusters' experimental data are clearly observed now and correlated to the [Ni₆Ge₁₃(CO)₅]⁴⁻ band at 347 cm⁻¹ (metal-carbonyl bending) and [Ni₂Ge₉(PPh₃)₂]²⁻ band at 311 cm⁻¹ (nickel-nickel stretching) of the computational spectra. As in the case of TPX windows, there is a no transmission between 700 cm⁻¹ and 750 cm⁻¹. Therefore, the band pairs of PPh₃ modes at 756 cm⁻¹ and 694 cm⁻¹ could not be identified in the experimental results. The differences between the computational and experimentally determined bands are listed in Table 3.9.

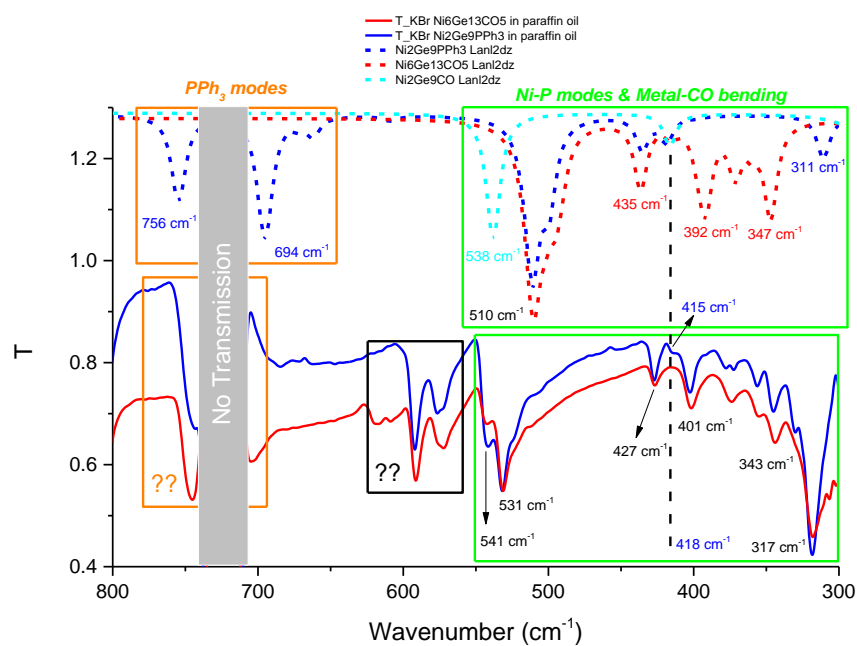


Figure 3.27. Experimental FTIR spectra of $[\text{Ni}_2\text{Ge}_9(\text{PPh}_3)]^{2-}$ (blue) and $[\text{Ni}_6\text{Ge}_{13}(\text{CO})_5]^{4-}$ (red) as solid lines with KBr windows; and computational IR spectra of $[\text{Ni}_2\text{Ge}_9(\text{PPh}_3)]^{2-}$ (blue), $[\text{Ni}_6\text{Ge}_{13}(\text{CO})_5]^{4-}$ (red) and $[\text{Ni}_2\text{Ge}_9(\text{CO})]^{2-}$ (cyan) as dash lines with Lanl2dz in 800-300 cm⁻¹ region.

Table 3.9. Differences in selected peak positions in Figure 3.27.

<i>Regions</i>	Computational (Lanl2dz)	Experimental	Difference
<i>Nickel-Phosphorous & Metal-Carbonyl Bending</i>	538 cm ⁻¹	541 cm ⁻¹	+ 3 cm ⁻¹
	510 cm ⁻¹	531 cm ⁻¹	+ 21 cm ⁻¹
	435 cm ⁻¹	427 cm ⁻¹	+ 8 cm ⁻¹
	418 cm ⁻¹	415 cm ⁻¹	+ 3 cm ⁻¹
	392 cm ⁻¹	401 cm ⁻¹	- 9 cm ⁻¹
	347 cm ⁻¹	343 cm ⁻¹	+ 4 cm ⁻¹
	311 cm ⁻¹	317 cm ⁻¹	- 6 cm ⁻¹
	<i>Average difference (Absolute)</i>		

In the second region of KBr windows (1350-800 cm⁻¹), different modes of PPh₃ is present in both clusters' (at 1302 cm⁻¹, 1173 cm⁻¹, 1100 cm⁻¹ and 928 cm⁻¹) and PPh₃ containing precursors' experimental data as well as four computational bands of [Ni₂Ge₉(PPh₃)²⁻ at 1288 cm⁻¹, 1173 cm⁻¹, 1062 cm⁻¹ and 998 cm⁻¹.(Figure 3.28.) Observing PPh₃ related vibrational modes in the experimental spectrum of [Ni₆Ge₁₃(CO)₅]⁴⁻, once again supports the co-crystal formation during the synthesis of both clusters. The relative peak positions of experimental and computational results were not compared in a table as previous regions. The bands could not be paired in a reliable way due to the complexity of the spectrum.

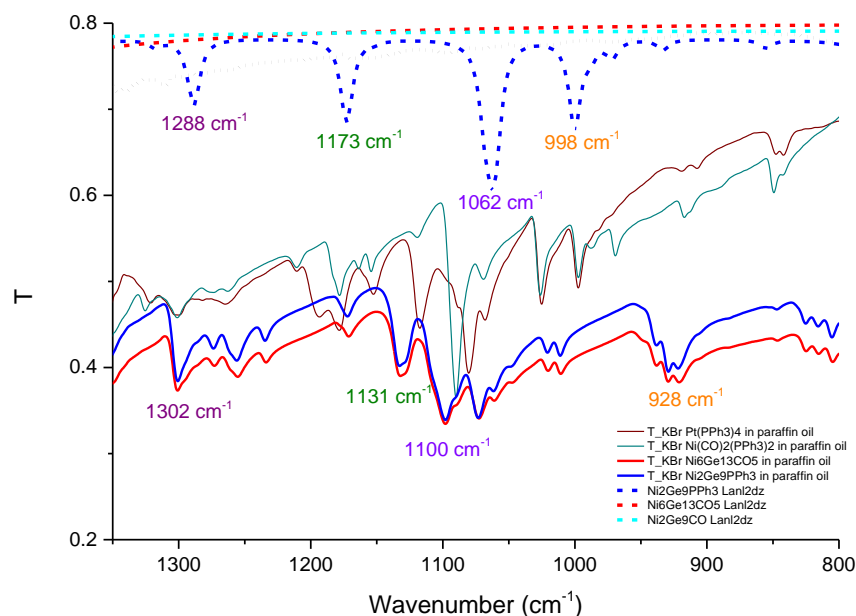


Figure 3.28. Experimental FTIR spectra of K_4Ge_9 (grey), $\text{Pt}(\text{PPh}_3)_4$ (wine), $\text{Ni}(\text{CO})_2(\text{PPh}_3)_2$ (dark cyan) as thin solid lines, $[\text{Ni}_2\text{Ge}_9(\text{PPh}_3)]^{2-}$ (blue) and $[\text{Ni}_6\text{Ge}_{13}(\text{CO})_5]^{4-}$ (red) as solid lines with KBr windows; and computational IR spectra of $[\text{Ni}_2\text{Ge}_9(\text{PPh}_3)]^{2-}$ (blue), $[\text{Ni}_6\text{Ge}_{13}(\text{CO})_5]^{4-}$ (red) and $[\text{Ni}_2\text{Ge}_9(\text{CO})]^{2-}$ (cyan) as dash lines with Lanl2dz in 1350-800 cm^{-1} region.

In the third region of KBr and TPX windows (2100-1500 cm^{-1}), carbonyl stretching bands are present in both clusters' experimental and computational data. (Figure 3.29.) There are 4 individual bands in computational spectrum of $[\text{Ni}_6\text{Ge}_{13}(\text{CO})_5]^{4-}$ resulting from 5 different carbonyl groups. For the terminal carbonyls, the maximum intensity is observed at 1762 cm^{-1} , which is at the same position of the carbonyl stretching of $[\text{Ni}_2\text{Ge}_9(\text{CO})]^{2-}$ in computational calculations. The bridging carbonyl stretching of $[\text{Ni}_6\text{Ge}_{13}(\text{CO})_5]^{4-}$ occurs at 1620 cm^{-1} in the computational spectrum. One of the modes of PPh_3 in the $[\text{Ni}_2\text{Ge}_9(\text{PPh}_3)]^{2-}$ is located at 1566 cm^{-1} . The shoulder that is observed at 1874 cm^{-1} of $[\text{Ni}_6\text{Ge}_{13}(\text{CO})_5]^{4-}$ experimental spectrum but

not clearly observed in the spectrum of the other is considered to be the bridging carbonyl stretching. Moreover, $[\text{Ni}_2\text{Ge}_9(\text{PPh}_3)]^{2-}$ spectrum has a sharper carbonyl band at 1929 cm^{-1} than the one in $[\text{Ni}_6\text{Ge}_{13}(\text{CO})_5]^{4-}$ spectrum. This might be due to the higher ratio of $[\text{Ni}_2\text{Ge}_9(\text{CO})]^{2-}$ cluster formation. Whereas, at 1932 cm^{-1} , $[\text{Ni}_6\text{Ge}_{13}(\text{CO})_5]^{4-}$ has a broader band since 4 terminal carbonyl groups present in its structure exhibits a combination of bands.

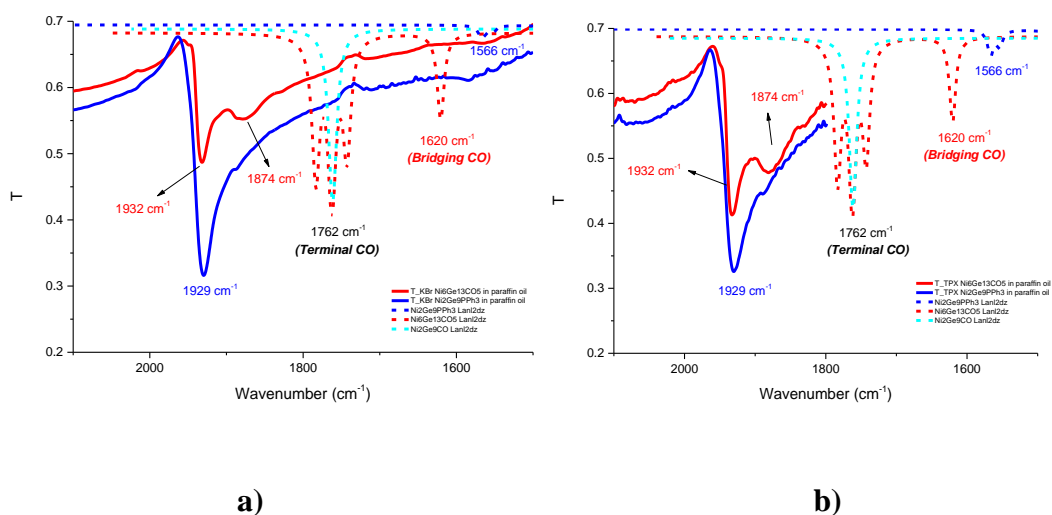


Figure 3.29. Experimental FTIR spectra of $[\text{Ni}_2\text{Ge}_9(\text{PPh}_3)]^{2-}$ (blue) and $[\text{Ni}_6\text{Ge}_{13}(\text{CO})_5]^{4-}$ (red) as solid lines with **a)** KBr windows **b)** TPX windows; and computational IR spectra of $[\text{Ni}_2\text{Ge}_9(\text{PPh}_3)]^{2-}$ (blue), $[\text{Ni}_6\text{Ge}_{13}(\text{CO})_5]^{4-}$ (red) and $[\text{Ni}_2\text{Ge}_9(\text{CO})]^{2-}$ (cyan) as dash lines with Lanl2dz in $2100\text{-}1500\text{ cm}^{-1}$ region.

3.4.3.2. Basis Set: CEP-121g

As observed in the computational spectrum with the Lanl2dz basis set, there are four main groups of bands in the region of 1750-20 cm^{-1} (metal-metal, nickel-phosphorous, PPh_3 modes) for $[\text{Ni}_2\text{Ge}_9(\text{PPh}_3)]^{2-}$ cluster.(Figure 3.30.) No band is observed between 2600 cm^{-1} and 1750 cm^{-1} as expected. In the metal-metal region (315-20 cm^{-1}), the nickel-nickel stretching takes place at 315 cm^{-1} , which is slightly different from the Lanl2dz calculations (310 cm^{-1}). In the nickel-phosphorous region (506-410 cm^{-1}), nickel-phosphorous stretching is present at 506 cm^{-1} , whereas it was 510 cm^{-1} in Lanl2dz calculations. Similar to the previous case various modes of triphenylphosphine occur between 1565 cm^{-1} and 610 cm^{-1} .

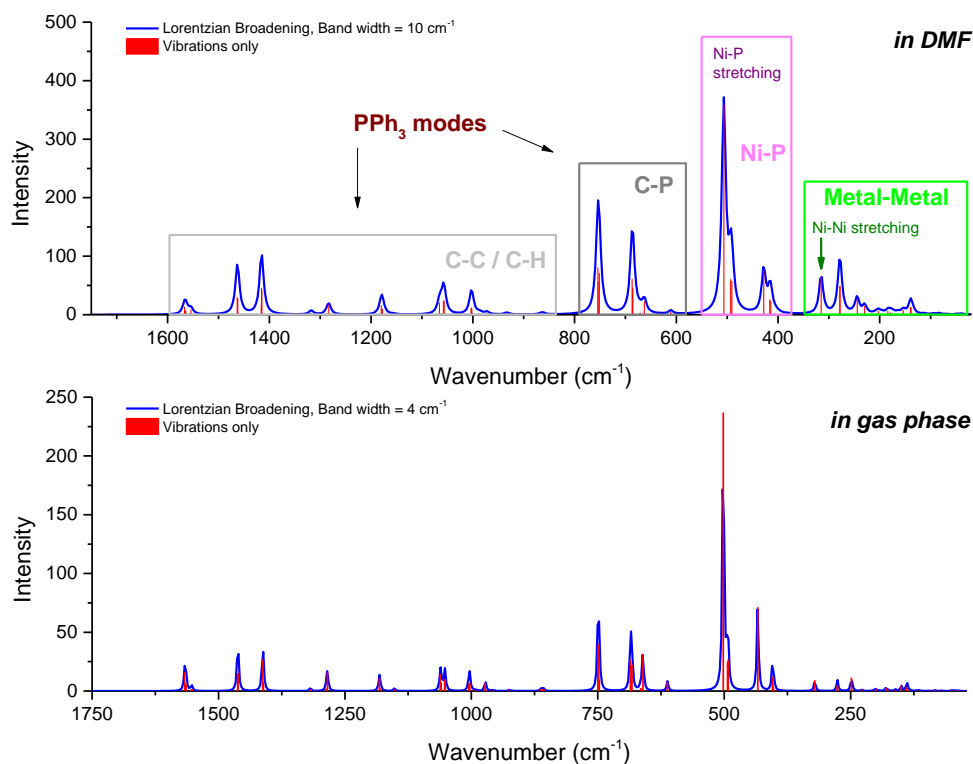


Figure 3.30. Computational IR spectra of $[\text{Ni}_2\text{Ge}_9(\text{PPh}_3)]^{2-}$ in DMF and gas phase with CEP-121g in $1750\text{-}20\text{ cm}^{-1}$ region.

Four groups of bands (metal-metal modes, nickel-carbon stretching, metal-carbonyl bending and carbonyl stretching) is also observed for $[\text{Ni}_2\text{Ge}_9(\text{CO})]^{2-}$ cluster similar to the calculation with Lanl2dz. The carbonyl stretching has as a sharp band at 1757 cm^{-1} , which was at 1761 cm^{-1} for the case of Lanl2dz.(Figure 3.31.) In the metal-metal region ($296\text{-}20\text{ cm}^{-1}$), nickel-nickel stretching is at 295 cm^{-1} , which is different from the Lanl2dz case (272 cm^{-1}). Nickel-carbon stretching and metal-carbonyl bending are located at 531 cm^{-1} and 390 cm^{-1} , respectively, again slightly red shifted compared to the Lanl2dz calculations (538 cm^{-1} and 410 cm^{-1}). The nickel-carbon stretching at 531 cm^{-1} of the cluster is in the region where gallium-carbon and aluminum-carbon stretching modes takes place ($680\text{-}332\text{ cm}^{-1}$).^{110,113}

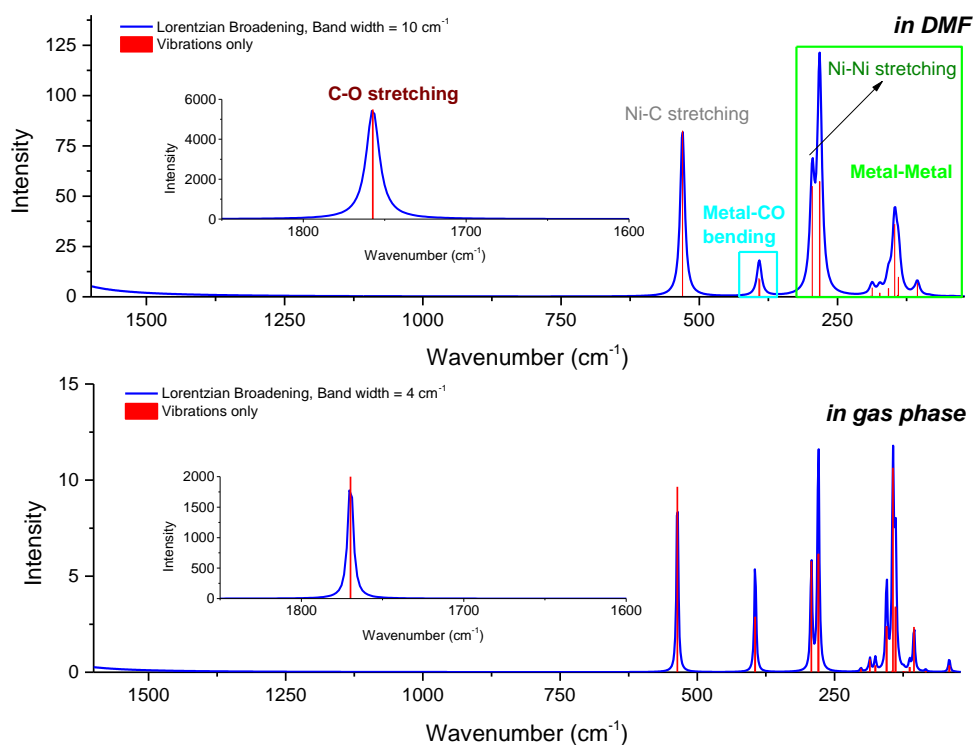


Figure 3.31. Computational IR spectra of $[\text{Ni}_2\text{Ge}_9(\text{CO})]^{2-}$ in DMF and gas phase with CEP-121g in $1850\text{-}1600\text{ cm}^{-1}$ and $1625\text{-}20\text{ cm}^{-1}$ regions.

In the computed spectrum of $[\text{Ni}_6\text{Ge}_{13}(\text{CO})_5]^{4-}$, there are three groups of bands (metal-metal, metal-carbonyl bending and carbonyl stretching modes) as in the spectrum obtained with Lanl2dz calculations. (Figure 3.32.) In metal-metal region ($270\text{-}20\text{ cm}^{-1}$), the nickel-nickel stretching band of the two interstitial nickel atoms is present at 270 cm^{-1} (Lanl2dz: 258 cm^{-1}). Metal-carbonyl bending modes are present in between 538 cm^{-1} and 345 cm^{-1} (Lanl2dz: 510 cm^{-1} and 347 cm^{-1}), which is also the region where nickel-phosphorous modes occur in $[\text{Ni}_2\text{Ge}_9(\text{PPh}_3)]^{2-}$. Carbonyl stretching bands are 1745 cm^{-1} , 1723 cm^{-1} , 1712 cm^{-1} , 1707 cm^{-1} for terminal carbonyls and 1565 cm^{-1} for the bridging one compared to the Lanl2dz case (1783 cm^{-1} , 1762 cm^{-1} , 1747 cm^{-1} , 1742 cm^{-1} and 1620 cm^{-1} , respectively). As in Lanl2dz

calculations, Gaussian calculated the vibrational spectrum of the clusters with C_1 symmetry so all carbonyl groups show separate bands.

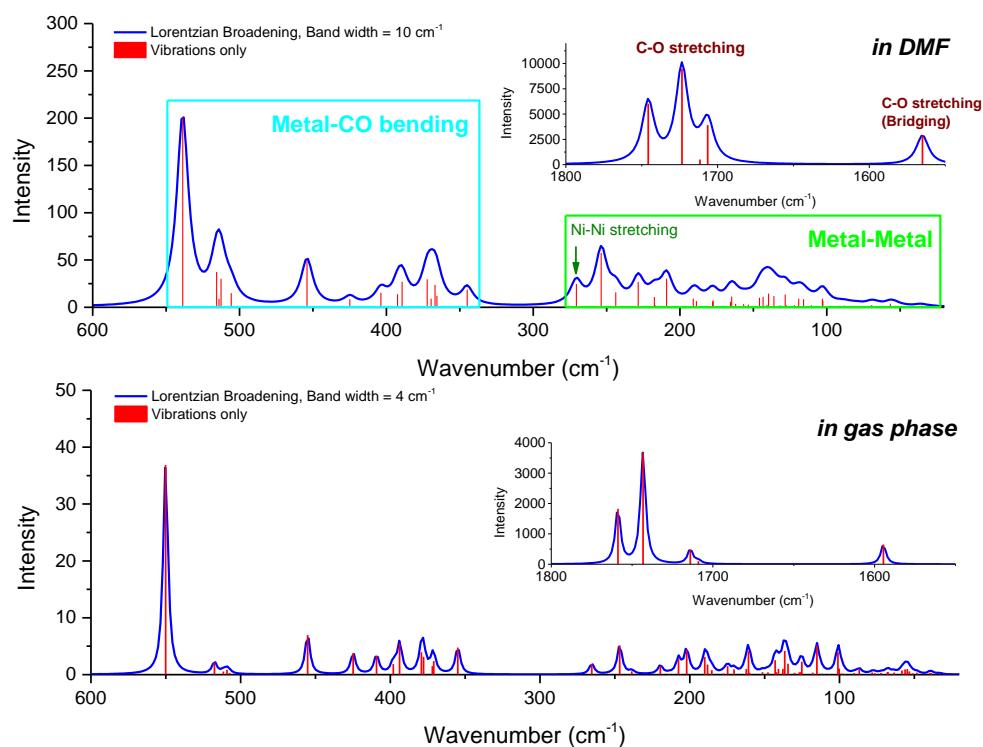


Figure 3.32. Computational IR spectra of $[\text{Ni}_6\text{Ge}_{13}(\text{CO})_5]^{4-}$ in DMF and gas phase with CEP-121g in 1800-1550 cm^{-1} and 600-20 cm^{-1} regions.

3.4.3.2.1. Comparison of CEP-121g Calculations with Experimental Results

As Lan12dz comparison in *Section 3.4.3.1.1*, the spectra are divided into regions to analyze the bands in detail.(Table 3.6.) Similar bands or group of bands are shown with the same colored rectangles.

In the metal-metal region of TPX windows, the combination of frequency calculations of three clusters ($[\text{Ni}_2\text{Ge}_9(\text{PPh}_3)]^{2-}$, $[\text{Ni}_6\text{Ge}_{13}(\text{CO})_5]^{4-}$, $[\text{Ni}_2\text{Ge}_9(\text{CO})]^{2-}$) revealed similar bands with the experimental data as three groups of bands (grey, green and black rectangles). As mentioned in Lanl2dz discussions, this actually strengthens the idea of having co-crystals in the same solution.(Figure 3.33.) The nickel-nickel stretching bands are located in the computational spectra at 310 cm^{-1} , 258 cm^{-1} , 295 cm^{-1} for ($[\text{Ni}_2\text{Ge}_9(\text{PPh}_3)]^{2-}$, $[\text{Ni}_6\text{Ge}_{13}(\text{CO})_5]^{4-}$, $[\text{Ni}_2\text{Ge}_9(\text{CO})]^{2-}$) clusters, respectively. Thus, the band observed in the experimental spectra of the clusters at 292 cm^{-1} is considered to be the nickel-nickel stretching band. The rest of the bands are similarly assigned as in the case of Lanl2dz. The relative peak differences in the computational and experimental spectra are shown in Table 3.10. The average of differences is 15 cm^{-1} for this region which is lower than Lanl2dz one.

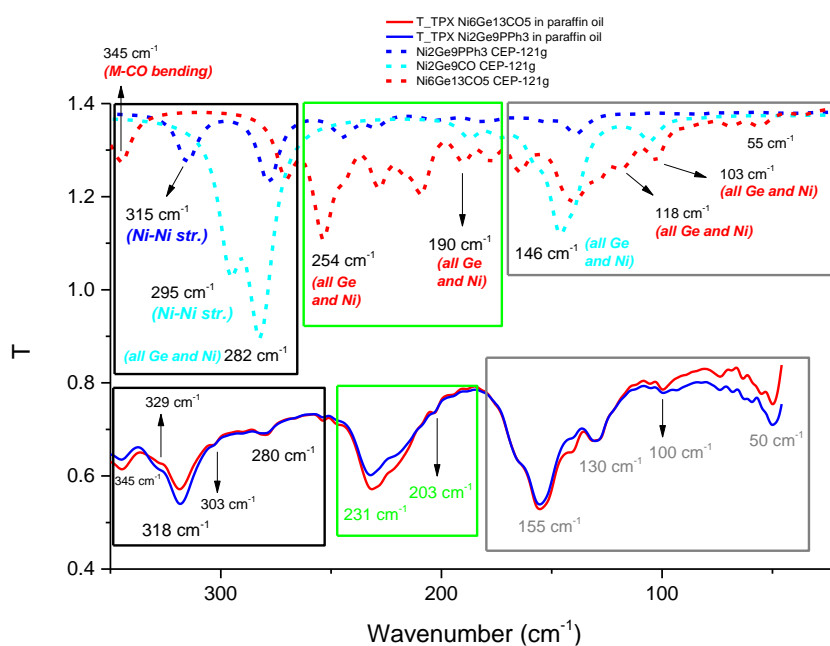


Figure 3.33. Experimental FTIR spectra of $[\text{Ni}_2\text{Ge}_9(\text{PPh}_3)]^{2-}$ (blue) and $[\text{Ni}_6\text{Ge}_{13}(\text{CO})_5]^{4-}$ (red) as solid lines with TPX windows; and computational IR spectra of $[\text{Ni}_2\text{Ge}_9(\text{PPh}_3)]^{2-}$ (blue), $[\text{Ni}_6\text{Ge}_{13}(\text{CO})_5]^{4-}$ (red) and $[\text{Ni}_2\text{Ge}_9(\text{CO})]^{2-}$ (cyan) as dash lines with CEP-121g in 350-20 cm⁻¹ region.

Table 3.10. Differences in selected peak positions in Figure 3.33.

<i>Regions</i>	Computational (CEP-121g)	Experimental	Difference
<i>Metal-Metal</i>	55 cm ⁻¹	50 cm ⁻¹	+ 5 cm ⁻¹
	103 cm ⁻¹	100 cm ⁻¹	+ 3 cm ⁻¹
	118 cm ⁻¹	130 cm ⁻¹	- 12 cm ⁻¹
	146 cm ⁻¹	155 cm ⁻¹	- 9 cm ⁻¹
	190 cm ⁻¹	203 cm ⁻¹	- 13 cm ⁻¹
	254 cm ⁻¹	231 cm ⁻¹	+ 23 cm ⁻¹
	282 cm ⁻¹	318 cm ⁻¹	- 36 cm ⁻¹
	295 cm ⁻¹	329 cm ⁻¹	- 34 cm ⁻¹
	345 cm ⁻¹	345 cm ⁻¹	0 cm ⁻¹
	<i>Average difference (Absolute)</i>		

In the second region of TPX windows (700-350 cm⁻¹), green rectangle represents different modes of nickel-phosphorous and metal-carbonyl bending based on the computational results.(Figure 3.34.) Nickel-phosphorous stretching in [Ni₂Ge₉(PPh₃)₂]²⁻ is present at 506 cm⁻¹, where one of the carbonyl bending modes of [Ni₆Ge₁₃(CO)₅]⁴⁻ also takes place. Other metal-carbonyl bending modes of CO-containing clusters occur between 538 cm⁻¹ and 345 cm⁻¹ in the computational results. Metal-carbonyl bending of [Ni₆Ge₁₃(CO)₅]⁴⁻ at 538 cm⁻¹ and nickel-phosphorous stretching band of [Ni₂Ge₉(PPh₃)₂]²⁻ at 506 cm⁻¹ resembles to each other as Lan12dz calculations. However, there is a difference in their peak positions which actually better correlates with the broad band of clusters in their FTIR spectra from 531 cm⁻¹ to 460 cm⁻¹. That broad band with a maximum of 531 cm⁻¹ is probably a combination of the computed cluster bands in various amounts from 538 cm⁻¹ to 454 cm⁻¹. The other computed bands of [Ni₂Ge₉(PPh₃)₂]²⁻ and [Ni₆Ge₁₃(CO)₅]⁴⁻ at 428 cm⁻¹

¹, 391 cm⁻¹ and 369 cm⁻¹ are similar to the bands of experimental bands of the clusters at 427 cm⁻¹, 401 cm⁻¹ and 375 cm⁻¹. As Lanl2dz calculations, the group of bands in black rectangle could not be paired with any of the bands in the computational results. In the orange rectangle at 690 cm⁻¹, there are sharp bands of computational [Ni₂Ge₉(PPh₃)²⁻ and PPh₃ containing precursors Pt(PPh₃)₄, Ni(CO)₂(PPh₃)₂, which was not identified in the experimental spectra possibly due to the blue shift beyond 700 cm⁻¹. The differences in selected peak positions are shown in Table 3.11, where average values are 5 cm⁻¹ and 7 cm⁻¹ for Ni-P and M-CO bending modes, and PPh₃ modes, respectively.

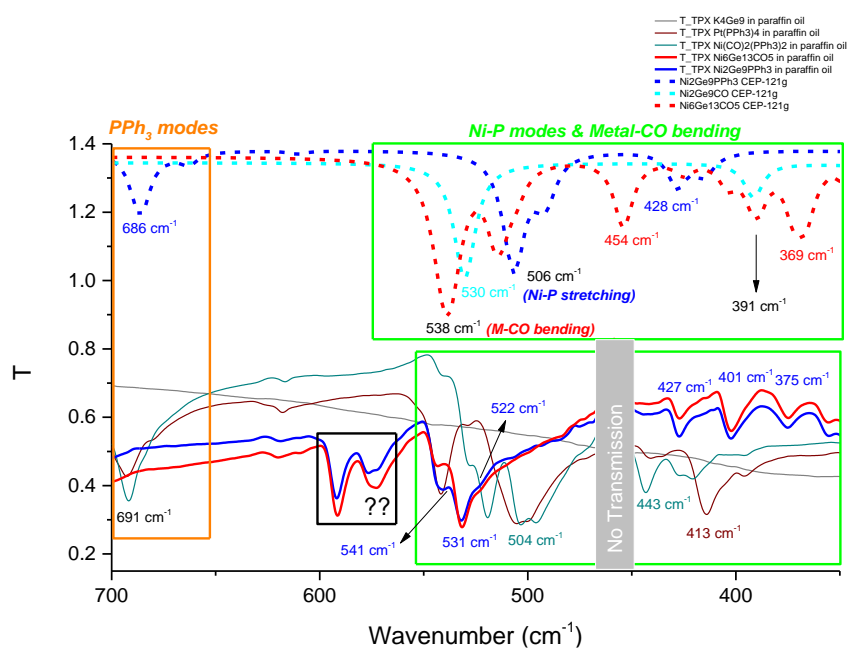


Figure 3.34. Experimental FTIR spectra of K_4Ge_9 (grey), $Pt(PPh_3)_4$ (wine), $Ni(CO)_2(PPh_3)_2$ (dark cyan) as thin solid lines, $[Ni_2Ge_9(PPh_3)]^{2-}$ (blue) and $[Ni_6Ge_{13}(CO)_5]^{4-}$ (red) as solid lines with TPX windows; and computational IR spectra of $[Ni_2Ge_9(PPh_3)]^{2-}$ (blue), $[Ni_6Ge_{13}(CO)_5]^{4-}$ (red) and $[Ni_2Ge_9(CO)]^{2-}$ (cyan) as dash lines with CEP-121g in 700-350 cm^{-1} region.

Table 3.11. Differences in selected peak positions in Figure 3.34.

<i>Regions</i>	Computational (CEP-121g)	Experimental	Difference
<i>Nickel-Phosphorous Modes & Metal-Carbonyl Bending</i>	538 cm ⁻¹	531 cm ⁻¹	+ 7 cm ⁻¹
	506 cm ⁻¹	522 cm ⁻¹	- 16 cm ⁻¹
	454 cm ⁻¹	-	-
	428 cm ⁻¹	427 cm ⁻¹	+ 1 cm ⁻¹
	391 cm ⁻¹	401 cm ⁻¹	- 10 cm ⁻¹
	369 cm ⁻¹	371 cm ⁻¹	- 2 cm ⁻¹
	<i>Average difference (Absolute)</i>		7 cm ⁻¹
<i>PPh₃ Modes</i>	686 cm ⁻¹	691 cm ⁻¹	- 5 cm ⁻¹
	<i>Average difference (Absolute)</i>		5 cm ⁻¹

In the first region of KBr windows (800-300 cm⁻¹), different modes of nickel-phosphorous, metal-carbonyl bending and PPh₃ takes place.(Figure 3.35.) There are some differences in the spectra of KBr and TPX windows. Bands at 343 cm⁻¹ and 318 cm⁻¹ of both clusters' experimental data are similar to the ones of computational [Ni₆Ge₁₃(CO)₅]⁴⁻ band at 345 cm⁻¹ (metal-carbonyl bending) and [Ni₂Ge₉(PPh₃)]²⁻ band at 315 cm⁻¹ (nickel-nickel stretching). Similarly, bands at 426 cm⁻¹ and 402 cm⁻¹ of experimental results resembles to 454 cm⁻¹ and 368 cm⁻¹ of [Ni₆Ge₁₃(CO)₅]⁴⁻ computational data. As Lanl2dz calculations, the band pairs of PPh₃ modes at 753 cm⁻¹ and 686 cm⁻¹ could not be identified in the experimental results. Table 3.12 lists the selected bands of computational and experimental results with an average value of 15 cm⁻¹. In this region, Lanl2dz calculations resemble to the experimental ones more.

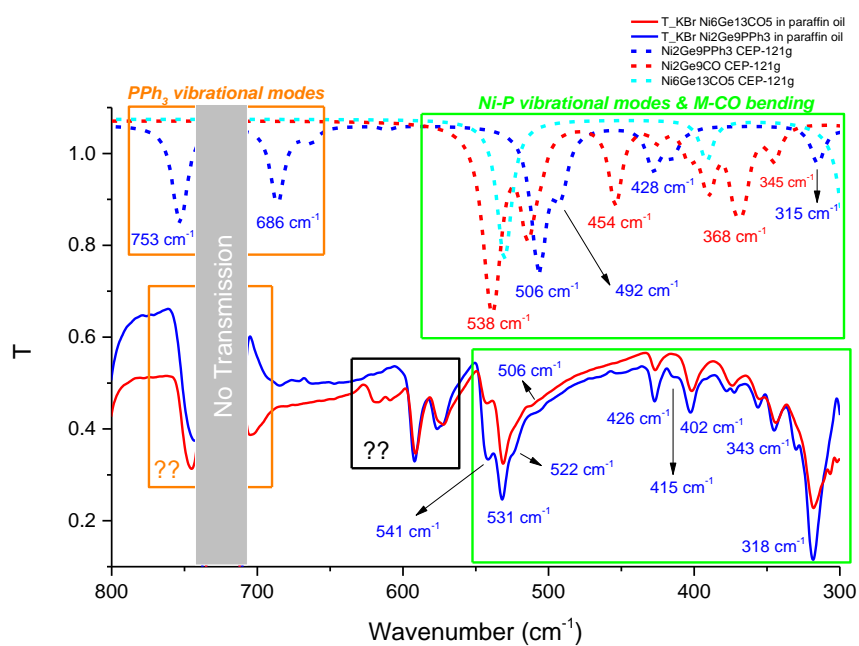


Figure 3.35. Experimental FTIR spectra of $[\text{Ni}_2\text{Ge}_9(\text{PPh}_3)]^{2-}$ (blue) and $[\text{Ni}_6\text{Ge}_{13}(\text{CO})_5]^{4-}$ (red) as solid lines with KBr windows; and computational IR spectra of $[\text{Ni}_2\text{Ge}_9(\text{PPh}_3)]^{2-}$ (blue), $[\text{Ni}_6\text{Ge}_{13}(\text{CO})_5]^{4-}$ (red) and $[\text{Ni}_2\text{Ge}_9(\text{CO})]^{2-}$ (cyan) as dash lines with CEP-121g in 800-300 cm⁻¹ region.

Table 3.12. Differences in selected peak positions in Figure 3.35.

<i>Regions</i>	Computational (CEP-121g)	Experimental	Difference
<i>Nickel-Phosphorous & Metal-Carbonyl Bending</i>	538 cm ⁻¹	531 cm ⁻¹	+ 7 cm ⁻¹
	506 cm ⁻¹	522 cm ⁻¹	- 16 cm ⁻¹
	492 cm ⁻¹	506 cm ⁻¹	- 14 cm ⁻¹
	454 cm ⁻¹	426 cm ⁻¹	+ 28 cm ⁻¹
	428 cm ⁻¹	415 cm ⁻¹	+ 13 cm ⁻¹
	368 cm ⁻¹	402 cm ⁻¹	- 34 cm ⁻¹
	345 cm ⁻¹	343 cm ⁻¹	+ 2 cm ⁻¹
	315 cm ⁻¹	317 cm ⁻¹	- 3 cm ⁻¹
	<i>Average difference (Absolute)</i>		

In the second region of KBr windows (1350-800 cm⁻¹), different modes of PPh₃ are present in both clusters' (at 1302 cm⁻¹, 1173 cm⁻¹, 1100 cm⁻¹ and 928 cm⁻¹) and PPh₃ containing precursors' experimental data as well as four computational bands of [Ni₂Ge₉(PPh₃)]²⁻ at 1284 cm⁻¹, 1178 cm⁻¹, 1058 cm⁻¹ and 1002 cm⁻¹.(Figure 3.36.) Observing PPh₃ related vibrational modes in the experimental spectrum of [Ni₆Ge₁₃(CO)₅]⁴⁻, supports the co-crystal formation during the synthesis of both clusters one more time. As Lan12dz calculations, the relative peak positions of experimental and computational results were not compared in a table as previous regions.

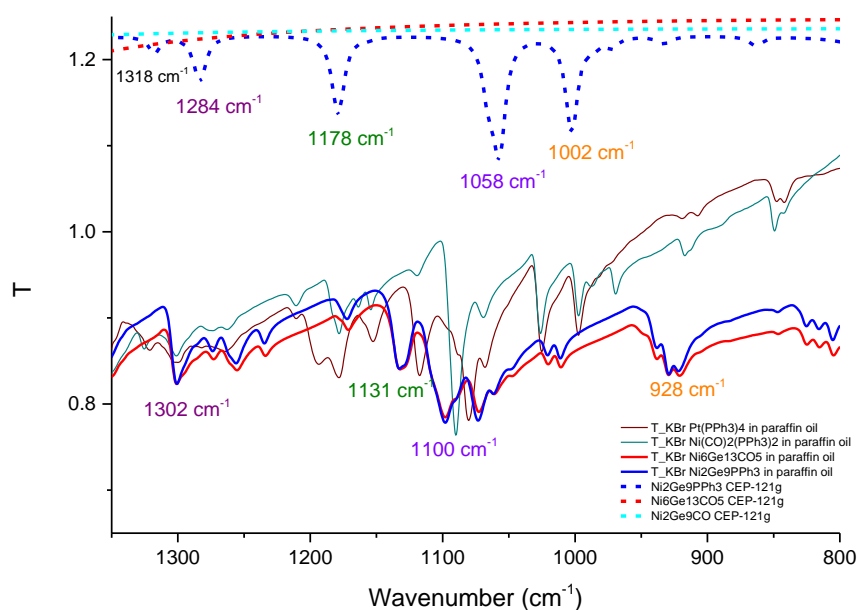


Figure 3.36. Experimental FTIR spectra of K_4Ge_9 (grey), $Pt(PPh_3)_4$ (wine), $Ni(CO)_2(PPh_3)_2$ (dark cyan) as thin solid lines, $[Ni_2Ge_9(PPh_3)]^{2-}$ (blue) and $[Ni_6Ge_{13}(CO)_5]^{4-}$ (red) as solid lines with KBr windows; and computational IR spectra of $[Ni_2Ge_9(PPh_3)]^{2-}$ (blue), $[Ni_6Ge_{13}(CO)_5]^{4-}$ (red) and $[Ni_2Ge_9(CO)]^{2-}$ (cyan) as dash lines with CEP-121g in 1350-800 cm^{-1} region.

In the third region of KBr and TPX windows (2100-1500 cm^{-1}), carbonyl stretching bands are present in both clusters' experimental data and all computational data.(Figure 3.37.) There are four carbonyl bands in computational spectrum of $[Ni_6Ge_{13}(CO)_5]^{4-}$ resulting from five different vibrations.(Figure 3.32.) For the terminal carbonyls, the maximum intensity is observed at 1724 cm^{-1} ; however, the carbonyl stretching of $[Ni_2Ge_9(CO)]^{2-}$ has shifted to 1757 cm^{-1} which is different from the Lanl2dz results.(Figure 3.24) Both bridging carbonyl stretching of

computational $[\text{Ni}_6\text{Ge}_{13}(\text{CO})_5]^{4-}$ and one of the modes of PPh_3 in the $[\text{Ni}_2\text{Ge}_9(\text{PPh}_3)]^{2-}$ occur at 1564 cm^{-1} .

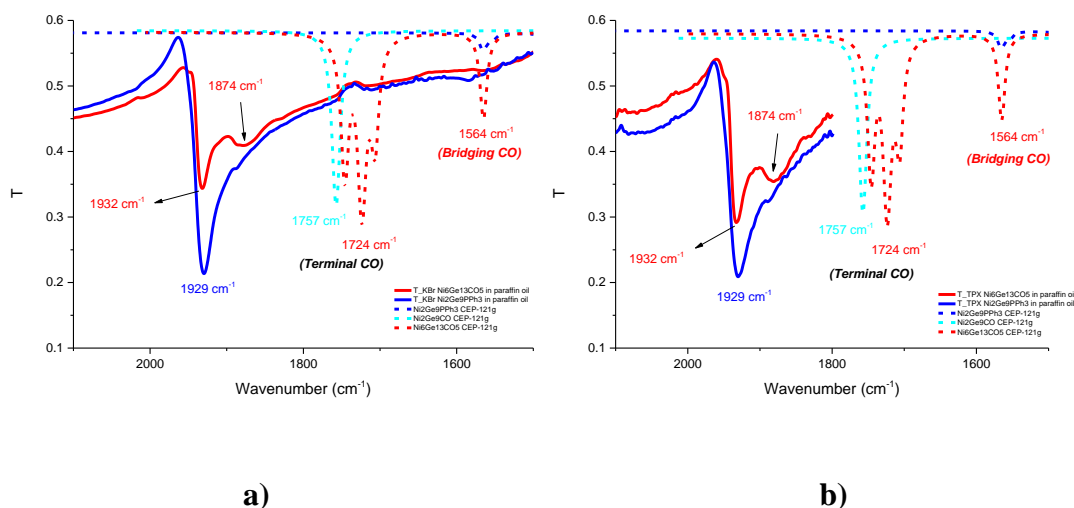


Figure 3.37. Experimental FTIR spectra of $[\text{Ni}_2\text{Ge}_9(\text{PPh}_3)]^{2-}$ (blue) and $[\text{Ni}_6\text{Ge}_{13}(\text{CO})_5]^{4-}$ (red) as solid lines with a) KBr windows b) TPX windows; and computational IR spectra of $[\text{Ni}_2\text{Ge}_9(\text{PPh}_3)]^{2-}$ (blue), $[\text{Ni}_6\text{Ge}_{13}(\text{CO})_5]^{4-}$ (red) and $[\text{Ni}_2\text{Ge}_9(\text{CO})]^{2-}$ (cyan) as dash lines with CEP-121g in $2100\text{-}1500\text{ cm}^{-1}$ region.

3.4.4. Fluorescence Spectrometry Analyses

The potential fluorescent activities of both clusters are investigated in DMF solutions by screening various excitation wavelengths. Due to the low intensity of the cluster bands and strong interference from the solvent, the excitation and emission slit widths are chosen as 2.5 nm and 10 nm for clusters, respectively. On the other hand, in all background measurements of DMF, excitation and emission slit widths are chosen as 1.5 nm and 2.5 nm due to comparably stronger emissions.

A search for excitation wavelengths of $[\text{Ni}_2\text{Ge}_9(\text{PPh}_3)]^{2-}$ clusters revealed a band at 260 nm, which is the maximum absorption in UV-Vis spectra, and a broad band centered around 320 nm.(Figure 3.38.) Excitation of the sample at these wavelengths results a fairly strong emission band at ca. 400 nm (s). The observed feature at 780 nm with 260 nm excitation is most probably the third-order diffraction of the 260 nm excitation. A check for background emission with only DMF at the same excitation wavelengths revealed that pure DMF also emits strongly close to the cluster bands; at 320 nm (w) and 383 nm (s) with excitation at 260 nm, and 354 nm (sh), 374 nm (s), and 700 nm (w, broad) with excitation at 320 nm. Although the spectrum of DMF may look similar to cluster one, there are some differences. The shape of the emission bands have no resemblance to the DMF ones but quite similar to the UV spectra of the clusters. Moreover, unlike DMF the center of the emission band of the cluster does not shift with a change in the excitation wavelength and have ca. 30 nm difference with the observed strongest band of DMF. In addition, the emission band of DMF observed at 320 nm with excitation of 260 nm and the shoulder observed at 354 nm are not present in the cluster data.(Figure 3.38.) The cluster spectrum has no observed broad emission centered ca. 700 nm.

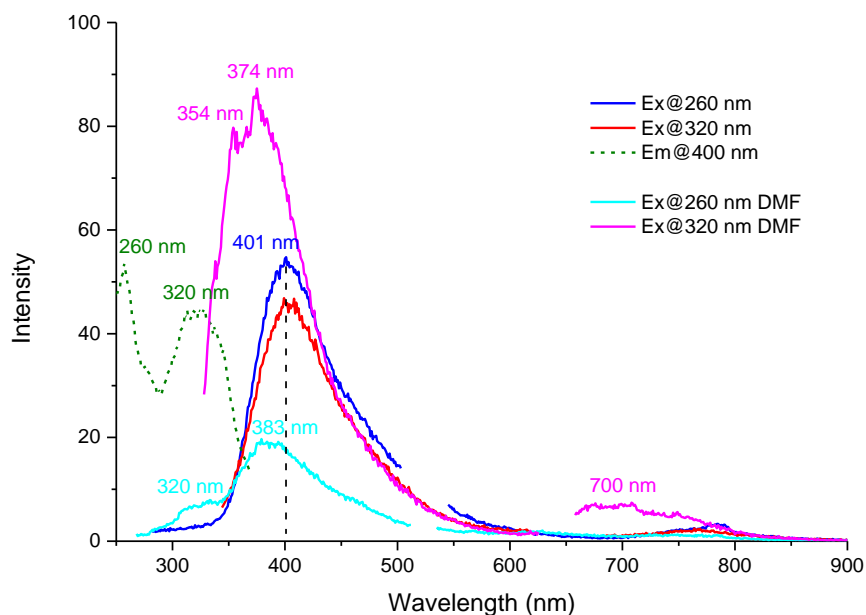


Figure 3.38. Fluorescence spectra of $[\text{Ni}_2\text{Ge}_9(\text{PPh}_3)]^{2-}$ in DMF and only DMF

The search of excitation wavelengths of $[\text{Ni}_6\text{Ge}_{13}(\text{CO})_5]^{4-}$ clusters revealed a strong band at 263 nm, which is also close to the maximum absorption, and a very broad band from ca. 300 nm to 450 nm. (Figure 3.39.) Therefore, the emissions of the cluster are investigated at 260 nm, 320 nm, 355 nm and 380 nm. Similarly, the excitation of the cluster at 260 nm and 320 nm has resulted a strong feature at ca. 410 nm. (Figure 3.39.) Excitation of the cluster at 355 nm and 380 nm yielded a similar band with a shifted center wavelength. The changes observed in the main emission band is possibly due to the lower energies of the excitation wavelengths that does not provide enough energy to access to the higher energy states of the cluster. As seen in the TD studies of the cluster, simulation of the UV spectrum requires more than 750 transitions, thus access to higher energy states of the cluster. Similar differences are observed between the DMF and cluster spectra.

It should also be noted that there is a possibility of observing fluorescent spectra of the clusters as hindered DMF emissions. This is most likely due to strong absorptions of cluster molecules at higher energies compared to the lower energies (see UV-vis spectra). Unfortunately, there is no other solvent available for further investigation.

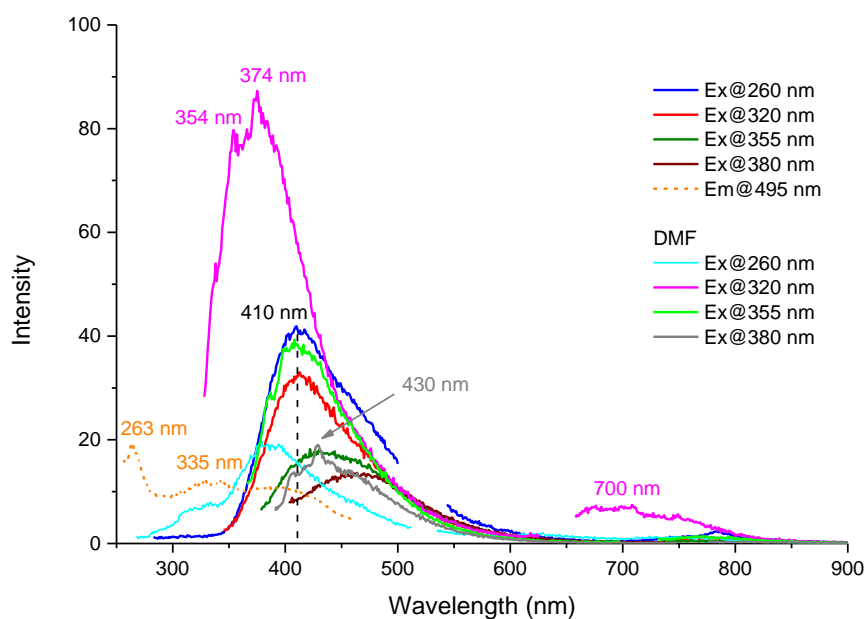


Figure 3.39. Fluorescence spectra of $[\text{Ni}_6\text{Ge}_{13}(\text{CO})_5]^{4+}$ in DMF and only DMF

CHAPTER 4

CONCLUSIONS

The quest for discovering new clusters with well-known properties and using them as elementary units for nanomaterials has become great interest in cluster science. Zintl ion clusters serve the possibility of being seeds to larger clusters and “artificial atoms” in cluster assembled materials. This possibility urges to investigate properties of these clusters thoroughly for making properly designed materials with predictable properties for advanced material applications.

In this study, two nickel integrated germanium Zintl ion clusters were synthesized and investigation of spectroscopic properties, which have never been investigated for these types of clusters, was performed. $[\text{Ni}_2\text{Ge}_9(\text{PPh}_3)]^{2-}$ and $[\text{Ni}_6\text{Ge}_{13}(\text{CO})_5]^{4-}$ were synthesized under inert atmosphere at different temperatures with the same starting materials and solvent choice. After proper treatment of the cluster crystals, cluster solutions or mixtures were included in measurements of UV-Vis, FTIR and Fluorescence spectroscopy to validate their vibrational and optical properties. Since there is not enough information available of spectroscopic properties for these types of clusters, a computational study (Optimization, Frequency and TD) was also performed to evaluate experimental results in FTIR and UV-Vis spectroscopy. The calculations were done under the influence of DMF solvent in order to create a similar environment to the experimental conditions, in addition to the gas phase calculations. The difference between Lanl2dz and CEP-121g basis sets were aimed to be determined based on their similarities to the experimental results.

After optimizations of both clusters, relative bond lengths and angles of optimized and crystal structures were compared with both basis sets. CEP-121g results revealed more similar values to the original structure in both cluster calculations. In addition, MO diagrams of both clusters were constructed by using the optimization outputs of the Lanl2dz and CEP-121g calculations. According to the HOMO-LUMO band gaps of the diagrams, $[\text{Ni}_2\text{Ge}_9(\text{PPh}_3)]^{2-}$ cluster might be a semi-conductor since it has band gap of ca. 1.12 eV. On the other hand, with a band gap lower than 0.06 eV, $[\text{Ni}_6\text{Ge}_{13}(\text{CO})_5]^{4-}$ cluster may find applications in optics and solar cells as detectors, solar energy collectors and optical filters in future.

In UV-Vis spectroscopy, cluster spectra are slightly different from each other that $[\text{Ni}_6\text{Ge}_{13}(\text{CO})_5]^{4-}$ cluster had a shoulder ca. 330 nm, which is most probably due to its more complex structure with higher number of electronic transitions. TD calculations with up to 750 transitions could be performed due to memory restrictions in TR-Grid computers, and thus a complete TD spectrum could not be constructed for both clusters. For this reason, only qualitative information could be extracted from the spectra and comparison with experimental results. Similar to the UV-Vis spectrum of $[\text{Ni}_6\text{Ge}_{13}(\text{CO})_5]^{4-}$, a shoulder is again present at ca. 330 nm in both TD calculations. Both basis set calculations give similar results either one of them could be used for interpretation of experimental results. It is important to note that the wide range of absorptions of clusters from UV to near-IR hint the potential use of these clusters in applications such as solar cells.

In FTIR measurements, DMF and paraffin oil was used for solvent dispersion of the crystals with two different window alternatives as TPX and KBr for the sample holders. The IR spectrum was screened from 2600 cm^{-1} to 20 cm^{-1} and possible identification of vibrational bands of clusters was investigated. Due to the high moisture conditions of DMF-based measurements, paraffin oil-based measurements were chosen to be compared with the computational results. In metal-metal region, the possible combinations of different Ni-Ni, Ni-Ge and Ge-Ge modes as well as the

phonon mode of the clusters were observed in both cases. In the region where M-CO bending and Ni-P stretching takes place, it was observed that no clear distinction between M-CO bending and Ni-P stretching could be made since the computational results of $[\text{Ni}_2\text{Ge}_9(\text{PPh}_3)]^{2-}$ and $[\text{Ni}_6\text{Ge}_{13}(\text{CO})_5]^{4-}$ revealed very similar bands in the same region. In the PPh_3 region, both clusters showed similar bands of PPh_3 modes; although, $[\text{Ni}_6\text{Ge}_{13}(\text{CO})_5]^{4-}$ cluster does not have any PPh_3 groups. A similar situation was observed in the CO region where $[\text{Ni}_2\text{Ge}_9(\text{PPh}_3)]^{2-}$ cluster also had an absorption. These results demonstrate the formation of crystals of CO containing compound such as $[\text{Ni}_2\text{Ge}_9(\text{CO})]^{2-}$ along with the ones of $[\text{Ni}_2\text{Ge}_9(\text{PPh}_3)]^{2-}$. The results obtained from FTIR as well as ESI mass spectrometer analyses verify this observation. In the comparison of experimental results with the computational ones, the FTIR bands exhibited more resemblance to the results obtained from CEP-121g calculations.

In fluorescence spectroscopy, a wide range of excitation wavelengths were tested to investigate possible fluorescence activities of both clusters. Even though DMF signals interfere with the observed signals of clusters, the investigation demonstrated that both clusters are promising fluorescent materials.

REFERENCES

- (1) Castleman, a. W.; Khanna, S. N. *J. Phys. Chem. C* **2009**, *113*, 2664.
- (2) Claridge, S. a; Castleman, a W.; Khanna, S. N.; Murray, C. B.; Sen, A.; Weiss, P. S. *ACS Nano* **2009**, *3*, 244.
- (3) Clusters <http://curie.chem.metu.edu.tr/~emren/research/clusters/> (accessed Aug 28, 2014).
- (4) Khanna, S. N.; Weiss, P. S. *ACS Nano* **2010**, *4*, 235–240.
- (5) Kesanli, B.; Fettingler, J. C.; Gardner, R.; Eichhorn, B. W. *J. Am. Chem. Soc.* **2002**, *124*, 4779.
- (6) Hauptmann, R.; Fassler, T. F. *Krist. New Cryst. Struct.* **2003**, *218*, 461.
- (7) Kircher, P.; Huttner, G.; Heinze, K.; Renner, G. *Angew. Chemie* **1998**, *37*, 1664.
- (8) Wang, J.-Q.; Stegmaier, S.; Wahl, B.; Fassler, T. F. *Inorg. Chem.* **2010**, *16*, 1793.
- (9) Scharfe, S.; Fassler, T. F. *Eur. J. Inorg. Chem.* **2010**, 1207.
- (10) Sun, Z.-M.; Zhao, Y.-F.; Li, J.; Wang, L.-S. *J. Clust. Sci.* **2009**, *20*, 601.
- (11) Henke, F.; Schenk, C.; Schnepf, A. *Dalt. Trans.* **2009**, 9141.
- (12) Goicoechea, J. M.; Sevov, S. C. *J. Am. Chem. Soc.* **2005**, *127*, 7676.
- (13) Kocak, F. S.; Zavalij, P.; Lam, Y.-F.; Eichhorn, B. W. *Inorg. Chem.* **2008**, *47*, 3515.
- (14) Sun, Z.-M.; Xiao, H.; Li, J.; Wang, L. S. *J. Am. Chem. Soc.* **2007**, *129*, 9560.
- (15) Esenturk, E. N.; Fettingler, J.; Eichhorn, B. *Polyhedron* **2006**, *25*, 521.

- (16) Esenturk, E. N.; Fettinger, J. C.; Eichhorn, B. W. *J. Am. Chem. Soc.* **2006**, *128*, 12.
- (17) Esenturk, E. N.; Fettinger, J.; Lam, Y.-F.; Eichhorn, B. *Angew. Chem. Int. Ed. Engl.* **2004**, *43*, 2132.
- (18) Esenturk, E. N.; Fettinger, J.; Eichhorn, B. *J. Am. Chem. Soc.* **2006**, *128*, 9178.
- (19) Scharfe, S.; Fässler, T. F.; Stegmaier, S.; Hoffmann, S. D.; Ruhland, K. *Chem. Eur. J.* **2008**, *14*, 4479.
- (20) Wang, J.-Q.; Stegmaier, S.; Fässler, T. F. *Angew. Chem. Int. Ed. Engl.* **2009**, *48*, 1998.
- (21) Goicoechea, J. M.; Sevov, S. C. *J. Am. Chem. Soc.* **2006**, *128*, 4155.
- (22) Benda, C. B.; Schäper, R.; Schulz, S.; Fässler, T. F. *Eur. J. Inorg. Chem.* **2013**, *2013*, 5964.
- (23) Fassler, T. F. et. al. *J. Am. Chem. Soc.* **2012**, *134*, 14450.
- (24) Fassler, T. F.; Schutz, U. *Inorg. Chem.* **1999**, *38*, 1866.
- (25) Goicoechea, J. M.; Sevov, S. C. *Angew. Chem. Int. Ed. Engl.* **2005**, *44*, 4026.
- (26) Li, F.; Sevov, S. C. *Inorg. Chem.* **2012**, *51*, 2706.
- (27) Rios, D.; Gillett-Kunnath, M. M.; Taylor, J. D.; Oliver, A. G.; Sevov, S. C. *Inorg. Chem.* **2011**, *50*, 2373.
- (28) Rios, D.; Sevov, S. C. *Inorg. Chem.* **2010**, *49*, 6396.
- (29) Waibel, M.; Fässler, T. F. *Inorg. Chem.* **2013**, *52*, 5861.
- (30) Wang, J.-Q.; Stegmaier, S.; Wahl, B.; Fässler, T. F. *Chem. Eur. J.* **2010**, *16*, 1793.
- (31) Zhou, B.; Denning, M. S.; Kays, D. L.; Goicoechea, J. M. *J. Am. Chem. Soc.* **2009**, *131*, 2802.
- (32) Zhou, B.; Krämer, T.; Thompson, A. L.; McGrady, J. E.; Goicoechea, J. M. *Inorg. Chem.* **2011**, *50*, 8028.

- (33) Atkins, P.; Overton, T.; Rourke, J.; Weller, M.; Armstrong, F.; Shriver, F. *Shriver & Atkins' Inorganic Chemistry*; 5th ed.; Oxford University Press: Oxford, 2010.
- (34) Sherigara, B. S.; Kutner, W.; D'Souza, F. *Electroanalysis* **2003**, *15*, 753.
- (35) Milani, P. et al. *Eur. Lett.* **1999**, *46*, 245.
- (36) Wayner, D. M.; Huang, Y. *J. Am. Chem. Soc.* **1993**, *115*, 367.
- (37) Harneit, W. *Phys. Rev. A* **2002**, *65*, 032322.
- (38) Bonnemann, H.; Braun, G.; Brijoux, W.; Brinkmann, R.; Schulze Tilling, A.; Seevogel, K.; Siepen, K. *Organomet. Chem.* **1996**, *520*, 143.
- (39) Hunter, R. J. *Foundations of Colloid Science*; Oxford University Press: New York, 1987.
- (40) Gonzalez-Moraga, G. *Cluster Chemistry: Introduction to the chemistry of transition metal and main group element molecular clusters*; Springer-Verlag: Berlin, New York, 1993.
- (41) Kroto, H. W.; Heath, J. R.; O'Brien, S. C.; Curl, R. F.; Smalley, R. E. *Nature* **1985**, *318*, 162.
- (42) Kraetschmer, W.; Lamb, L. D.; Fostiropoulos, K.; Huffman, D. R. *Nature* **1990**, *347*, 354.
- (43) Castlemen, A. W. *Science (80-.)*. **1992**, *225*, 1411.
- (44) Scharfe, S.; Kraus, F.; Stegmaier, S.; Schier, A.; Fässler, T. F. *Angew. Chem. Int. Ed. Engl.* **2011**, *50*, 3630.
- (45) Buckyball <http://web.stevens.edu/nue/images/buckyball.png> (accessed Aug 28, 2014).
- (46) Johannis, A. *Comptes rendus Hebd. des seances l'academie des Sci.* **1891**, 113.
- (47) Kraus, C. A. *J. Am. Chem. Soc.* **1907**, *29*, 1557.
- (48) Kraus, C. A. *J. Am. Chem. Soc.* **1922**, *44*, 1216.
- (49) Kraus, C. A. *J. Am. Chem. Soc.* **1924**, *47*, 43.

- (50) Smyth, F. A. *J. Am. Chem. Soc.* **1917**, *39*, 1299.
- (51) Zintl, E.; Goubeau, J.; Dullenkopf, W. *Z. Phys. Chem.* **1931**, *154*, 1.
- (52) Diehl, L.; Khodadadeh, K.; Kummer, D. *J. Am. Chem. Soc.* **1976**, *109*, 3404.
- (53) Zintl, E.; Harder, A. *Z. Phys. Chem. Abst. A.* **1931**, 154.
- (54) Muller, U. *Inorganic Structural Chemistry*; 2nd ed.; John Wiley & Sons: West Sussex, 2006.
- (55) Corbett, J. D.; Belin, C. H.; Cisar, A. *J. Am. Chem. Soc.* **1977**, *99*, 7163.
- (56) Adolphson, D. G.; Corbett, J. D.; Merryman, D. J. *J. Am. Chem. Soc.* **1976**, *98*, 7234.
- (57) Hoffmann, R.; Fassler, T. F. *Angew. Chem. Int. Ed. Engl.* **1999**, *38*, 543.
- (58) Corbett, J. D.; Edwards, P. A. *J. Am. Chem. Soc.* **1977**, *99*, 3313.
- (59) Hoffmann, R.; Fassler, T. F. **1999**, 3339.
- (60) Todorov, E.; Sevov, S. C. *Inorg. Chem.* **1998**, *37*, 3889.
- (61) Queneau, V.; Sevov, S. C. *Angew. Chem. Int. Ed. Engl.* **1997**, *36*, 1754.
- (62) Dahlmann, W.; VonSchnering, H. G. *Naturwissenschaften* **1973**, *60*, 429.
- (63) Dahlmann, W.; VonSchnering, H. G. *Naturwissenschaften* **1972**, *59*, 420.
- (64) Laves, F. *Naturwissenschaften* **1941**, *29*, 244.
- (65) Critchlow, S. C.; Corbett, J. D. *Inorg. Chem.* **1984**, *23*, 770.
- (66) Wade, K. *Inorg. Chem. Radiochem.* **1976**, *18*, 1.
- (67) Mingos, D. M. *P. Acc. Chem. Res.* **1984**, *17*, 311.
- (68) Fassler, T. F. *Coord. Chem. Rev.* **2001**, *215*, 347.
- (69) Corbett, J. D. *Chem. Rev.* **1985**, *85*, 383.
- (70) Sevov, S. C.; Goicoechea, J. M. *Organometallics* **2006**, *25*, 5678.

- (71) Spiekermann, A.; Hoffmann, S. D.; Fässler, T. F. *Angew. Chem. Int. Ed. Engl.* **2006**, *45*, 3459.
- (72) Cui, L.-F.; Wang, L.-S. *Int. Rev. Phys. Chem.* **2008**, *27*, 139.
- (73) Xu, L.; Sevov, S. C. *J. Am. Chem. Soc.* **1999**, *121*, 9245.
- (74) Ugrinov, A.; Sevov, S. C. *J. Am. Chem. Soc.* **2002**, *124*, 10990.
- (75) Downie, C.; Tnag, Z. J.; Guloy, A. M. *Angew. Chem. Int. Ed. Engl.* **2000**, *39*, 338.
- (76) Downie, C.; Mao, J. G.; Guloy, A. M. *Inorg. Chem.* **2001**, *40*, 4721.
- (77) Haushalter, R. C.; Eichhorn, B. W. *J. Am. Chem. Soc. Chem Commun.* **1990**, 937.
- (78) Haushalter, R. C.; Eichhorn, B. W. *J. Am. Chem. Soc.* **1988**, *110*, 8704.
- (79) Kauzlarich, S. M. *Chemistry, structure and bonding of zintl phases and ions*; VCH Publishers Inc: New York, 1996.
- (80) Esenturk, E. N.; Fettinger, J.; Eichhorn, B. *Chem. Commun.* **2005**, 247.
- (81) Kesanli, B.; Halsig, J. E.; Zavalij, P.; Fettinger, J. C.; Lam, Y.-F.; Eichhorn, B. W. *J. Am. Chem. Soc.* **2007**, *129*, 4567.
- (82) Buffat, P. *Phys. Rev. A* **1976**, *13*.
- (83) Espinoza-quintero, G.; Duckworth, J. C. A.; Myers, W. K.; Mcgrady, J. E.; Goicoechea, J. M. **2014**, *10*.
- (84) Moses, M. J.; Fettinger, J. C.; Eichhorn, B. W. *Science* **2003**, *300*, 778.
- (85) Xie, H.; Qin, Z.; Wu, X.; Tang, Z.; Jiang, L. *J. Chem. Phys.* **2012**, *137*, 064318.
- (86) Grubisic, A.; Wang, H.; Li, X.; Ko, Y.-J.; Kocak, F. S.; Pederson, M. R.; Bowen, K. H.; Eichhorn, B. W. *Proc. Natl. Acad. Sci. U. S. A.* **2011**, *108*, 14757–14762.
- (87) Jensen, F. *Introduction to computational chemistry*; 2nd ed.; John Wiley & Sons: England, 2007.

- (88) Koch, W.; Hertwig, R. H. *Density functional theory applications to transition metal problems*; 1st ed.; Encyclopedia of Computational Chemistry, 2002.
- (89) Gill, P. M. W. *Density Functional Theory (DFT), Hartree–Fock (HF), and the Self-consistent Field*; Encyclopedia of Computational Chemistry: Cambridge, 2002.
- (90) Delley, B.; Wrinn, M.; Luthi, H. P. *Chem. Phys. Letts.* **1985**, *117*, 151.
- (91) Wang, H.; Sun, X.; Du, J. *Int. J. Quantum Chem.* **2008**, *108*, 1505.
- (92) Heiles, S.; Johnston, R. L.; Schäfer, R. *J. Phys. Chem. A* **2012**, *116*, 7756.
- (93) Muñoz-Castro, A.; Sevov, S. C. *Phys. Chem. Chem. Phys.* **2013**, *15*, 986.
- (94) Uță, M. M.; Cioloboc, D.; King, R. B. *J. Phys. Chem. A* **2012**, *116*, 9197.
- (95) Wiesel, A.; Drebov, N.; Rapps, T.; Ahlrichs, R.; Schwarz, U.; Kelting, R.; Weis, P.; Kappes, M. M.; Schooss, D. *Phys. Chem. Chem. Phys.* **2012**, *14*, 234.
- (96) Tomberg, A. *Gaussian 09W tutorial*; McGill University.
- (97) Gaussian. Basis sets http://www.gaussian.com/g_tech/g_ur/m_basis_sets.htm (accessed Aug 28, 2014).
- (98) Dhaka, K.; Trivedi, R.; Bandyopadhyay, D. *J. Mol. Model.* **2013**, *19*, 1473.
- (99) Wang, J.; Han, J.-G. *J. Phys. Chem. B* **2006**, *110*, 7820.
- (100) Martin, R. L.; Hay, J.; Roy, L. E. *J. Chem. Theory Comput.* **2008**, *4*, 1029.
- (101) Foresman, J. B.; Frisch, A. *Exploring chemistry with electronic structure methods*; 2nd ed.; Gaussian Inc: Pittsburgh, PA, 1996.
- (102) Ochterski, J. W. Vibrational analysis in Gaussian http://www.gaussian.com/g_whitepap/vib/vib.pdf (accessed Aug 28, 2014).
- (103) Kahn, K. Description of electronically excited states http://web.chem.ucsb.edu/~kalju/chem126/public/elspect_theory.html (accessed Aug 28, 2014).
- (104) Gaussian. TD http://www.gaussian.com/g_tech/g_ur/k_td.htm (accessed Aug 28, 2014).

- (105) Gaussian. SCRF http://www.gaussian.com/g_tech/g_ur/k_scrf.htm (accessed Aug 28, 2014).
- (106) NSM Archive. Band structure <http://www.ioffe.ru/SVA/NSM/Semicond/SiGe/bandstr.html#Band> (accessed Sep 7, 2014).
- (107) NIST. Precomputed vibrational scaling factors <http://cccbdb.nist.gov/vibscale.asp> (accessed Sep 7, 2014).
- (108) Carey, N. a. D.; Clark, H. C. *Chem. Commun.* **1967**, 292.
- (109) Schumann, H.; Stelzer, O. *Angew. Chem. Int. Ed. Engl.* **1967**, 6, 701.
- (110) Schmidbaur, H.; Klein, H. F.; Eiglmeier, K. *Angew. Chem. Int. Ed. Engl.* **1967**, 8, 806.
- (111) Daasch, L.; Smith, D. *Anal. Chem.* **1951**, 23, 853.
- (112) University, C. IR spectroscopy tutorial: Aromatics <http://orgchem.colorado.edu/Spectroscopy/irtutor/aromaticsir.html> (accessed Sep 7, 2014).
- (113) Shurvell, H. F. *Spectrochim. Acta.* **1967**, 23, 2925.
- (114) Chemistry, L. Carbonyl ligands <http://chem-faculty.lsu.edu/stanley/webpub/4571-chap3-carbonyls.pdf> (accessed Sep 7, 2014).

APPENDIX A

DATA RELATIVE TO CHAPTER 1

Use of Gaussian 09 Software on TR-Grid

Since clusters have high number of electrons and complicated structures, the capacity of a regular computer would not be enough to calculate their properties. Therefore, Linux based system such as TR-Grid, which is provided by ULAKBIM, can be used. TR-Grid requires SSH client programs to send commands in Windows, such as MobaXterm, Putty, etc. By using a specific username and password, a secure connection to TR-Grid can be achieved by those programs.(Figure A.1.)

Since TR-Grid operates in Linux, there are certain types of commands needed. Some of the important ones used are shown in Table A.1.

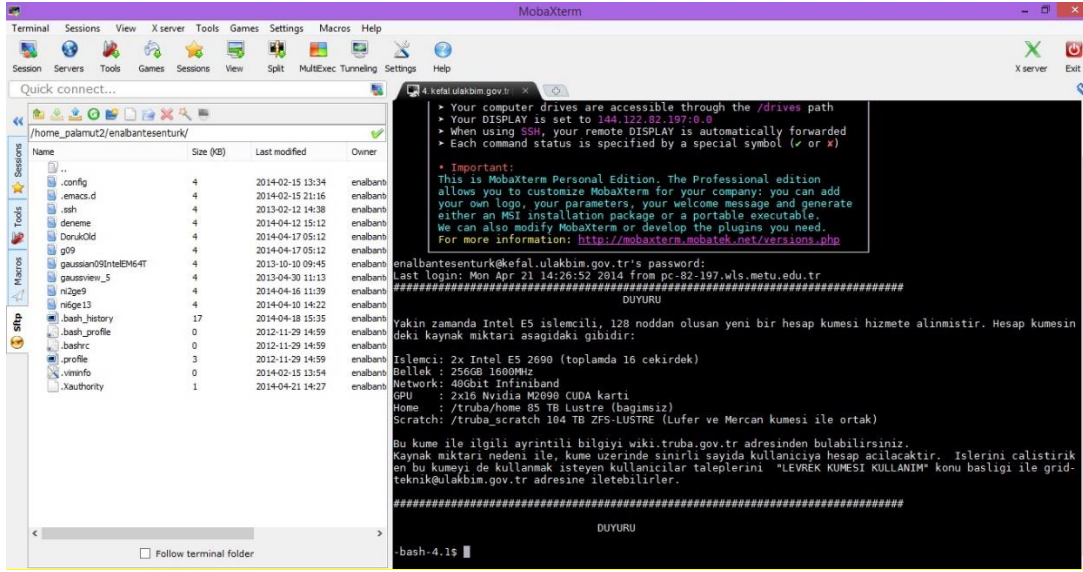


Figure A.1. The screenshot of MobaXterm

Table A.1. Important commands used in TR-Grid

Code	Extensions after one 'space'?	What does it do?
mkdir	directoryname	creates new directories
cd	directoryname	changes directories
cd	..	goes to an upper directory
pwd	no extension!	tells you where you are
nano	file name	opens a file to edit
sbatch	example.slurm	submits a job
scancel	job number	Cancels a job
squeue	no extension!	shows running jobs
sinfo	no extension!	shows available nodes

Input, Slurm and Output Files

An input file consists of a checkpoint file (.chk extension) storing the necessary information which can be used to restart or continue from an incomplete calculation, memory limit given in million words (Mw), the route line including the calculation type, method and basis set, description of the calculation, and the coordinates of the system which can either be given as Cartesian (x, y, z) or z-matrix (A = Angle, B = Bond length, D = Dihedral angle).(Figure A.2.)

```
1 %chk=ni2ge9_cep121g_opt.chk
2 $mem=400Mw
3 #p opt b3lyp/CEP-121G
4
5 Restarted using the coordinates in 241112
6
7 -2 1
8 C
9 C          1          B1
10 H         2          B2   1          A1
11 C         2          B3   1          A2      3          D1   0
12 H         4          B4   2          A3      1          D2   0
13 C         4          B5   2          A4      1          D3   0
14 H         6          B6   4          A5      2          D4   0
15 C         6          B7   4          A6      2          D5   0
16 H         8          B8   6          A7      4          D6   0
17 Ge        8          B9   6          A8      4          D7   0
18 Ge        10         B10  8          A9      6          D8   0
19 Ge        11         B11  10         A10     8          D9   0
20 Ge        12         B12  11         A11    10         D10  0
21 Ge        11         B13  10         A12     8          D11  0
22 Ge        14         B14  11         A13    10         D12  0
23 Ge        15         B15  14         A14    11         D13  0
24 Ge        10         B16   8          A15     6          D14  0
25 Ge        17         B17  10         A16     8          D15  0
26 Ni        12         B18  11         A17    10         D16  0
27 Ni        19         B19  12         A18    11         D17  0
28 P         20         B20  19         A19    12         D18  0
```

Figure A.2. Input file example with z-matrix coordinates

In addition to input file, a slurm file, which is a batch file, is required to start a calculation.(Figure A.3) The slurm file has all the information to initiate a run

including operating platform, partition name, user name, job name, and number of nodes, time, working, output and error directories, and a command line to run Gaussian with input file name.

By using the slurm file, a calculation can be submitted. Simultaneously, output and error files are created by the program in the given destinations. In the case of a successfully ended calculation, the output file can be downloaded via MobaXterm and be opened in programs such as GaussView for visualization of results.

```
1 #!/bin/bash
2 #SBATCH -M linux
3 #SBATCH -p mid2
4 #SBATCH -A enalbantesenturk
5 #SBATCH -J Ni2copsol
6 #SBATCH -N 1
7 #SBATCH -n 16
8 #SBATCH --time=7-00:00
9 #SBATCH --workdir=/truba_scratch/enalbantesenturk/ni2ge9/cep121g/opt/
10 #SBATCH --output=ni2ge9_cep121g_opt_sol-%j.out
11 #SBATCH --error=ni2ge9_cep121g_opt_sol-%j.err
12
13 export OMP_NUM_THREADS=1
14 export g09root=$HOME
15 export GAUSS_SCRDIR=/tmp
16 . $g09root/g09/bsd/g09.profile
17
18 echo "SLURM_NODELIST $SLURM_NODELIST"
19 $g09root/g09/g09 < /home_palamut2/enalbantesenturk/ni2ge9/cep121g/opt/ni2ge9_b31yp_cep121g_opt_sol.com
```

Figure A.3. Slurm file example

APPENDIX B

DATA RELATIVE TO CHAPTER 3

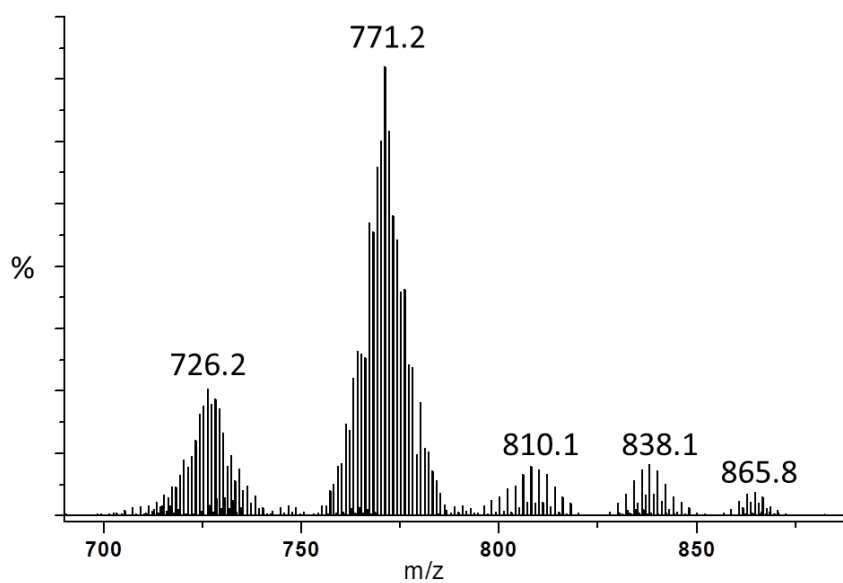


Figure A.4. ESI mass spectra (negative ion mode) of $[\text{K}(2,2,2\text{-crypt})]_2[\text{Ni}_2\text{Ge}_9(\text{PPh}_3)]$ salt showing mass envelopes of $[\text{K}[\text{Ni}_2\text{Ge}_9(\text{CO})(\text{CN})]^{-1}]^{-1}$ ($m/z = 865.8$), $[\text{K}[\text{Ni}_2\text{Ge}_9(\text{CO})]^{-1}]^{-1}$ ($m/z = 838.1$), $[\text{K}[\text{Ni}_2\text{Ge}_9]^{-1}]^{-1}$ ($m/z = 810.1$), $[\text{Ni}_2\text{Ge}_9]^{-1}$ ($m/z = 771.2$) and $[\text{Ni}_2\text{Ge}_8(\text{CO})]^{-1}$ ($m/z = 726.2$) ions

Table A.2. Cartesian coordinates of $[\text{Ni}_2\text{Ge}_9(\text{PPh}_3)]^{2-}$ crystal structure

Atoms	x (Å)	y (Å)	z (Å)
<i>Ge</i>	12.6102	2.1177	18.6437
<i>Ge</i>	12.9168	2.8904	16.1384
<i>Ge</i>	10.3458	2.4922	15.7276
<i>Ge</i>	9.9558	-0.0583	15.4622
<i>Ge</i>	12.4627	0.7372	14.5363
<i>Ge</i>	14.0982	0.4718	16.6116
<i>Ge</i>	12.2195	-1.3467	16.1413
<i>Ge</i>	12.4595	-0.4855	18.6805
<i>Ge</i>	9.9369	0	18.0948
<i>Ni</i>	11.7009	0.9055	16.8474
<i>Ni</i>	10.304	2.3413	18.0939
<i>P</i>	9.0551	3.7003	19.1381

Table A.3. Cartesian coordinates of optimized structures of $[\text{Ni}_2\text{Ge}_9(\text{PPh}_3)]^{2-}$

Atoms	Lanl2dz			CEP-121g		
	x (Å)	y (Å)	z (Å)	x (Å)	y (Å)	z (Å)
<i>Ge</i>	-3.15393	1.421401	-5.88469	0.02276	1.784554	1.224294
<i>Ge</i>	-3.56378	4.050912	-5.37645	1.701039	2.479779	-0.77823
<i>Ge</i>	-3.61538	3.297224	-2.76151	0.823455	0.216064	-1.9947
<i>Ge</i>	-6.10744	2.419466	-2.15748	2.255368	-1.87111	-1.04042
<i>Ge</i>	-6.24222	4.354635	-4.31529	3.801682	0.537489	-0.8817
<i>Ge</i>	-5.89955	2.916987	-6.67722	3.200775	1.699694	1.538684
<i>Ge</i>	-7.50334	1.892162	-4.64384	3.547939	-1.02445	1.369408

Table A.3. (Continued)

Atoms	Lanl2dz			CEP-121g		
	x (Å)	y (Å)	z (Å)	x (Å)	y (Å)	z (Å)
<i>Ge</i>	-5.55709	0.144025	-5.90503	1.293638	-0.00738	2.821508
<i>Ge</i>	-5.27825	0.051734	-3.21159	0.484248	-1.85274	1.018831
<i>Ni</i>	-3.07377	1.040391	-3.48499	-0.73955	-0.08797	-0.1435
<i>P</i>	-1.32716	0.033149	-2.62188	-2.8793	-0.32979	-0.55192

Table A.4. Cartesian coordinates of $[\text{Ni}_6\text{Ge}_{13}(\text{CO})_5]^{4-}$ crystal structure

Atoms	x (Å)	y (Å)	z (Å)
<i>O</i>	0	0	0
<i>Ge</i>	0	0	3.877657
<i>Ni</i>	1.985159	0	2.094976
<i>Ni</i>	0.472876	1.927114	2.117367
<i>Ge</i>	-0.22555	2.561159	4.550425
<i>Ge</i>	1.130581	0.82582	6.424437
<i>Ge</i>	2.445063	-0.93551	4.467202
<i>Ni</i>	1.941703	1.49095	4.231683
<i>Ge</i>	2.909039	2.327554	2.223466
<i>Ni</i>	1.617365	4.013822	3.535851
<i>Ge</i>	1.982102	3.305142	5.983156
<i>Ge</i>	3.77831	1.077558	5.92733
<i>Ni</i>	4.291975	0.638098	3.432266
<i>Ni</i>	3.940531	3.095904	4.293154
<i>Ge</i>	5.513288	2.713785	2.289916

Table A.4. (Continued)

<i>Ge</i>	3.81091	4.868391	2.420463
<i>Ge</i>	3.241582	5.394702	4.980456
<i>Ge</i>	4.726052	3.639733	6.539061
<i>Ge</i>	6.059569	1.927301	4.780191
<i>Ge</i>	5.786983	4.703723	4.209092
<i>C</i>	2.788852	-1.30284	1.368007
<i>O</i>	3.278551	-2.25257	0.85608
<i>C</i>	0.561666	0.415677	0.973387
<i>C</i>	-0.5673	3.046126	1.346152
<i>O</i>	-1.35904	3.735287	0.85289
<i>C</i>	0.668064	5.30707	2.928187
<i>O</i>	0.061786	6.202723	2.453542
<i>C</i>	5.394977	-0.50691	2.703541
<i>O</i>	6.102077	-1.22942	2.185706

Table A.5. Cartesian coordinates of optimized structures of $[\text{Ni}_6\text{Ge}_{13}(\text{CO})_5]^{4-}$

Atoms	Lanl2dz			CEP-121g		
	x (Å)	y (Å)	z (Å)	x (Å)	y (Å)	z (Å)
<i>O</i>	2.803941	-1.14413	-4.52917	-2.794	1.16597	-4.56379
<i>Ge</i>	3.595602	-0.13087	-0.83579	-3.58253	0.102086	-0.8752
<i>Ni</i>	1.597204	0.63399	-2.51681	-1.5943	-0.63179	-2.56857
<i>Ni</i>	1.667902	-1.73351	-1.87962	-1.68971	1.735135	-1.90428
<i>Ge</i>	2.39265	-2.07464	0.660781	-2.40637	2.019061	0.665886

Table A.5. (Continued)

<i>Ge</i>	2.649738	0.68023	2.17139	-2.71815	-0.68518	2.033143
<i>Ge</i>	2.27035	2.241148	-0.51104	-2.2285	-2.23782	-0.52181
<i>Ni</i>	1.266403	0.083215	0.182157	-1.2244	-0.07897	0.130505
<i>Ge</i>	-0.443	-0.41093	-1.4479	0.462874	0.431566	-1.47584
<i>Ni</i>	-0.16619	-2.20825	0.277187	0.168802	2.219059	0.26871
<i>Ge</i>	0.405329	-0.86535	2.412831	-0.43965	0.830004	2.404224
<i>Ge</i>	0.320007	2.01699	1.625336	-0.3163	-2.02041	1.621065
<i>Ni</i>	-0.29147	2.034553	-0.88612	0.337863	-2.02007	-0.91594
<i>Ni</i>	-1.42751	0.177202	0.778581	1.41075	-0.16308	0.783807
<i>Ge</i>	-2.76297	1.059563	-1.40908	2.798945	-1.00971	-1.33567
<i>Ge</i>	-2.66823	-1.8008	-0.61717	2.690397	1.781653	-0.52528
<i>Ge</i>	-2.07521	-1.95343	2.088836	2.053313	1.905369	2.156563
<i>Ge</i>	-2.05631	0.792964	3.088986	1.990236	-0.80933	3.120068
<i>Ge</i>	-2.22642	2.616508	0.81455	2.278356	-2.55969	0.851271
<i>Ge</i>	-3.93819	0.146722	1.033528	3.903464	-0.14185	1.179877
<i>C</i>	1.530994	1.889154	-3.74363	-1.56134	-1.86668	-3.80745
<i>O</i>	1.553147	2.720815	-4.60747	-1.65361	-2.66604	-4.71136
<i>C</i>	2.303118	-0.86306	-3.45281	-2.28205	0.877135	-3.48161
<i>C</i>	1.727351	-3.43714	-2.30516	-1.8306	3.442535	-2.27302
<i>O</i>	1.840882	-4.59108	-2.61351	-2.04593	4.602296	-2.53922
<i>C</i>	-0.24139	-3.96193	0.23673	0.314769	3.958495	0.155288
<i>O</i>	-0.33929	-5.15837	0.253026	0.453218	5.158989	0.108127
<i>C</i>	-0.47507	3.527593	-1.79158	0.580641	-3.51363	-1.7963
<i>O</i>	-0.6081	4.57915	-2.35543	0.748456	-4.56864	-2.36449

Table A.6. Comparison of bond lengths calculated with both basis sets:
 $[\text{Ni}_2\text{Ge}_9(\text{PPh}_3)]^{2-}$

	Bond Lengths (Å)				
	Crystal Structure	Lanl2dz Optimized	Difference	CEP-121g Optimized	Difference
<i>R (10-19)</i>	2.350	2.438	0.088	2.425	0.075
<i>R (10-20)</i>	2.381	2.431	0.050	2.441	0.060
<i>R (11-19)</i>	2.433	2.553	0.120	2.542	0.109
<i>R (12-19)</i>	2.368	2.438	0.070	2.424	0.056
<i>R (12-20)</i>	2.371	2.431	0.060	2.442	0.071
<i>R (13-19)</i>	2.428	2.554	0.126	2.542	0.114
<i>R (14-19)</i>	2.439	2.553	0.114	2.532	0.093
<i>R (15-19)</i>	2.448	2.554	0.106	2.532	0.084
<i>R (16-19)</i>	2.417	2.554	0.137	2.533	0.116
<i>R (17-19)</i>	2.423	2.554	0.131	2.542	0.119
<i>R (18-19)</i>	2.343	2.439	0.096	2.425	0.082
<i>R (18-20)</i>	2.370	2.431	0.061	2.442	0.072
<i>R (19-20)</i>	2.359	2.388	0.029	2.390	0.031
<i>R (20-21)</i>	2.121	2.193	0.072	2.192	0.071
<i>R (21-22)</i>	1.847	1.903	0.056	1.920	0.073
<i>R (21-24)</i>	1.843	1.903	0.060	1.920	0.077
<i>R (21-35)</i>	1.840	1.903	0.063	1.920	0.080
<i>R (10-17)</i>	2.608	2.722	0.114	2.716	0.108
<i>R (17-18)</i>	2.635	2.709	0.074	2.704	0.069
<i>R (11-12)</i>	2.634	2.722	0.088	2.716	0.082
<i>R (12-13)</i>	2.594	2.71	0.116	2.705	0.111
<i>R (13-16)</i>	2.692	2.9	0.208	2.863	0.171
<i>R (15-16)</i>	2.657	2.785	0.128	2.751	0.094
<i>R (11-15)</i>	2.733	2.904	0.171	2.868	0.135
<i>R (14-15)</i>	2.656	2.786	0.130	2.751	0.095
<i>R (11-14)</i>	2.722	2.897	0.175	2.863	0.141
<i>R (12-14)</i>	2.997	3.23	0.233	3.196	0.199
<i>R (13-14)</i>	2.788	2.902	0.114	2.867	0.079

Table A.6. (Continued)

<i>R (14-16)</i>	2.642	2.786	0.144	2.752	0.110
<i>R (10-11)</i>	2.64	2.709	0.069	2.704	0.064
<i>R (15-17)</i>	2.808	2.899	0.091	2.863	0.055
<i>R (16-17)</i>	2.692	2.904	0.212	2.868	0.176
<i>R (13-18)</i>	2.633	2.721	0.088	2.716	0.083
Average	2.482	2.591	0.109	2.578	0.096
Minimum	1.840	1.903	0.029	1.920	0.031
Maximum	2.997	3.230	0.233	3.196	0.199
Average <i>R (Ni-Ge)</i>	2.395	2.486	0.091	2.478	0.083
Average <i>R (Ge-Ge)</i>	2.696	2.830	0.135	2.806	0.111

Table A.7. Comparison of bond angles calculated with both basis sets:
[Ni₂Ge₉(PPh₃)²⁻

	Bond Angles (°)				
	Crystal Structure	Lanl2dz Optimized	Difference	CEP-121g Optimized	Difference
<i>A (19-10-20)</i>	59.8	58.7	1.1	58.8	1.0
<i>A (10-19-11)</i>	67.0	65.7	1.3	65.9	1.1
<i>A (10-19-12)</i>	103.7	97.7	6.0	98.3	5.4
<i>A (10-19-13)</i>	156.8	153.5	3.3	154.6	2.2
<i>A (10-19-14)</i>	129.7	130.8	1.1	130.5	0.8
<i>A (10-19-15)</i>	77.6	80.5	2.9	80.2	2.6
<i>A (10-19-16)</i>	128.4	131.2	2.8	130.9	2.5
<i>A (10-19-17)</i>	66.2	66.0	0.2	66.3	0.1
<i>A (10-19-18)</i>	94.8	97.9	3.1	98.4	3.6

Table A.7. (Continued)

<i>A (10-19-20)</i>	60.7	60.5	0.2	60.9	0.2
<i>A (10-20-12)</i>	102.7	98.1	4.6	97.4	5.3
<i>A (10-20-18)</i>	93.3	98.3	5.0	97.5	4.2
<i>A (10-20-19)</i>	59.4	60.8	1.4	60.2	0.8
<i>A (10-20-21)</i>	121.1	119.1	2.0	119.6	1.5
<i>A (11-19-12)</i>	66.5	66.0	0.5	66.2	0.3
<i>A (11-19-13)</i>	121.1	119.7	1.4	119.6	1.5
<i>A (11-19-14)</i>	67.9	69.1	1.2	68.7	0.8
<i>A (11-19-15)</i>	68.1	69.3	1.2	68.8	0.7
<i>A (11-19-16)</i>	124.6	126.0	1.4	125.2	0.6
<i>A (11-19-17)</i>	122.2	119.8	2.4	119.6	2.6
<i>A (11-19-18)</i>	147.9	153.6	5.7	154.6	6.7
<i>A (11-19-20)</i>	87.3	93.1	5.8	93.7	6.4
<i>A (19-12-20)</i>	59.7	58.7	1.0	58.8	0.9
<i>A (12-19-13)</i>	65.5	65.7	0.2	66.0	0.5
<i>A (12-19-14)</i>	77.1	80.6	3.5	80.3	3.2
<i>A (12-19-15)</i>	129.3	131.4	2.1	130.9	1.6
<i>A (12-19-16)</i>	127.5	131.0	3.5	130.6	3.1
<i>A (12-19-17)</i>	157.2	153.3	3.9	154.5	2.7
<i>A (12-19-18)</i>	94.6	97.8	3.2	98.4	3.8
<i>A (12-19-20)</i>	60.2	60.5	0.3	60.9	0.7
<i>A (12-20-18)</i>	93.8	98.2	4.4	97.5	3.7
<i>A (12-20-19)</i>	60.1	60.8	0.7	60.2	0.1
<i>A (12-20-21)</i>	117.4	119.1	1.7	119.8	2.4
<i>A (13-19-14)</i>	69.9	69.2	0.7	68.8	1.1
<i>A (13-19-15)</i>	125.4	126.0	0.6	125.2	0.2
<i>A (13-19-16)</i>	67.5	69.2	1.7	68.7	1.2
<i>A (13-19-17)</i>	115.4	119.8	4.4	119.6	4.2
<i>A (13-19-18)</i>	67.0	66.0	1.0	66.3	0.7
<i>A (13-19-20)</i>	96.7	93.0	3.7	93.7	3.0
<i>A (14-19-15)</i>	65.8	66.1	0.3	65.8	0.0
<i>A (14-19-16)</i>	65.9	66.1	0.2	65.8	0.1
<i>A (14-19-17)</i>	125.4	126.1	0.7	125.2	0.2

Table A.7. (Continued)

<i>A (14-19-18)</i>	135.5	131.2	4.3	130.9	4.6
<i>A (14-19-20)</i>	136.7	141.1	4.4	141.2	4.5
<i>A (15-19-16)</i>	66.2	66.1	0.1	65.8	0.4
<i>A (15-19-17)</i>	70.4	69.2	1.2	68.7	1.7
<i>A (15-19-18)</i>	136.1	130.8	5.3	130.5	5.6
<i>A (15-19-20)</i>	137.6	140.9	3.3	141.1	3.5
<i>A (16-19-17)</i>	67.6	69.3	1.7	68.8	1.2
<i>A (16-19-18)</i>	87.5	80.4	7.1	80.2	7.3
<i>A (16-19-20)</i>	148.1	140.9	7.2	141.1	7.0
<i>A (17-19-18)</i>	67.1	65.7	1.4	65.9	1.2
<i>A (17-19-20)</i>	97.8	92.8	5.0	93.6	4.2
<i>A (19-18-20)</i>	60.1	58.7	1.4	58.8	1.3
<i>A (18-19-20)</i>	60.5	60.5	0.0	60.9	0.4
<i>A (18-20-19)</i>	59.4	60.8	1.4	60.2	0.8
<i>A (18-20-21)</i>	122.8	119.4	3.4	119.9	2.9
<i>A (19-20-21)</i>	177.2	179.8	2.6	179.8	2.6
<i>Average</i>	96.5	96.6	2.5	96.6	2.3
<i>Minimum</i>	59.4	58.7	0.0	58.8	0.0
<i>Maximum</i>	177.2	179.8	7.2	179.8	7.3

Table A.8. Comparison of bond lengths calculated with both basis sets:
 $[\text{Ni}_6\text{Ge}_{13}(\text{CO})_5]^{4-}$

	Bond Lengths (Å)				
	Crystal Structure	Lanl2dz Optimized	Difference	CEP-121g Optimized	Difference
<i>R</i> (1-23)	1.198	1.220	0.022	1.232	0.034
<i>R</i> (2-3)	2.668	2.721	0.053	2.713	0.045
<i>R</i> (2-4)	2.653	2.716	0.063	2.703	0.050
<i>R</i> (2-8)	2.474	2.551	0.077	2.570	0.096
<i>R</i> (3-4)	2.450	2.453	0.003	2.460	0.010
<i>R</i> (3-7)	2.591	2.657	0.066	2.678	0.087
<i>R</i> (3-8)	2.606	2.774	0.168	2.780	0.174
<i>R</i> (3-9)	2.508	2.529	0.021	2.561	0.053
<i>R</i> (3-21)	1.695	1.756	0.061	1.750	0.055
<i>R</i> (3-23)	1.859	1.901	0.042	1.893	0.034
<i>R</i> (4-5)	2.610	2.664	0.054	2.683	0.073
<i>R</i> (4-8)	2.611	2.777	0.166	2.765	0.154
<i>R</i> (4-9)	2.471	2.528	0.057	2.553	0.082
<i>R</i> (4-23)	1.898	1.907	0.009	1.891	0.007
<i>R</i> (4-24)	1.711	1.757	0.046	1.752	0.041
<i>R</i> (5-8)	2.438	2.481	0.043	2.467	0.029
<i>R</i> (5-10)	2.557	2.591	0.034	2.613	0.056
<i>R</i> (6-8)	2.431	2.495	0.064	2.494	0.063
<i>R</i> (7-8)	2.489	2.479	0.010	2.469	0.020
<i>R</i> (7-13)	2.638	2.597	0.041	2.606	0.032
<i>R</i> (8-9)	2.381	2.413	0.032	2.385	0.004
<i>R</i> (8-10)	2.637	2.704	0.067	2.691	0.054
<i>R</i> (8-11)	2.522	2.572	0.050	2.571	0.049
<i>R</i> (8-12)	2.534	2.592	0.058	2.611	0.077
<i>R</i> (8-13)	2.625	2.716	0.091	2.703	0.078
<i>R</i> (8-14)	2.564	2.761	0.197	2.716	0.152
<i>R</i> (9-10)	2.497	2.507	0.010	2.515	0.018
<i>R</i> (9-13)	2.496	2.514	0.018	2.518	0.022
<i>R</i> (9-14)	2.437	2.504	0.067	2.522	0.085

Table A.8. (Continued)

<i>R (10-11)</i>	2.574	2.587	0.013	2.619	0.045
<i>R (10-14)</i>	2.610	2.745	0.135	2.735	0.125
<i>R (10-16)</i>	2.605	2.688	0.083	2.680	0.075
<i>R (10-17)</i>	2.575	2.644	0.069	2.686	0.111
<i>R (10-26)</i>	1.715	1.756	0.041	1.749	0.034
<i>R (11-14)</i>	2.595	2.668	0.073	2.653	0.058
<i>R (12-13)</i>	2.585	2.585	0.000	2.620	0.035
<i>R (12-14)</i>	2.602	2.675	0.073	2.671	0.069
<i>R (13-14)</i>	2.628	2.741	0.113	2.737	0.109
<i>R (13-15)</i>	2.666	2.708	0.042	2.693	0.027
<i>R (13-19)</i>	2.570	2.641	0.071	2.680	0.110
<i>R (13-28)</i>	1.749	1.756	0.007	1.751	0.002
<i>R (14-15)</i>	2.575	2.711	0.136	2.671	0.096
<i>R (14-16)</i>	2.582	2.720	0.138	2.671	0.089
<i>R (14-17)</i>	2.499	2.584	0.085	2.564	0.065
<i>R (14-18)</i>	2.441	2.472	0.031	2.492	0.051
<i>R (14-19)</i>	2.468	2.567	0.099	2.550	0.082
<i>R (14-20)</i>	2.450	2.524	0.074	2.524	0.074
<i>R (21-22)</i>	1.185	1.199	0.014	1.210	0.025
<i>R (24-25)</i>	1.160	1.200	0.040	1.209	0.049
<i>R (26-27)</i>	1.181	1.201	0.020	1.209	0.028
<i>R (28-29)</i>	1.136	1.201	0.065	1.210	0.074
<i>Average</i>	2.322	2.381	0.061	2.381	0.062
<i>Minimum</i>	1.136	1.199	0.000	1.209	0.002
<i>Maximum</i>	2.668	2.777	0.197	2.780	0.174
<i>Average R (Ni-Ni)</i>	2.591	2.698	0.107	2.709	0.118
<i>Average R (Ni-Ge)</i>	2.537	2.594	0.060	2.590	0.056
<i>Average R (Ge-Ge)</i>	2.755	2.895	0.140	2.865	0.110

Table A.9. Comparison of bond angles calculated with both basis sets:
 $[\text{Ni}_6\text{Ge}_{13}(\text{CO})_5]^4-$

	Bond Angles (°)				
	Crystal Structure	Lanl2dz Optimized	Difference	CEP-121g Optimized	Difference
A(1-23-3)	140.5	140.2	0.3	139.6	0.9
A(1-23-4)	138.1	139.4	1.3	139.2	1.1
A(3-2-4)	54.8	53.6	1.2	54.0	0.8
A(3-2-8)	60.8	63.4	2.6	63.4	2.6
A(2-3-4)	62.3	63.1	0.8	62.8	0.5
A(2-3-7)	61.3	61.2	0.1	60.8	0.5
A(2-3-9)	103.9	102.4	1.5	102.1	1.8
A(2-3-21)	129.8	131.3	1.5	130.3	0.5
A(2-3-23)	80.4	79.1	1.3	79.6	0.8
A(4-2-8)	61.1	63.6	2.5	63.2	2.1
A(2-4-3)	62.9	63.3	0.4	63.2	0.3
A(2-4-5)	60.7	61.0	0.3	60.8	0.1
A(2-4-9)	105.4	102.6	2.8	102.6	2.8
A(2-4-23)	80.2	79.1	1.1	79.9	0.3
A(2-4-24)	131.7	129.9	1.8	127.8	3.9
A(2-8-5)	65.5	65.8	0.3	65.5	0.0
A(2-8-6)	72.7	80.3	7.6	76.5	3.8
A(2-8-7)	65.5	65.9	0.4	65.5	0.0
A(2-8-9)	114.2	111.1	3.1	111.7	2.5
A(2-8-11)	123.1	128.4	5.3	127.0	3.9
A(2-8-12)	124.5	128.2	3.7	126.5	2.0
A(4-3-7)	112.7	112.4	0.3	111.2	1.5
A(4-3-8)	62.1	61.0	1.1	61.1	1.0
A(3-4-5)	111.4	112.3	0.9	111.8	0.4
A(3-4-9)	61.3	61.0	0.3	61.4	0.1
A(3-4-23)	48.6	49.8	1.2	49.5	0.9
A(3-4-24)	152.3	150.9	1.4	152.1	0.2
A(7-3-9)	102.9	97.8	5.1	96.5	6.4
A(7-3-21)	91.8	96.0	4.2	97.0	5.2

Table A.9. (Continued)

A(7-3-23)	140.3	138.9	1.4	139.5	0.8
A(3-7-8)	61.7	65.3	3.6	65.2	3.5
A(3-7-13)	63.2	66.0	2.8	66.5	3.3
A(9-3-21)	124.1	124.1	0.0	125.5	1.4
A(9-3-23)	96.1	100.5	4.4	99.6	3.5
A(3-9-4)	58.9	58.0	0.9	57.5	1.4
A(3-9-8)	64.4	68.3	3.9	68.3	3.9
A(3-9-10)	117.6	119.9	2.3	119.8	2.2
A(3-9-13)	66.5	69.1	2.6	69.6	3.1
A(3-9-14)	119.5	126.6	7.1	125.9	6.4
A(21-3-23)	106.0	103.5	2.5	103.2	2.8
A(3-21-22)	176.0	176.3	0.3	173.6	2.4
A(3-23-4)	81.4	80.2	1.2	81.1	0.3
A(5-4-9)	100.6	97.5	3.1	96.8	3.8
A(5-4-23)	140.2	139.0	1.2	139.8	0.4
A(5-4-24)	95.7	95.6	0.1	94.4	1.3
A(4-5-8)	62.2	65.2	3.0	64.8	2.6
A(4-5-10)	64.9	66.2	1.3	66.4	1.5
A(9-4-23)	96.2	100.4	4.2	99.9	3.7
A(9-4-24)	120.8	125.2	4.4	126.9	6.1
A(4-9-8)	65.1	68.3	3.2	68.0	2.9
A(4-9-10)	67.8	69.5	1.7	69.8	2.0
A(4-9-13)	117.2	119.8	2.6	119.5	2.3
A(4-9-14)	120.3	127.1	6.8	126.0	5.7
A(23-4-24)	106.1	103.4	2.7	104.0	2.1
A(4-24-25)	174.3	176.4	2.1	174.3	0.0
A(8-5-10)	63.7	64.4	0.7	63.9	0.2
A(5-8-6)	72.9	78.6	5.7	75.8	2.9
A(5-8-7)	126.5	128.9	2.4	127.3	0.8
A(5-8-9)	108.5	105.9	2.6	107.6	0.9
A(5-8-11)	66.9	70.4	3.5	69.7	2.8
A(5-8-12)	128.9	135.0	6.1	132.5	3.6
A(5-10-9)	101.4	100.0	1.4	99.6	1.8
A(5-10-11)	64.4	68.5	4.1	66.8	2.4

Table A.9. (Continued)

A(5-10-16)	164.4	163.9	0.5	163.7	0.7
A(5-10-17)	122.5	127.3	4.8	125.1	2.6
A(5-10-26)	99.8	95.6	4.2	99.7	0.1
A(6-8-7)	73.5	77.9	4.4	75.2	1.7
A(6-8-9)	173.0	168.6	4.4	171.8	1.2
A(6-8-11)	64.9	65.3	0.4	66.1	1.2
A(6-8-12)	66.0	65.2	0.8	65.9	0.1
A(8-7-13)	61.5	64.6	3.1	64.3	2.8
A(7-8-9)	109.9	106.0	3.9	107.3	2.6
A(7-8-11)	129.2	134.4	5.2	131.8	2.6
A(7-8-12)	68.3	69.8	1.5	69.0	0.7
A(7-13-9)	101.9	99.7	2.2	99.4	2.5
A(7-13-12)	65.4	68.1	2.7	66.9	1.5
A(7-13-15)	162.5	163.1	0.6	162.7	0.2
A(7-13-19)	125.1	127.7	2.6	126.6	1.5
A(7-13-28)	102.4	96.3	6.1	98.1	4.3
A(9-8-11)	109.1	105.9	3.2	107.7	1.4
A(9-8-12)	109.1	105.7	3.4	107.3	1.8
A(8-9-10)	65.4	66.7	1.3	66.6	1.2
A(8-9-13)	65.1	66.9	1.8	66.8	1.7
A(8-9-14)	64.3	68.3	4.0	67.2	2.9
A(11-8-12)	69.0	70.7	1.7	69.6	0.6
A(8-11-10)	62.3	63.2	0.9	62.4	0.1
A(8-11-14)	60.1	63.6	3.5	62.6	2.5
A(12-8-13)	60.1	63.3	3.2	62.2	2.1
A(12-8-14)	61.4	63.2	1.8	61.9	0.5
A(8-12-14)	59.9	66.4	6.5	65.8	5.9
A(9-10-11)	103.9	102.7	1.2	102.5	1.4
A(9-10-16)	64.0	63.9	0.1	64.4	0.4
A(9-10-17)	109.3	108.8	0.5	108.8	0.5
A(9-10-26)	127.5	134.1	6.6	130.7	3.2
A(9-13-12)	104.0	103.0	1.0	103.2	0.8
A(9-13-15)	61.3	63.4	2.1	63.6	2.3
A(9-13-19)	107.2	108.3	1.1	107.9	0.7

Table A.9. (Continued)

A(9-13-28)	126.2	134.9	8.7	135.4	9.2
A(9-14-11)	105.0	100.5	4.5	101.4	3.6
A(9-14-12)	105.2	100.7	4.5	101.6	3.6
A(9-14-15)	63.3	63.4	0.1	63.8	0.5
A(9-14-16)	65.1	63.4	1.7	64.5	0.6
A(9-14-17)	113.9	110.8	3.1	112.6	1.3
A(9-14-18)	171.1	171.6	0.5	171.3	0.2
A(9-14-19)	112.4	111.0	1.4	111.9	0.5
A(9-14-20)	119.8	118.6	1.2	120.7	0.9
A(11-10-16)	112.2	113.7	1.5	111.9	0.3
A(11-10-17)	61.6	62.9	1.3	61.8	0.2
A(11-10-26)	128.5	123.2	5.3	126.8	1.7
A(10-11-14)	60.7	63.0	2.3	62.5	1.8
A(16-10-17)	62.2	62.7	0.5	61.9	0.3
A(16-10-26)	93.8	96.0	2.2	93.7	0.1
A(10-16-14)	60.4	61.0	0.6	61.5	1.1
A(17-10-26)	98.2	94.7	3.5	95.9	2.3
A(10-17-14)	61.9	63.3	1.4	62.7	0.8
A(10-26-27)	176.4	176.9	0.5	177.7	1.3
A(11-14-12)	66.8	68.0	1.2	67.5	0.7
A(11-14-15)	168.3	163.8	4.5	165.0	3.3
A(11-14-16)	112.3	110.1	2.2	111.2	1.1
A(11-14-17)	62.3	62.6	0.3	63.0	0.7
A(11-14-18)	68.0	72.5	4.5	71.7	3.7
A(11-14-19)	123.9	125.2	1.3	125.0	1.1
A(11-14-20)	122.6	128.1	5.5	126.2	3.6
A(13-12-14)	60.9	62.8	1.9	62.3	1.4
A(12-13-15)	111.9	113.6	1.7	112.3	0.4
A(12-13-19)	62.9	63.2	0.3	62.8	0.1
A(12-13-28)	129.7	122.1	7.6	121.4	8.3
A(12-14-15)	114.3	110.7	3.6	111.4	2.9
A(12-14-16)	170.0	163.8	6.2	165.9	4.1
A(12-14-17)	121.6	124.8	3.2	123.7	2.1
A(12-14-18)	67.4	72.5	5.1	71.1	3.7

Table A.9. (Continued)

<i>A(12-14-19)</i>	64.0	63.0	1.0	63.8	0.2
<i>A(12-14-20)</i>	125.3	128.8	3.5	126.5	1.2
<i>A(15-13-19)</i>	61.2	62.3	1.1	61.1	0.1
<i>A(15-13-28)</i>	92.4	96.4	4.0	96.6	4.2
<i>A(13-15-14)</i>	60.2	60.8	0.6	61.3	1.1
<i>A(19-13-28)</i>	96.5	93.9	2.6	93.4	3.1
<i>A(13-19-14)</i>	62.8	63.5	0.7	63.1	0.3
<i>A(13-28-29)</i>	177.5	177.0	0.5	177.8	0.3
<i>A(15-14-16)</i>	64.4	66.3	1.9	66.0	1.6
<i>A(15-14-17)</i>	121.4	123.7	2.3	123.4	2.0
<i>A(15-14-18)</i>	123.5	123.2	0.3	122.7	0.8
<i>A(15-14-19)</i>	63.8	63.2	0.6	63.0	0.8
<i>A(15-14-20)</i>	67.1	66.1	1.0	67.3	0.2
<i>A(16-14-17)</i>	63.5	63.0	0.5	63.6	0.1
<i>A(16-14-18)</i>	122.0	123.0	1.0	122.5	0.5
<i>A(16-14-19)</i>	120.7	123.8	3.1	122.3	1.6
<i>A(16-14-20)</i>	64.0	65.8	1.8	66.3	2.3
<i>A(17-14-18)</i>	68.4	70.6	2.2	69.5	1.1
<i>A(17-14-19)</i>	128.4	134.3	5.9	131.2	2.8
<i>A(17-14-20)</i>	67.5	71.9	4.4	70.2	2.7
<i>A(18-14-19)</i>	69.4	70.8	1.4	69.7	0.3
<i>A(18-14-20)</i>	69.1	69.9	0.8	68.0	1.1
<i>A(19-14-20)</i>	70.8	72.6	1.8	70.6	0.2
<i>Average</i>	94.9	95.8	2.5	95.5	1.8
<i>Minimum</i>	48.6	49.8	0.0	49.5	0.0
<i>Maximum</i>	177.5	177.0	8.7	177.8	9.2